Simulation Study on Relaxation Phenomena in Spherical Tokamak

Naoki MIZUGUCHI

DOCTOR OF PHILOSOPHY

Department of Fusion Science
School of Mathematical and Physical Science
The Graduate University for Advanced Studies

1999 (School Year)

March 31, 2000

Abstract

It is well known that relaxation phenomena which take place in thermonuclear plasma have great influence on the confinement in not only that it is usually harmful to sustainment of configuration, but sometimes that the confinement is improved to much better state by relaxation. The Taylor's theory[*J.B. Taylor, Rev. Mod. Phys.* **58**, 741 (1986)] is one of the most successful and useful theory describing relaxation phenomena, in which the total magnetic energy is minimized under the constraint that the total magnetic helicity is conserved. However, it is not sufficient to be applied for real fusion plasma because it ignores the existence of plasma pressure. On the other hand, the achievable plasma beta value in experiments has been increasing in recent years. In particular, the spherical tokamak concept is attracting a great deal of attention because it has excellent properties in the confinement and the stability at high β, and the engineering economy. Therefore, a generalized theory on relaxation phenomena including the effect of plasma pressure is needed. In this thesis, we shall try to reveal the dynamics of pressure-driven relaxation phenomena observed in spherical tokamak plasma, which is so-called IRE(Internal Reconnection Event), by means of a numerical simulation. IRE is observed as a rapid fall in the soft X-ray signal and an increase in the net toroidal current, together with a drastic deformation in overall shape. However, the physical mechanism of IRE had not been clarified at all until this study was carried out. The simulation results are full of suggestion for both improving the confinement of spherical tokamak plasma and understanding the general nature of the pressure-driven relaxation phenomena.

The simulation is based on a nonlinear three-dimensional magnetohydrodynamic equations. It is executed in a full toroidal spherical tokamak geometry including an open external magnetic field region, so that the dynamical behavior of an IRE, such as a large distortion in overall shape, can be properly treated. The spontaneous time development of tiny perturbations applied on an initial unstable equilibrium is pursued by a high-accuracy scheme.

The simulation results successfully reproduce the key features of IRE in good agreement with experimental observations. The dominant linear eigenmodes for an initial condition including a $q = 1$ rational surface are found to be a combination of several low-n modes. Especially, the $m = 2/n = 2$ and the $m = 1/n = 1$ pressure-driven interchange modes grow simultaneously with almost the same large growth rate. As a result of the nonlinear development of such low-n modes, which induce an elliptically elongating and shifting convection flow in the poloidal cross section, a pressure bulge appears on the surface of the torus in a toroidally localized region, where the radial positive displacements of each mode are aligned to each other. The localized deformation generates a current sheet structure near the separatrix, which induces magnetic reconnection between the internal and external magnetic fields. The reconnected field line links the core region at high pressure and the peripheral region at low pressure, so that a large pressure gradient is formed along the reconnected field line. The confined plasma is rapidly expelled out of the torus due to the flows induced by the pressure gradient. The expelled plasma extends in the periphery, forming a characteristic helically twisted conical layers at the top and

the bottom of the torus, which is in good agreement with experimental results observed by using a CCD camera. On the other hand, the plasma pressure at the center of the torus falls into about 40% of that at the initial state in a short time scale of several tens of Alfvèn transit time, which also agrees well with experiments. After releasing a part of heat energy out of the separatrix, the system is once stabilized with respect to ideal modes. However, another kind of an instability, which has a nature of a resistive mode, is excited. This instability includes an $m = 2/n = 1$ component dominantly, and can be destructive compared to the original ideal modes. Due to the growth of this instability, the overall shape of the torus is largely distorted, which agrees with experimental observations, such as the tilting and the axis-asymmetric elongation of the torus.

More detailed analyses of the simulation results show several interesting dynamics on pressure-driven relaxation phenomena, such as an almost parallel magnetic reconnection, formation of a tunnel-like convective loss channel due to the magnetic reconnection between the internal and the external fields, and spontaneous phase alignment among multiple modes on weakly nonlinear development of pressure-driven instability.

Contents

1 Introduction **4**
- 1.1 Relaxation phenomenon in plasma 4
- 1.2 Spherical tokamak 5
  - 1.2.1 Spherical tokamak configuration 5
  - 1.2.2 Historical review of spherical tokamak experiments 6
  - 1.2.3 Properties of spherical tokamak plasma 8
- 1.3 Relaxatioin phenomena in spherical tokamak 9
  - 1.3.1 The Internal Reconnection Event 9
  - 1.3.2 Disruptions and fast ion driven modes 13
- 1.4 Purpose of this study 13

2 Simulation model **15**
- 2.1 Simulation geometry 15
- 2.2 Basic equations 15
  - 2.2.1 MHD equations 15
  - 2.2.2 Normalization 17
- 2.3 Numerical scheme 17
  - 2.3.1 Fourth order finite difference and Runge-Kutta method 18
  - 2.3.2 Numerical stability 19
- 2.4 Initial condition 21
  - 2.4.1 Numerical solution of ST equilibrium 21
  - 2.4.2 Initialization for the nonlinear simulation 22
- 2.5 Boundary condition 23

3 Simulation result **25**
- 3.1 Overview of simulation results 25
- 3.2 Linear instability 27
  - 3.2.1 Linear growth of instability 27
  - 3.2.2 Mode structure 28
  - 3.2.3 Identification of modes 30
- 3.3 Nonlinear dynamics on relaxation phenomena 33
  - 3.3.1 Weakly nonlinear development of low-n interchange mode 33
  - 3.3.2 Collapse and localized deformation 36
  - 3.3.3 Magnetic reconnection between internal and external fields 38
  - 3.3.4 Convective loss of heat energy 43

3.4 Multi-step relaxation 48
3.4.1 Cessation and re-heating 48
3.4.2 Behavior of resistive instability 54

4 Discussion **58**
4.1 Comparison with experiments 58
4.1.1 Time development of observable quantities 58
4.1.2 Deformation of the overall shape 60
4.2 Dependency on parameters 64
4.3 Spontaneous phase alignment among modes 66
4.4 On the parallel heat transport 70

5 Concluding remarks **73**
5.1 Summary 73
5.2 Future work 74

A Numerical convergence test on the simulation **86**

Chapter 1

Introduction

1.1 Relaxation phenomenon in plasma

This thesis deals with relaxation phenomena in plasma. A relaxation in plasma is defined as an energy transition from a certain state to another lower or more stable energy state. Relaxation phenomena are often observed in various kinds of thermonuclear or space plasma. We should carefully treat the relaxation phenomena when we consider a magnetically confinement fusion plasma, partly because the plasma should be confined at as stable state as possible, and partly because the spontaneous transition among different states should be controlled as preferable. Therefore, it has been needed that relaxation phenomena in plasma are well understood systematically about the conditions and the physical mechanisms of the occurrences, the aspects of the time development, and the properties of the resultant relaxed state.

Over the past few decades numerous studies dealing with relaxation phenomena in plasma have been made. In the article published in 1974[1, 2], Taylor proposed a relaxed state, which is now so-called the Taylor's force-free configuration. In his theory, a minimum energy state that is expressed as

$$\nabla \times \boldsymbol{B} = \lambda \boldsymbol{B} \tag{1.1}$$

is derived under an assumption of a conservation in the total magnetic helicity. The equilibria of RFP or spheromak can be successfully explained by this relaxed state.

On the other hand, his theory has an insufficient point in that it ignores the effect of plasma pressure, though there must be a pressure gradient in real plasma. In recent years, several attempts have been made to construct a theory dealing with the relaxation in plasma with finite pressure. Zhu *et al.*[3] studied a self-organization process in plasma with finite pressure by means of a three-dimensional magnetohydrodynamic(MHD) simulation. They showed that a non-Taylor relaxed state, which is expressed as an MHD equilibrium,

$$\nabla p = \boldsymbol{j} \times \boldsymbol{B}, \tag{1.2}$$

is formed as the result of self-organization in finite pressure plasma. Experimentally, a formation of a field-reversed configuration(FRC) by means of a counter-helicity merging

of two spheromaks is studied in TS-3 device[4]. Since there is only the poloidal magnetic field and the toroidal current in the finally formed FRC with finite pressure, this relaxation process cannot be explained by the Taylor's theory. A two-dimensional MHD simulation is executed to explain this relaxation process[5]. In Ref.[5], it is shown that the thermal energy which is generated by the release of the magnetic energy due to the driven magnetic reconnection between two spheromaks is transported by the poloidal plasma flow induced by the reconnection, so that an FRC with finite pressure gradient is formed.

However, the general treatment for finite pressure relaxation has not been well understood yet. In recent years there has been renewal of interest in high-β plasma in thermonuclear fusion research to realize efficient fusion compared to the conventional vast experimental devices. In such high-β plasma, plasma pressure plays an important role on relaxation events such as sawteeth and disruptions. Therefore, it has become an urgent research topic to understand the relaxation in finite pressure plasma.

1.2 Spherical tokamak

1.2.1 Spherical tokamak configuration

As a concrete example of high β plasma, in which the effect of the pressure plays an important role on its dynamics, we focus on the spherical tokamak (ST) plasma [6, 7, 8]. The ST concept has been recently attracting a great deal of attention in the nuclear fusion community, because it has promising properties in the stability, the confinement, the compactness, and so on. The ST is called by several different names at present situation, such as "low aspect ratio tokamak (LART)" and "spherical torus", or sometimes it is nicknamed "fat tokamak". Though the definition of ST configuration has not been settled yet, there is a common perception that the tokamak which has a smaller aspect ratio ($A \equiv \frac{\text{major radius}(R)}{\text{minor radius}(a)}$) than approximately 2 should be considered as an ST separately from conventional tokamaks. Here, it should be noted that the ST is usually in vertically elongated shape and its magnetic axis is largely shifted out, therefore, the minor radius cannot be uniquely defined. Usually, it is measured as a half width of the outermost surface on the midplane of the torus . Especially, the ST of much smaller aspect ratio ($A < 1.5$), which has several unique properties in the equilibrium, is sometimes called the "ultra low aspect ratio tokamak (ULART)".

Figure 1.1 shows the image of the overall shape of a ST plasma which is taken by a charge coupled device (CCD) camera in Small Tight Aspect Ratio Tokamak(START) at Culham[9]. The brighter region on the image corresponds to colder plasma near the outermost surface. As one can see from Fig.1.1, the overall shape of ST looks like an almost spherical one due to the smallness of the aspect ratio, which is where it gets its name spherical tokamak from. The dark part at the center of the picture is a so-called "centerpost" made of a conductor rod, which forms a part of the boundary of a toroidal confinement system. Thus, the ST device is composed by a cylindrical chamber with a center conducting rod. In other words, one can regard the ST as a compromise between tokamak and compact tori. It is a quite simple machine configuration compared to large aspect devices such as a conventional tokamak, in which bulky poloidal coils link the torus

shaped chamber.

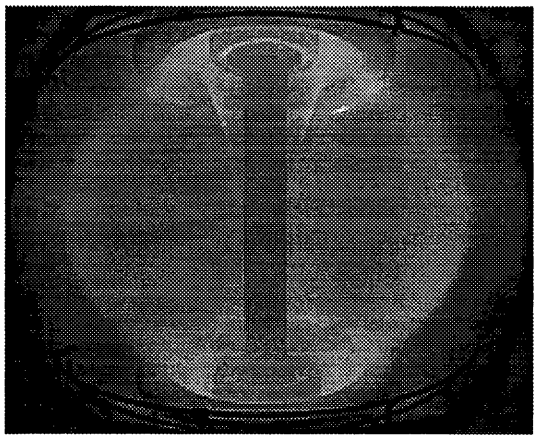

Figure 1.1: Picture of overall shape of START plasma by courtesy of Dr. A. Sykes and Dr. M. Gryaznevich.

In general, the ST equilibrium has a large toroidicity due to the smallness of the aspect ratio, so that it tends to have a strong stability and good confinement. Shown in Fig.1.2 is a typical trace of the magnetic field line on the $q = 7$ rational surface. It should be noted that the field line traces more turns in the inner (good curvature) part than in the outer (bad curvature) part because of its strong toroidicity. Therefore the curvature tends to be good in average along the magnetic field line compared to the conventional tokamak configuration where the field line traces almost uniformly in both the inner and the outer region.

In following subsections, the review of ST research and the basic properties of ST plasma are described.

1.2.2 Historical review of spherical tokamak experiments

The ST research of today is based on the conceptional design by Peng *et. al* [6, 10, 11]. They obtained an equilibrium of a low aspect ratio tokamak with a large natural elongation and a strong paramagnetism. They pointed out that the equilibrium has a promising properties in that the large plasma current and a high beta value are available with small toroidal magnetic field compared to conventional tokamaks with an assumption that the confinement of ST plasma obeys the Troyon's scaling law[12].

Such features of ST plasma are confirmed experimentally first in Hidelberg by Bruhns *et al*[13]. They showed that a spheromak with an axial conductor forms a spherical tokamak configuration, which is globally stable without any additional stabilization. In particular, the tilt instability is found to be suppressed in such configuration.

An intensive ST experiment has begun since 1991 at Culham. The experiment is named Small Tight Aspect Ratio Tokamak(START)[14]. The START experiment had taken the lead in the ST research of the world until its shutdown in 1998. The behavior of ST plasma is investigated in detail, and showed an excellent stability and

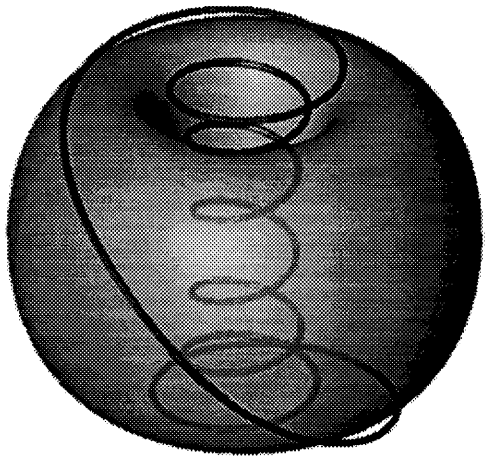

Figure 1.2: Typical magnetic field line trace in ST configuration on the $q = 7$ rational surface. It can be seen that the field line trace turns once in the outer region and six times in the inner region in toroidal direction while it go round in the poloidal direction.

confinement[7, 14]. It was also observed that the ST is free from a current-terminating disruption, and that the edge configuration forms a natural exhaust system. These features were recognized to be preferable for confinement. In the first stage of the START experiment, the property of plasma had been increased up to the electron temperature of ~500 eV and the plasma current of ~150 kA with a natural and a double-null divertors[15]. Furthermore, the MHD activity in START plasma is studied in Ref.[15] in detail. A relaxation phenomenon termed Internal Reconnection Event(IRE) had been recognized in this period. The detail of the IRE will be described in the next section. It was also found in Ref.[15] that the density limit for the ST operation lies near that of the conventional tokamak, and is limited by the existence of IRE, not a hard disruption like conventional tokamak.

In 1996, a neutral beam injector(NBI) was settled on START experiment for an additional heating[16, 17]. It had led to significant improvements in plasma performance. The beta value had been increased up to ~50% at the center and ~10% in volume average. The scaling law for the energy confinement of ST plasma had been explored in wide range, and found that it is as good as or better than the H-mode scalings from conventional tokamak. The normalized beta value[12] was estimated by $\beta_N \sim 3.5$ at this period. The disruption immunity and the existence of IRE was confirmed to occur at such high beta regime. By developing the performance of plasma, the volume-averaged beta value had reached 30% in 1998[18, 19]. The properties at such high-beta regime was intensively studied, and found that the normalized beta exceeds 4. Besides, the MHD behavior at an IRE is studied by using charge coupled device(CCD) cameras[19].

Further enhancement in the plasma performance had been done until the shutdown of START experiments at 1999[20, 21, 22]. The volume-averaged beta value had exceed 40%

at the final stage of START experiments. The confinement property of such high-beta regime showed that the normalized beta $\beta_N \sim 5$. On the other hand, a current-terminating disruption came to be observed after a divertor coil was installed near the plasma [21, 9]. In such enhanced plasma heated by NBI, several energetic particle-driven instabilities such as chirping, fishbone, and other Alfvènic modes were also observed[21, 23]. These results in START experiment are reviewed in Refs.[24, 25].

Other smaller experiments were carried out in CDX-U[26, 27, 28] at Princeton, HIT[29, 30, 31], HIT-II[32, 33] at Washington, TST, TST-M[34, 35, 36, 37] at Tokyo, TS-3[4, 38, 39] at Tokyo, HIST[40] at Himeji, NUCTE-ST[41] at Nihon Univ., and Rotamak-ST[42] at Australia focusing on each interest. In CDX-U, an ST of $I_p \sim$100kA is formed by using a non-inductive current drive concept. The MHD activities are observed in detail. It should be noted that the IRE is also observed in CDX-U. Another scheme for the current drive using a so-called coaxial helicity injection is studied in HIT and HIT-II. They observed that an ST plasma of $I_p \sim$250kA is formed in HIT experiment. The TS-3 ST plasma, on the other hand, makes use of a merging technique to form a ST configuration. In TST and TST-M, detailed measurements on plasma fluctuations were done.

In 1999, couple of large ST experiments have completed their construction. NSTX at Princeton[43, 44] has achieved the plasma current of $I_p \geq$1MA in 1999. Another large device MAST at Culham [24, 45] has begun its operation, aiming at an 1 mega-ampere plasma current. These large ST plasmas are formed at larger vertical elongation and safety factor than the previous devices. Other middle-sized ST plasmas are under planning at Pegasus in Wisconsin[46], and Globus-M in Russia[47].

1.2.3 Properties of spherical tokamak plasma

According to the first conceptual design for ST experiment by Peng *et. al*[6], the ST equilibria are characterized by

- high toroidal beta($\beta_t > 0.2$),
- low poloidal beta($\beta_p < 0.3$),
- large natural elongation($\kappa \simeq 2$),
- large plasma current,
- strong paramagnetism,
- strong magnetic helical pitch.

These features such as a large elongation and magnetic shear lead the increase in the MHD stability, and imply that a compact, high beta plasma is available with low magnetic field. They showed that an ST equilibrium with beta value above 20% can be obtained under an assumption that the Troyon's scaling law is applicable at low aspect ratio.

More quantitative analysis of the stability of ST plasma for ideal modes is carried out by Carreras *et al.*[48] by using an linear stability code such as ERATO[49] and PEST2[50]. They found that the Troyon's scaling law is a good extrapolation at low aspect ratio($A \leq$

2.5). Namely, the critical beta value is found to be higher than the Troyon's scaling parameter,

$$\beta_{crit} = \beta_N \frac{I_p[\mathrm{MA}]}{a[\mathrm{m}]B_0[\mathrm{T}]}, \tag{1.3}$$

where the normalized beta value $\beta_N \simeq 3.5$. They obtained such scaling extrapolation without full optimization of equilibria. They also showed by means of a nonlinear simulation that the stability for resistive tearing modes is also increased in ST equilibria.

More accurate calculation for the MHD stability in ST plasma is carried out by Menard *et al.*[51].They explored the ideal MHD stability limits by numerically optimizing the equilibria for several distinct regimes of operation. And they found a stable equilibrium at $\beta = 45\%$ with $A = 1.4$ and $\kappa = 3.0$.

Yamada *et al.* [52] studied the effect of the external toroidal field current (I_{tf}), which is to be applied on the center post, on the stabilization of the global tilt/shift modes. They showed that only a small I_{tf} of about 10% of the plasma current is needed to stabilize such modes. This result was in good agreement with the observation in TS-3 experiment.

Such properties of ST plasma on the equilibrium and the stability are proved in numbers of experimental results as described in the previous subsection.

1.3 Relaxatioin phenomena in spherical tokamak

As described in Sec.1.2.2, there was no experimental evidence of current-terminating disruptions in the early ST experiments. Such disruption immunity proved an advantage of ST plasma. In absence of such dangerous disruption, a more moderate, recuperative MHD activity was observed. This phenomenon is called the Internal Reconnection Event (IRE). IRE is peculiar relaxation phenomenon to ST plasma. In the recent experiments, other relaxation phenomena that are commonly observed in other configurations such as conventional tokamaks are also observed. In this section, these relaxation phenomena in ST plasma are reviewed.

1.3.1 The Internal Reconnection Event

In the early experiments in START device[15, 16], a relaxation phenomenon termed IRE(Internal Reconnection Event) was often observed. The IRE can be observed as a series of positive spikes in the plasma current trace. Similar spikes in H_α and CIII signals, and rapid drops in the soft X-ray(SXR) and the line integrated electron density signals were often accompanied to the current spikes[9]. The IRE is also observed in CDX-U[28]. However, the physical mechanisms for the occurrences of IREs have not been clarified enough yet.

The advanced diagnostics in ST experiments has provided a lot of clues for understanding the characteristic features of IREs. The plasma current trace for a typical shot in the early START experiment is shown in Fig.1.3 together with the corresponding line-integrated density trace[9]. It can be clearly seen in Fig.1.3(a) that there are six spikes

after $t = 29$ msec. Each of them is referred to an IRE. The duration time of each spike is around 200μsec. It should be noted that the IRE occurs repeatedly like this shot in most case. At the moment the current increases, on the other hand, the line-integrated density falls rapidly as shown in Fig.1.3(b). The time scale of the density fall seems to be shorter than that of the current spike. The fallen density ramps up to the former level during the intermissions of IREs. The behavior of the density trace is so similar to sawteeth that it can be difficult in some cases to distinguish an IRE from a sawtooth. IREs are differentiated from sawteeth in that the current increase in sawteeth is much small compared to that in IREs, and that the sawteeth repeat in almost regular intervals while IREs appear irregularly.

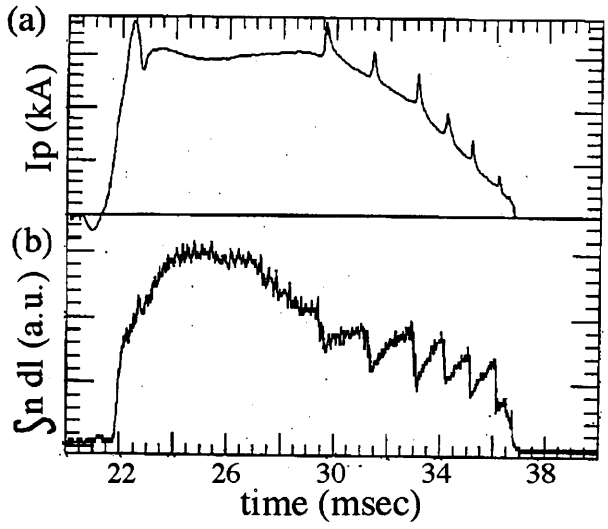

Figure 1.3: Experimental results in START by courtesy of Dr. A. Sykes and Dr. M. Gryaznevich. The time development of (a) the plasma current and (b) the line-integrated density is drawn for a typical discharge(#25868).

As for each individual IRE, the temporal change in the observed quantities is shown in Fig.1.4 for a typical shot in START experiment with an IRE (#36546, START)[9] for example. IRE usually proceeds in three stages as indicated in Fig.1.4 with I, II, and III, respectively. The first stage is the precursory thermal quench phase. In this stage, the growth of low-n activities and accompanying rapid fall in the SXR and the $\int ndl$ signals are observed. There is only a little change in the other signals in this stage. The second stage is accompanied by profile redistribution. The plasma current increases in a short time scale of around 50μsec. The last stage is referred to the post-IRE mode evolution and current quench. The increased current in the former stage gradually decreases to some level, and the CIII signal, which roughly corresponds to the increase of the inpurity in the edge region, decreases. As described in the next subsection, this stage sometimes end in hard disruption in more recent experiments in START.

The temporal change in the radial electron temperature and density profiles can be measured by using Thomson scattering diagnostics. The experimental results of the time

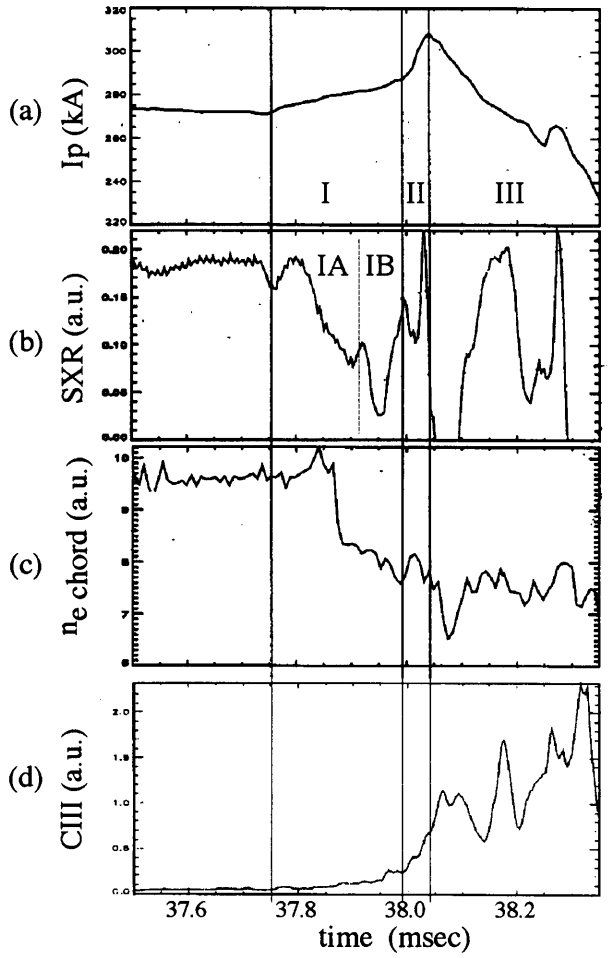

Figure 1.4: Experimental results in START by courtesy of Dr. A. Sykes and Dr. M. Gryaznevich. The time development of (a) the plasma current, (b) the soft X-ray signal at R=34.6cm (close to the magnetic axis), (c) the line-integrated density, and (d) the CIII emission are drawn for a typical IRE (#36546). The distinguishable three stages numbered I, II, and III are specified in (a). Stage I often proceeds in more two steps (IA, IB).

development in the temperature and density profiles, which are obtained in START[16, 9] shows that the central values of these quantities fall in a short time scale of around 100 μsec when an IRE occurs. The profiles become somewhat broaden after the collapse in the central value.

Another unique characteristic of IREs is a large distortion in the overall shape of the torus. In START, some charge coupled devise(CCD) cameras monitor the whole torus. Figure 1.1 is the typical snapshot at a steady state. While the IREs or the disruptions occur, a large helical low-n distortion is often observed in CCD images[18, 19, 9]. Shown in Fig.1.5 is the example of such distortion. A large helical twist at the core plasma region and a vertical extension of the visible light toward the top and the bottom boundary of the chamber can be seen. The properties of such distortion will be described in Sec.4.1.2 in detail comparing with our simulation results.

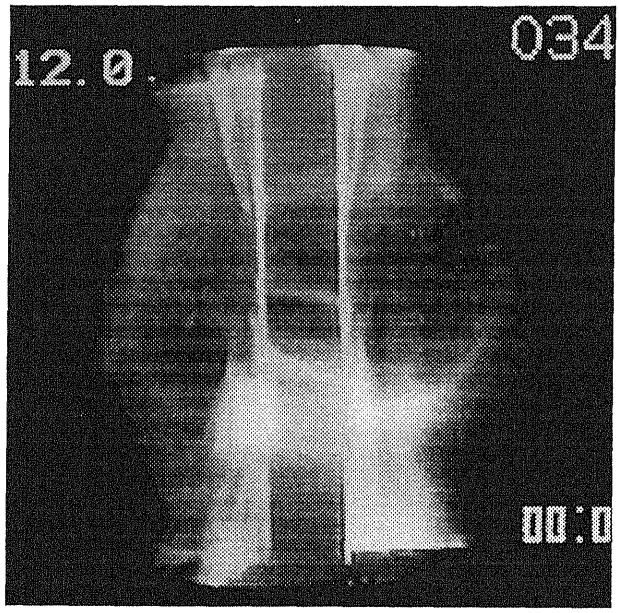

Figure 1.5: Large distortion accompanying with an IRE observed by CCD camera. (Courtesy of Dr. A. Sykes and Dr. M. Gryaznevich)

The occurrence of IRE needs to be carefully considered when we aim to improve the confinement of STs. As we can see from Fig.1.3(a), once IRE occurs the confinement seems to become unstable compared to the former steady state, so that the second IRE soon occurs, even if the plasma current looks as if it recovers to some level after the first IRE occurs. The plasma current also degrades itself to some extent, and the stored energy is lost typically in 30$\sim$40% every time IRE occurs [21, 9]. On the other hand, the strong resilience of IRE implies the existence of an excellent potential for self-organization in ST plasma. If we can make use of it, or at least if we can control it as it would not end in disruption, it will be a great help in improving the confinement of ST plasma.

There is only a few theoretical attempts about the IRE. A model for describing IREs has been developed by R. J. Buttery *et al.* In Ref.[21, 53], they reconstructed equilib-

rium using a free-boundary Grad-Shafranov code with the experimental data obtained in START. By comparing the pre- and the post-IRE states, they found out a conservation constraint in "modified helicity". Scanning in various aspect ratios and falls in β_p using this constraint, they successfully explained the distinctive features of IRE such as disruption immunity at low aspect ratio. However, there is no previous work that treats the dynamics during an IRE.

Thus, the characteristic features of IRE are summarized as follows.

- rapid fall in the density and the temperature at the core
- rapid increase in the plasma current and the edge activity
- a large axis-asymmetric deformation in overall shape
- large scale (low wavenumber) precursor
- strong resilience after the collapse

1.3.2 Disruptions and fast ion driven modes

In the early operation in START[16], and also other small STs such as CDX-U [28], no rapid current-terminating disruptions were observed except for tiny ones that occur as the last of sequential IREs. However, in more recent operations in START[19, 21] with higher-β and lower safety factor, the discharges end in terminating disruptions. The cause for the appearance of disruption is now thought to be related the machine configuration. After the installation of the divertor coils closer to the plasma in 1996, the frequency of the occurrence of disruptions is increased [21, 9]. The CCD images at the disruption phase shows that the plasma is elongated so that the edge of the plasma contacts the divertor coils. The prior stage to the disruption, on the other hand, is observed to be almost the same as IREs.

The NBI operation in START has made an opportunity for experimental study on the physics of energetic ion in ST plasma. Several energetic particle-driven instabilities such as the chirping modes, fishbones, and some other fixed-frequency modes in Alfvèn frequency range have been found[21], and are discussed[23, 54].

1.4 Purpose of this study

The main purpose of this study is to reveal the physical mechanism of the IRE by means of a numerical simulation. Namely, we aim to explain the scenario of an IRE with a spontaneous time development of plasma from the beginning to the end continuously and self-consistently. This should be placed upon the first attempt to understand the relaxation process in finite pressure plasma. The dynamics of the high-β plasma on the relaxation event which will be revealed by this study must have a lot of information for exploring the relaxation theory to the finite pressure regime. This study will intermediate between the phenomenology and the unsolved theory related to the finite pressure relaxation in plasma. For that purpose it is necessary to reproduce the nature of relaxation

phenomena as it is by the simulation. The numbers of experimental observation will help us to examine the accordance of the simulation results with real phenomena.

Bearing in mind the above objective, most of this study is devoted to reproduce the IRE by the simulation. Since the mechanism of IRE is not understood at all, we firstly aim to understand the outline of the phenomenon by using as simple model as possible. Thus, we carry out a magnetohydrodynamic (MHD) simulation in a three-dimensional full toroidal geometry to investigate the characteristic feature of IRE which is considered to be governed by large scale activities. The simulation results are immediately compared with the experimental results, and the discrepancy between them are fed back to the modelings. Repeating such investigations many times, we can improve the modelings and can reproduce the phenomenon appropriately.

After that, or in the process of the modelings, the detail of the dynamics will be revealed by analyzing the reproduced phenomenon carefully. The dynamics which appears in an IRE has a lot of interest in general physics such as magnetic reconnection process under a finite pressure. The results which are described in this thesis have been obtained by such a trial-and-error approach. Furthermore, we can obtain some suggestions for suppressing the occurrence of IRE in experiments from the result. It will improve the confinement of the plasma in ST experiments.

Thus, this study has several meanings in addition to an exploration into the generalization of relaxation theory to finite pressure regime. Firstly, it will help us to know how the occurrence of IRE is suppressed in experiments. It is directly related to the realization of nuclear fusion. Secondly, it is a challenge to such kind of approach with highly sophisticated numerical computations for investigating the large scale dynamics observed in real fusion experiment. And finally, each individual processes included in an IRE is full of physical interest.

In following chapters, the simulation model and results are described as a unified scenario for an IRE by summarizing the modelings. Some pieces of consideration are described in Chap.4. And finally, the summary of this study and some remarks are described in the last chapter.

Chapter 2

Simulation model

2.1 Simulation geometry

As described in Chap.1, an IRE is accompanied by a large distortion in overall shape. The distortion extends to the vacuum region, where the plasma does not exist before the IRE occurs. To consider such dynamics of IRE in simulation, it is necessary to treat self-consistently over the whole region where the torus itself and the peripheral region are included. The distortion usually appears as a non-axisymmetric one. Therefore, a full three-dimensional computation geometry is needed to reproduce the distortion properly. We adopt such a simulation system as shown in Fig. 2.1. A three-dimensional full-toroidal cylindrical coordinate (r, θ, z) is used. The region where the simulation is performed includes both the core ST plasma and the peripheral magnetic field. The peripheral region is not modelled as a vacuum but is filled with low pressure plasma. The plasma can freely extend into the peripheral region as a result of time development. A conductor rod is placed on the center of the cylinder. Since the plasma motion that is propagated by the Alfvèn wave is disturbed at the top and the bottom boundary, the simulation result is more sensitive to the conditions of these boundaries than the inner and the outer boundaries. Therefore, we leave a sufficient margin in the vertical direction from the core plasma in order to avoid the disturbance from the reflection at the top and the bottom boundaries.

2.2 Basic equations

2.2.1 MHD equations

The basic equations to be solved in the simulation are the standard set of compressive MHD equations as follows.

$$\frac{\partial \rho}{\partial t} = -\nabla \cdot (\rho \boldsymbol{v}) \tag{2.1}$$

$$\frac{\partial}{\partial t}(\rho \boldsymbol{v}) = -\nabla \cdot (\rho \boldsymbol{v}\boldsymbol{v}) - \nabla p + \boldsymbol{j} \times \boldsymbol{B} + \mu(\nabla^2 \boldsymbol{v} + \frac{1}{3}\nabla(\nabla \cdot \boldsymbol{v})) \tag{2.2}$$

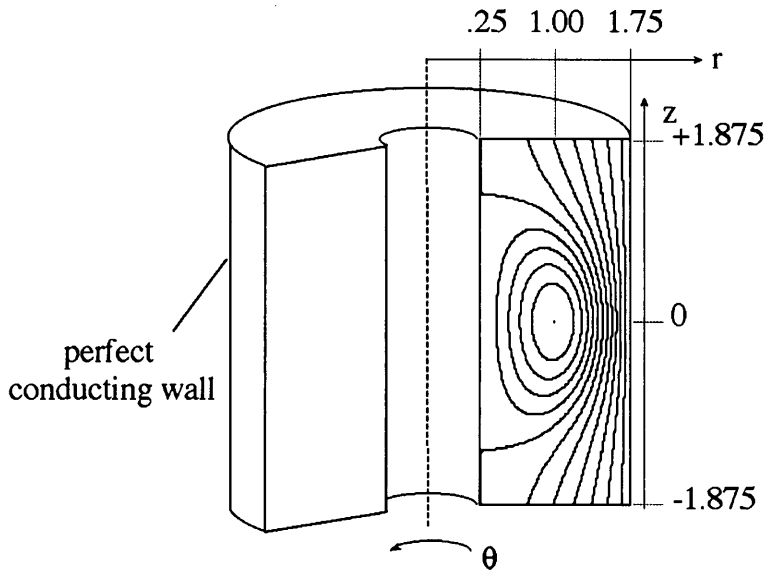

Figure 2.1: Schematics of simulation geometry.

$$\frac{\partial \boldsymbol{B}}{\partial t} = -\nabla \times \boldsymbol{E} \tag{2.3}$$

$$\frac{\partial p}{\partial t} = -\nabla \cdot (p\boldsymbol{v}) - (\gamma - 1)(p\nabla \cdot \boldsymbol{v} + \eta \boldsymbol{j}^2 + \Phi) \tag{2.4}$$

$$\boldsymbol{j} = \nabla \times \boldsymbol{B} \tag{2.5}$$

$$\boldsymbol{E} = -\boldsymbol{v} \times \boldsymbol{B} + \eta \boldsymbol{j} \tag{2.6}$$

$$\Phi = 2\mu(e_{ij}e_{ij} - \frac{1}{3}(\nabla \cdot \boldsymbol{v})^2) \tag{2.7}$$

$$e_{ij} = \frac{1}{2}(\frac{\partial v_i}{\partial x_j} + \frac{\partial v_j}{\partial x_i}) \tag{2.8}$$

The independent variables to be solved are the density ρ, the flow velocity $\boldsymbol{v}$, the intensity of magnetic field $\boldsymbol{B}$, and the plasma pressure p. The fluid is considered to be a single fluid. Equation (2.1)-(2.4) are the equation of continuity, the equation of motion, the equation of induction (Faraday's law), and the equation of pressure, respectively. In Eq. (2.2), $\boldsymbol{j}$ is the current density given by the Ampére's law which is expressed as Eq. (2.5). μ is the viscosity, which is assumed to be a uniform constant. In Eq. (2.3), $\boldsymbol{E}$ is the electric field calculated from the Ohm's law, which is expressed as Eq. (2.6). Since the resistivity η is included in Eq. (2.6), the effect of resistive diffusion is solved in this simulation. Here, η is assumed to be a uniform constant everywhere in the simulation region. Adding the time evolution of pressure solved in Eq. (2.4), the equations are closed. The first term of the right hand side of Eq. (2.4) represents the convection, and all of the heating terms are included in the second term. The heating term consists of adiabatic compression ($p\nabla \cdot \boldsymbol{v}$), the Ohmic heating($\eta \boldsymbol{j}^2$), and the viscous heating(Φ). The viscous heating is represented as Eq. (2.7) using with the rate of strain tensor defined as Eq. (2.8). It should be noted that the local conservation of energy is kept everywhere.

2.2.2 Normalization

In this simulation, the MHD equations are solved in a normalized form like (2.1)-(2.8). The proportional factor of current to rotation of magnetic field appearing in the Ampére's law is chosen to be unity, as represented in (2.5). The magnetic field is normalized by the value at the magnetic axis in the initial equilibrium(B_0). Since pressure has the same order as that of the energy density, that is, square of magnetic field, pressure is automatically normalized by scaling magnetic field, or,

$$p_0 = B_0^2. \tag{2.9}$$

The spacial scale is normalized by the major radius of the geometric center of the simulation region(see Fig. 2.1). The mass density is assumed to be uniformly $\rho_0 = 1$ everywhere in the simulation region. The normalization for velocity is given as the Alfvén velocity at the magnetic axis

$$v_0 = \frac{B_0}{\sqrt{\rho_0}} = B_0 \tag{2.10}$$

Therefore, the time scale is normalized by the Alfvén transit time at the magnetic axis for the length of the major radius of the geometric center.

Thus, we can compare the simulation results with real experiments, by scaling the spacial dimension, the density, and the magnetic field. For example, the plasma parameters of a typical NBI shot of START plasma in 1996 are as follows[17].

- toroidal magnetic field at the geometric center ~ 0.2 (T)
- major radius ~ 0.34 (m)
- line averaged density $\sim 4 \times 10^{19}(m^{-3})$
- volume averaged total beta $\beta_T \sim 10\%$

By using these parameters, we can estimate the normalization of the time scale for this shot as $1(\tau_A) \sim 0.5(\mu\text{sec})$.

2.3 Numerical scheme

Eqs. (2.1)-(2.8) are solved numerically. In this section, the outline of numerical scheme is described. This is based on the finite difference method and an explicit time integration. Such a scheme is simple compared to other method such as the spectral method. Especially, it is suitable for a large scale computing by using a super computer. The computation can be executed at an extremely high speed up to 13 GFLOPS on NEC/SX-4 super computer. It takes only about 30 hours to simulate through the whole process. It is important to try the simulation many times in various situations to explore unknown phenomena. The highly efficient computing enables such a trial-and-error approach.

2.3.1 Fourth order finite difference and Runge-Kutta method

We solve (2.1)-(2.8) by using the finite difference method. All the quantities in (2.1)-(2.8) are defined at finite discrete points forming a so-called numerical grid. In this simulation, the numerical grid is composed in regular intervals in each r, θ, and z direction. The number of the grid points should be large enough to obtain appropriate accuracy. The question whether the numerical solution of the equation approaches the real solution when the grid number is increased is called a convergence problem. When one executes a simulation, the convergence check is important to make sure the reliability of the solution. Here, we use $(N_r, N_\theta, N_z) = (128, 64, 128)$ as the number of numerical grid. It is large enough to treat at least large scale dynamics, and the solution is converged. The detailed convergence analysis is described in Appendix. The step size δr , $R\delta\theta$, and δz is scaled to be 4mm, 33mm, and 10mm, respectively, for the START operation parameter. It is quite reasonable resolution.

To obtain as higher accuracy as possible with reasonable memory size, it is effective to raise the order of the finite difference approximation. We use a forth order finite difference approximation in this simulation. A first spatial derivative of a variable f at a discrete point is represented in the fourth-order central difference form by

$$\left.\frac{\partial f}{\partial x}\right|_{x=x_i} = \frac{1}{12\delta x}(-f_{i+2} + 8f_{i+1} - 8f_{i-1} + f_{i-2}), \tag{2.11}$$

where i is the index of the numerical grid for the spatial coordinate x, and δx is its interval. The numerical error due to the finite difference approximation is of the order of $(\delta x)^4$ at most. As we can see from (2.11), the estimation at the grid point i needs the information at two neighbors in both directions($i - 2 \sim i + 2$). Therefore, another treatment is necessary near the boundaries. There are two approaches for it. First one is to represent the derivatives by using the one-side difference form. The fourth order forward difference, for example, is represented by

$$\left.\frac{\partial f}{\partial x}\right|_{x=x_i} = \frac{1}{12\delta x}(-3f_{i+4} + 16f_{i+3} - 36f_{i+2} + 48f_{i+1} - 25f_i), \tag{2.12}$$

However, it has been found that the resultant numerical error tends to become large with this method. Therefore, we adopt another approach, which makes use of a lower order approximation near the boundaries. Namely, at the grid points next to the boundary, a second order central difference,

$$\left.\frac{\partial f}{\partial x}\right|_{x=x_i} = \frac{1}{2\delta x}(f_{i+1} - f_{i-1}), \tag{2.13}$$

is used, and, at the boundary, a first order difference,

$$\left.\frac{\partial f}{\partial x}\right|_{x=x_i} = \frac{1}{\delta x}(f_{i+1} - f_i), \tag{2.14}$$

is used. Such treatment of reducing the order of the difference approximation near the boundary has a stabilizing effect for the solution, in particular, when there is a reflection of short-wavelength wave at the boundary wall.

Thus, all the derivatives in the right hand side of (2.1)-(2.4) are represented in the finite difference form by using (2.11), (2.13)-(2.14). The partial differential equations (2.1)-(2.4) are now treated as ordinary differential equations in respect to t by estimating the right hand side at each time.

The time integration is calculated explicitly by using fourth-order Runge-Kutta method. Now we denotes the set of the independent variables $(\rho, \boldsymbol{v}, \boldsymbol{B}, p)$ by the vector $\boldsymbol{y}$, and the sum of the right hand side of (2.1)-(2.4) by the vector $\boldsymbol{g}$. A fourth-order Runge-Kutta method for (2.1)-(2.4) is represented by

$$\boldsymbol{y}^{n+1} = \boldsymbol{y}^n + \frac{1}{6}(\boldsymbol{k_1} + 2\boldsymbol{k_2} + 2\boldsymbol{k_3} + \boldsymbol{k_4}) \tag{2.15}$$

$$\boldsymbol{k_1} = \delta t \boldsymbol{g}(\boldsymbol{y}^n) \tag{2.16}$$

$$\boldsymbol{k_2} = \delta t \boldsymbol{g}\left(\boldsymbol{y}^n + \frac{\boldsymbol{k_1}}{2}\right) \tag{2.17}$$

$$\boldsymbol{k_3} = \delta t \boldsymbol{g}\left(\boldsymbol{y}^n + \frac{\boldsymbol{k_2}}{2}\right) \tag{2.18}$$

$$\boldsymbol{k_4} = \delta t \boldsymbol{g}(\boldsymbol{y}^n + \boldsymbol{k_3}), \tag{2.19}$$

where n and δt is the time index and the time interval, respectively. The numerical error for this scheme is of the order of $(\delta t)^5$ at most. Combining (2.1)-(2.8) and (2.15)-(2.19), we can solve the MHD equations numerically.

2.3.2 Numerical stability

The time interval δt should be carefully selected as it does not break the numerical stability condition. The numerical stability for this scheme is estimated by following discussion[55]. Now, we consider the propagation of a Fourier component of a plane wave

$$f(x,t) = f_0 \exp(i\omega x - ikt). \tag{2.20}$$

(2.20) is the exact solution of the wave equation

$$\frac{\partial f}{\partial t} = -\frac{k}{\omega}\frac{\partial f}{\partial x} \tag{2.21}$$

with a periodic boundary condition. The right hand side of (2.21) for the solution (2.20) is represented with the finite difference approximation (2.11) by

$$\left.\frac{\partial f}{\partial x}\right|_{x=\delta xj}^{t=\delta tn} = \frac{\mu_{\omega,k}}{\delta t} f(\delta xj, \delta tn), \tag{2.22}$$

where

$$\mu_{\omega,k} = i\alpha\left(\frac{1}{6}\sin 4\theta - \frac{4}{3}\sin 2\theta\right) \tag{2.23}$$

$$\alpha = \omega\delta t/k\delta x \tag{2.24}$$

$$\theta = k\delta x/2. \tag{2.25}$$

Substituting (2.22) for (2.15)-(2.19), we obtain the Fourier transformation $G_{\omega,k}$ for each one step of time integration as

$$f\left(\delta xj, \delta t(n+1)\right) = G_{\omega,k} f\left(\delta xj, \delta tn\right) \tag{2.26}$$

$$G_{\omega,k} = 1 + \mu_{\omega,k} + \frac{\mu_{\omega,k}^2}{2} + \frac{\mu_{\omega,k}^3}{6} + \frac{\mu_{\omega,k}^4}{24}. \tag{2.27}$$

On the other hand, the exact solution (2.20) gives the wave function at $t = t + \delta t$ as

$$f\left(\delta xj, \delta t(n+1)\right) = f\left(\delta xj, \delta tn\right)\exp\left(-2i\alpha\theta\right). \tag{2.28}$$

Comparing (2.26), (2.28), we obtain the amplification factor $g_{\omega,k}$ for a time step as

$$g_{\omega,k} = G_{\omega,k}\exp\left(2i\alpha\theta\right). \tag{2.29}$$

Figure 2.2 shows the absolute value and the argument of $g_{\omega,k}$. To obtain a numerically stable solution, it is necessary to solve the equation under the condition that the amplification factor $|g_{\omega,k}|$ is always less than unity, and it is preferable that $|g_{\omega,k}|$ and $\arg g_{\omega,k}$ is close to 1 and 0, respectively. It can be seen in Fig.2.2 that this condition is satisfied in wide range of α. Especially, it has an excellent property for large wavelength (small k , θ) components, which is thought to play an important role for the relaxation phenomena in ST plasma.

The value of δt used in the simulation should be carefully selected to satisfy the stability condition described above. However, too small value of δt cause an undesirable accumulation of numerical error. Therefore, we should choose as large value as possible for δt, unless the stability condition is broken. Thus, we set the time interval to be $\alpha \sim 1$ for $\omega/k \sim v_A$, where v_A is the Alfvén velocity ($v_A = B^2$). This condition is examined at the most severe grid, that is, at the inner most boundary. The time interval is reset at each time step of Runge-Kutta integration. Furthermore, the time step is reduced not to change the values of each variable so much in one time step, while the system evolves nonlinearly. Normally, the time step is about $4 \times 10^{-3}\tau_A$, and is reduced into a few percents at the minimum.

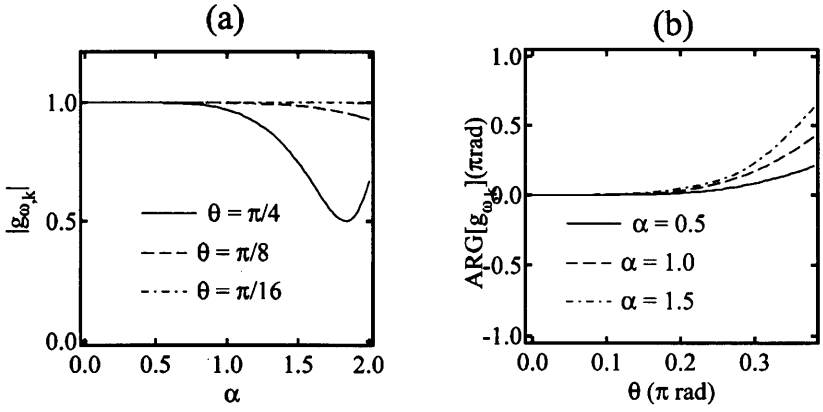

Figure 2.2: The amplification factor of the simulation scheme. (a) The absolute value and (b) the argument of $g_{\omega,k}$ is plotted.

2.4 Initial condition

2.4.1 Numerical solution of ST equilibrium

The initial condition for the simulation is given as an equilibrium obtained by solving the Grad-Shafranov equation numerically. The Grad-Shafranov equation for cylindrical geometry is expressed by

$$\begin{aligned} \triangle^* \Psi &= -r^2 \frac{dP}{d\Psi} - F\frac{dF}{d\Psi}, \\ \triangle^* &\equiv r\frac{\partial}{\partial r}(\frac{1}{r}\frac{\partial}{\partial r}) + \frac{\partial^2}{\partial z^2} \end{aligned} \tag{2.30}$$

where Ψ is a stream function for the poloidal magnetic field. The poloidal magnetic flux is equivalent to $2\pi\Psi$. The poloidal magnetic field is given by

$$B_r = -\frac{1}{r}\frac{\partial \Psi}{\partial z}, \tag{2.31}$$

$$B_z = \frac{1}{r}\frac{\partial \Psi}{\partial r}. \tag{2.32}$$

In (2.30), two free functions $p(\Psi)$ and $F(\Psi)$ are included. $p(\Psi)$ is the plasma pressure given as a magnetic flux surface quantity. $F(\Psi)$ is the poloidal current function, which is related to the toroidal magnetic field by

$$B_\theta = -\frac{1}{r}F(\Psi) \tag{2.33}$$

It is necessary to assume these functions to solve (2.30). In this simulation, we assume a simple polynomial form as follows.

$$p(\Psi) = p_0 \Psi_n^\alpha \tag{2.34}$$
$$F(\Psi) = F_0(\Psi_n^\beta + F_{ex}) \tag{2.35}$$

where Ψ_n is the normalized poloidal flux: $\Psi_n = 1$ at the magnetic axis and $\Psi_n = 0$ at plasma-vacuum boundary. We control each parameter iteratively to obtain a reasonable equilibrium in terms of the beta value, the shape of the poloidal cross section, the safety factor, and so on.

By solving (2.30) numerically on the poloidal cross section, we obtain $\Psi(r, z)$ at equilibrium state. The two-dimensional magnetic field ($\boldsymbol{B}_{GS}(r, z)$) and the pressure ($p_{GS}(r, z)$) at equilibrium state are derived by substituting the solution $\Psi(r, z)$ for (2.31)-(2.34).

2.4.2 Initialization for the nonlinear simulation

The nonlinear simulation is executed in a full toroidal three-dimensional geometry as described in Sec. 2.1. The two-dimensional equilibrium which is obtained by the procedure described in the previous subsection is converted into the three-dimensional field quantities as follows. The magnetic field and pressure is extended into axis-symmetric variables from the two-dimensional equilibrium.

$$\boldsymbol{B}(r, \theta, z) = \boldsymbol{B}_{GS}(r, z) \tag{2.36}$$
$$p(r, \theta, z) = p_{GS}(r, z) + p_{vac} \tag{2.37}$$

Here, we suppose that the outside region of the separatrix is filled with uniform low pressure plasma. One can see from (2.2) that the motion of plasma is affected by the gradient of the pressure, so that the equilibrium condition is not broken even if the uniform pressure p_{vac} is biased all over the simulation region. If this treatment is not applied, the calculation cannot be continued into a highly nonlinear regime. Thus, we add 10% of the maximum pressure as p_{vac}. The mass density is assumed to be uniformly $\rho(r, \theta, z) = 1$ at initial state.

If the equilibrium is unstable, tiny perturbation such as numerical error between the real equilibrium and the initial condition grow spontaneously. We will focus on such spontaneous development of MHD instability. However, such unexpected perturbation is not preferable to know the nature of the instability. To avoid the misleading from the unexpected perturbation, we start the nonlinear simulation from an artificially perturbed equilibrium. The amplitude of the perturbation added here should be small enough not to distort the configuration, and large enough to conceal the unexpected perturbation. The perturbation is composed to include any toroidal and poloidal wave numbers as

$$v_i(r, \theta, z) = \sum_{n=1}^{n_{max}} A_{i,n}(r, z) \sin\{n\theta + \zeta_n(r, z)\}. \tag{2.38}$$
$$(i = r, \theta, z)$$

The toroidal wave number n is explicitly included in (2.38). The maximum toroidal mode number n_{max} included in the perturbation is set to be 16, which is enough to cover the toroidal mode numbers concerned in the simulation. The poloidal mode number, on the other hand, is difficult to be defined in a rectangular numerical mesh. Therefore, we use quasi-random numbers for the amplitude $A_{i,n}$ at each mesh point on a poloidal cross section. The total amplitude for each poloidal wave number is approximately the same. Moreover, the toroidal phase ζ_n is also generated by quasi-random numbers to prevent any artificial correlation among each toroidal wavenumber. Here, $A_{i,n}$ and ζ_n are distributed in the range of

$$-5 \times 10^{-6} \leq A_{i,n} \leq 5 \times 10^{-6} \tag{2.39}$$

$$0 \leq \zeta_n \leq 2\pi. \tag{2.40}$$

By these treatment, the artificial perturbation includes any toroidal and poloidal wavenumbers at the same amplitude independently each other. It should be noted that the toroidal phase ζ_n is also independent among each mode. This fact will take on importance when we consider the interaction among the linear eigenmodes, which will be discussed in Sec.4.3.

2.5 Boundary condition

There are three kinds of boundary in the simulation region:

- inner boundary($r = r_{min}$) (center rod),
- outer boundary($r = r_{max}$),
- top ($z = z_{max}$) and bottom ($z = z_{min}$) boundaries.

In the real experiments, the center rod is made of metal, and is thought to play an important role for stabilizing of the ST equilibrium[52]. Therefore, it is preferable for us to treat the inner boundary as a perfect conducting wall to realize such effects in our simulation. The boundary condition for a perfect conductor is represented by

$$\boldsymbol{B}_{\perp} = const. \tag{2.41}$$

In the simulation, we can introduce this condition by forcing (2.41) on the relevant component of the magnetic field at the innermost mesh for each time step.

The other boundaries should be also properly modeled to reproduce the real situation in the experiment keeping any physical validity. In the real experiments, the plasma close to boundary is at low pressure and is governed by several complicated processes such as the recombination, the secondary electron, the reflected backward flow of plasma, and the impurity. Therefore, the dynamics in the periphery of the boundaries has not been clarified yet. In fact, a slight much care at the boundary, especially at the divertor, can make the property of bulk plasma much better. The effect of boundary condition can be

important also in the simulation. In particular, since the information is transmitted fast along the magnetic field, the effect of the top and bottom boundaries, where the magnetic field lines are passing through, tend to be significant on the simulation results. On the other hand, the outer boundary does not affect the results so much.

Here, we assume again the perfect conducting wall as the boundary condition for all the outer, the top, and the bottom boundaries. Since the real boundaries in experiments are usually made of metal, the most reasonable condition for boundaries is the perfect conducting wall, if the complicated effect described above and the finite size of numerical mesh are ignored. Ideally, such effect, that is, the rapid loss of plasma by recombination on the wall, or cooling by heat conduction, should be modeled properly. However, we adopt a simple model here as a principal approach. In addition, simpler model is better for treating complicated phenomena in our experience.

To check the effect of the top and the bottom boundaries, we executed simulation in other geometry where the boundaries are located further. The detail will be described in Appendix.

Chapter 3

Simulation result

3.1 Overview of simulation results

The simulation results that are executed under the condition described in the previous chapter show that the perturbations introduced on the initial equilibria grow spontaneously. That is because the initial equilibria are unstable ones. In this chapter, the details of the simulation results are described. Before going into the main argument, the outline of the simulation results are described in this section.

The initial equilibria that are maintained by the balance of the pressure gradient and the Lorentz force sometimes become unstable under certain conditions. A tiny perturbation introduced on such unstable equilibria can grow its amplitude with a specific eigenfunction. In the early stage of the growth, the perturbations grow exponentially with such eigenfunction, but the amplitude is still small enough not to affect the overall configuration so much. This stage of the growth may be called the 'linear stage', which is described in Sec.3.2. The eigenfunction consists of multiple mode components. Especially, low-n ones have larger growth rate and amplitude. These mode components grow independently each other. However, in the latter stage of the growth, the amplitude of each mode becomes large enough to cause an interaction among the modes. The time development after that may be called the 'nonlinear stage', which is described in Sec.3.3.

In the early nonlinear stage, many higher modes break into a rapid growth by nonlinear couplings between the low-n modes. The amplitude of the displacement reaches visible scale, and the growth is saturated because of the change in the overall configuration. The most remarkable change in the overall shape is the appearance of a localized pressure bulge, and the subsequent occurrence of a magnetic reconnection between the internal and the external magnetic field. The plasma pressure confined inside the separatrix is expelled out through the reconnection, and the structure is destroyed. The expelled plasma pressure forms a characteristic conical shape at the top and the bottom of the torus.

After dissipating the fine structures, a more stable axisymmetric configuration appears again. This configuration is unstable to resistive modes, so that perturbation can grow with the large resistivity. This stage may be called the 'second step' of the growth. Sec.3.4 is spent on describing the second step growth.

The parameters used in the simulation is listed in Table 3.1. The main result is

Table 3.1: Parameters used in the simulation.

	A	B	C	D	E	F
A	1.5	1.5	†	†	†	†
κ	1.9	2.1	†	†	†	†
β_0	0.44	0.41	†	†	†	†
$<\beta>$	0.081	0.083	†	†	†	†
β_T	0.12	0.13	†	†	†	†
q_0	0.91	1.06	†	†	†	†
μ	4×10^{-4}	†	1×10^{-4}	1×10^{-3}	†	†
η	1×10^{-5}	†	†	†	4×10^{-6}	2×10^{-5}

†: same as A

included in case A. In the following subsections, therefore, the detail of the simulation result for case A is described. Comparison with other parameters of case B is described in Sec.4.2. Cases C - F are used to investigate the dependence on the dissipation terms such as the viscosity and the resistivity. The analysis for them is described in Sec.3.2.

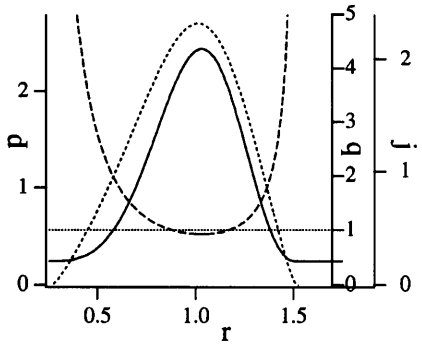

Figure 3.1: Radial profiles of the pressure, the toroidal current, and the safety factor in the initial equilibrium for case A,C,D,E, and F.

The radial profiles of the pressure, the toroidal current, and the safety factor (q value) of the initial equilibria are shown in Fig.3.1. All of them are in a kind of bell shape, not flat, and not hollow. The safety factor can be estimated by tracing the magnetic field line and using the following relation[56]:

$$q = \frac{rB_\theta}{2\pi} \oint \frac{dl_p}{r^2 B_p}, \tag{3.1}$$

where the line integral corresponds to one poloidal circuit, and B_p equals to the poloidal magnetic field. It should be noted that the central safety factor is slightly smaller than unity for case A, and greater for case B. Therefore, the $q = 1$ rational surface is included

for case A, and excluded for case B. Thus, we can investigate the role of the $q = 1$ surface in the relaxation phenomenon. These parameters correspond to the experimental operation regime in START.

3.2 Linear instability

3.2.1 Linear growth of instability

The tiny perturbations which are added to the initial equilibrium grow spontaneously due to the instability. Shown in Fig.3.2 is the time development of total magnetic energy for each toroidal Fourier component(n). It can be seen that multiple number of components grow exponentially during $t = 30 - 120\tau_A$ (τ_A is the Alfvèn transit time that is introduced in Sec.2.2.2). We call hereafter this period the 'linear stage'. In the linear stage, the amplitude of the perturbation is so small that the mode components grow independently of each other. Incidentally, before $t = 30\tau_A$ the magnetic energy for each mode decreases from 10^{-12} to some extent. The reason is that any toroidal and poloidal components are included in the initial condition, and the stable ones are damped.

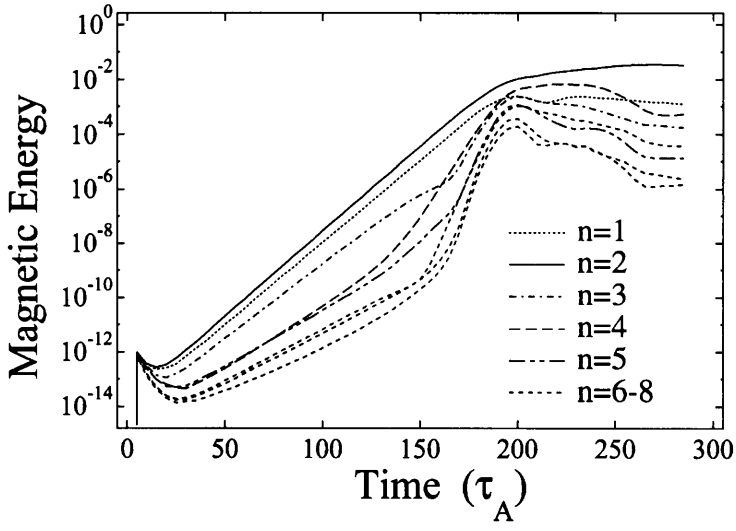

Figure 3.2: Time development of the total magnetic energy for each toroidal Fourier components.

As we can see from Fig.3.2, low-n modes have large amplitude and growth rate. To make a quantitative discussion, we estimate the growth rate for each mode (γ_n) from the data in Fig.3.2 by

$$\gamma_n = \frac{\Delta (\ln E_m)}{\Delta t}/2. \tag{3.2}$$

Figure 3.3 shows the growth rate for each mode defined by (3.2). For case A, it can be seen that the $n = 2$ mode has the largest growth rate, and that the $n = 1$ mode has the second largest one, which is close to that of the $n = 2$ mode. As for other higher modes, the lower-n modes have larger growth rate than the higher-n modes, but not so large as the $n = 2$ and the $n = 1$ modes. Moreover, the $n \leq 7$ modes are well damped. This fact makes sure of the numerical validity. Thus, the nonlinear behavior described in Sec.3.3 is determined by lower-n modes, especially, almost only the $n = 2$ and the $n = 1$ modes.

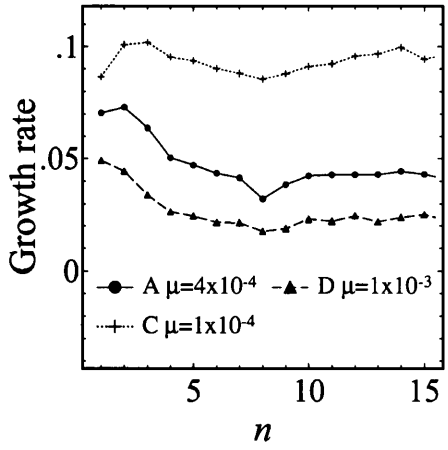

Figure 3.3: Growth rate of the linear eigenmodes for cases A, C, and D.

On the other hand, for case C, in which the viscosity is smaller than that for case A, the damping by the viscosity does not become effective, so that the growth rate for each mode is larger than that for case A. Especially, $n \geq 8$ modes have pretty large growth rate. Such high-n activity cannot be treated properly in our simulation which use a finite difference scheme in a discrete numerical grid system because of lack of numerical grid. Besides, experimentally, the low-n activity is thought to play more important role in the relaxation phenomena in ST. Therefore, our simulation should also focus on such low-n activity. The viscosity should be set to be large well enough to damp the high-n modes. Too large viscosity, such as case D, however, will cause an undesirable damping and saturation of growth. Thus, we use an appropriate value for the viscosity of $\mu = 4 \times 10^{-4}$ for case A.

3.2.2 Mode structure

In this section, we discuss the detail of the mode structure of the linear instability. Shown in Fig.3.4 is the poloidal structure of the fluctuation component in the pressure[(a),(b)] and the flow[(c),(d)] for the $n = 1$ [(a),(c)] and the $n = 2$ [(b),(d)] modes. The solid and the dotted contour in Figs.3.4(a) and (b) denote the positive and the negative perturbation in pressure, respectively. It can be seen from Figs.3.4(a) and (b) that the main poloidal component for the $n = 1$ mode is $m = 1$(m is poloidal mode number). For $n = 2$ mode, the most dominant poloidal component is the $m = 2$ one in the inner region and tiny

$m = 3$ perturbation can be seen in the outer region. On Figs.3.4(a) and (b), the position of the $q = 1$ rational surface and the separatrix are specified with broken line. It can be seen that both of the main $m = 2/n = 2$ and the $m = 1/n = 1$ modes are resonant to the $q = 1$ surface. Moreover, it should be noted that the perturbation is not localized in the poloidal direction. In other words, the amplitude of the perturbation in pressure is almost the same in the good and the bad curvature regions. Shown in Figs.3.4(c) and (d) is the poloidal flow pattern represented with arrows corresponding to the poloidal velocity. It can be seen that there are m pairs of vortices in a poloidal cross section. With this visualization, only the most dominant mode, that is, $m/n = 2/2$ and $1/1$ component can be seen. It should be pointed out that these poloidal flow pattern will cause a deformation if the amplitude become larger; the $m = 2$ flow will make the poloidal cross section more elliptic, and the $m = 1$ flow will shift the center of the poloidal structure away.

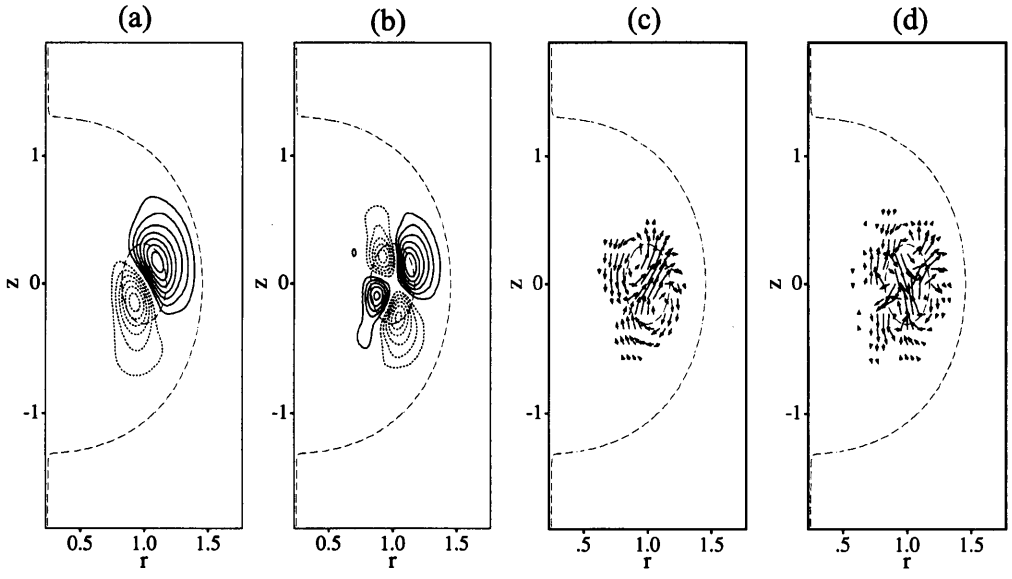

Figure 3.4: Poloidal mode structures of the linear eigenmodes. Perturbation components in (a) pressure for the $n = 1$ mode, (b) pressure for the $n = 2$ mode, (c) poloidal flow for the $n = 1$ mode, and (d) poloidal flow for the $n = 2$ mode. Solid and dotted lines denote the positive and the negative perturbations in the contour maps. The broken lines indicates the location of the separatrix and the $q = 1$ rational surface.

The three-dimensional structure of these modes is shown in Fig.3.5 with an iso-surface plot of the fluctuation component in pressure for the $n = 1$[(a)] and the $n = 2$[(b)] modes. It can be seen that there are n pairs of positive and negative fluctuation. The region where the pressure fluctuation becomes positive corresponds to the region where the plasma flow is gathered. It should be pointed out that there is no specific relationship in the structure between the $n = 1$ and the $n = 2$ modes. It is reasonable that they can glow independently each other because the system is axisymmetric, and because there is no relation between modes in the initial perturbation. This fact becomes important when we discuss about the nonlinear growth, which is described in Sec.3.3.

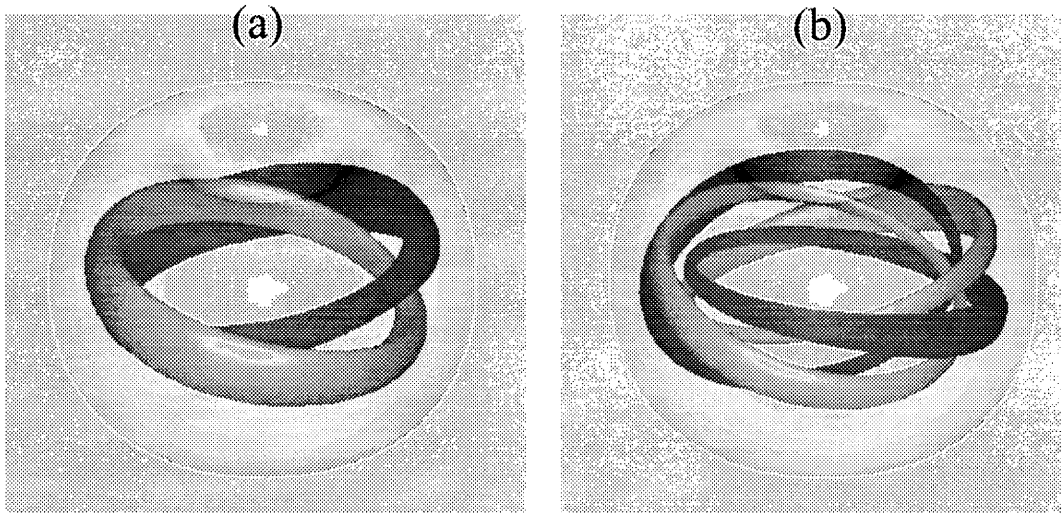

Figure 3.5: Three-dimensional mode structure of (a)$n = 1$ and (b)$n = 2$ component for the linear eigenmodes. Dark and light gray surface denote the positive and the negative perturbation in pressure. The semitransparent surface is the iso-contour surface of total pressure.

3.2.3 Identification of modes

As described in the previous subsection, low-n modes that correspond to those observed in experiment preceding to relaxation phenomena. It is worth considering the identity of such low-n instability. There are several ways to classify the instability.

First of all, we consider whether these modes are the ideal mode or the resistive one. In order to distinguish the resistive mode from the ideal mode, it is sufficient to see how the growth will change when the resistivity η is increased. Shown in Fig.3.6 is the growth rate for each toroidal mode for case A, E, and F. The only difference among these case is the value of η. It can be clearly seen that the growth rate for the higher-n ($n \geq 4$) modes is sensitive to the change in the resistivity. The growth rate for these modes are larger for larger resistivity. Therefore, it can be said that these modes have a nature of resistive mode. On the other hand, the changes in the growth rate for the low-n modes such as the $n = 2$ and the $n = 1$ modes, which are our interest, are much smaller than those in the higher-n modes. Thus, we can conclude that the low-n modes are the ideal modes.

Let us consider the driving source of the instability. It is useful for this purpose to make use of the energy principle[57] in order to estimate the change in the potential energy due to the displacement caused by the growth of the instability. The most illuminating expression for the energy principle is the form first derived by Greene and Johnson[58]. The change in the volume integrated potential energy (δW) for given displacement $\boldsymbol{\xi}$ is written by

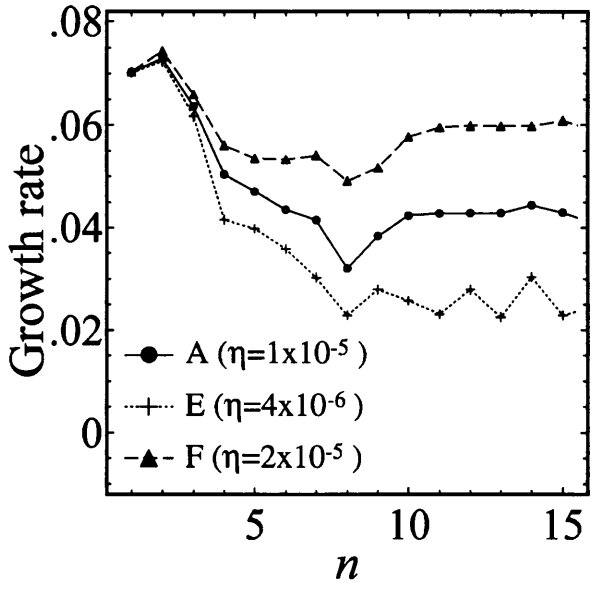

Figure 3.6: Same as Fig.3.3, but with the plot for cases E and F.

$$\delta W = \frac{1}{2}\int dV \left\{ \left|\boldsymbol{B}_{\perp}^{1}\right|^{2} + \left|\boldsymbol{B}_{\parallel}^{1} - \frac{\boldsymbol{B}^{0}\left(\boldsymbol{\xi}\cdot\nabla p^{0}\right)}{\left|B^{0}\right|^{2}}\right|^{2} + \gamma p^{0}\left|\nabla\cdot\boldsymbol{\xi}\right|^{2} + \frac{\boldsymbol{j}^{0}\cdot\boldsymbol{B}^{0}}{\left|B^{0}\right|^{2}}\boldsymbol{B}^{0}\times\boldsymbol{\xi}\cdot\boldsymbol{B}^{1} - 2\left(\boldsymbol{\xi}\cdot\nabla p^{0}\right)\left(\boldsymbol{\xi}\cdot\boldsymbol{\kappa}\right)\right\}, \tag{3.3}$$

where the superscripts 0 and 1 refers to the value at the equilibrium and the perturbation component, respectively, and the subscripts $\perp$ and $\parallel$ denotes the perpendicular and the parallel component to the equilibrium magnetic field, respectively. $\boldsymbol{\kappa}$ is the magnetic field curvature defined by $\boldsymbol{\kappa} = \boldsymbol{b}\cdot\nabla\boldsymbol{b}$, where $\boldsymbol{b}$ is the unit vector along the magnetic field. The volume integral is done over the region where it is filled with plasma. In this simulation, however, the plasma and the vacuum region are continuously faced each other, and it is difficult to specify the boundary between them. For simplicity, we estimate the potential energy integral (3.3) by integrating over whole volume in the simulation region. This treatment is justified by the fact that the displacement is seen only inside the separatrix in the linear stage. (3.3) is an illuminating form to understand the driving source of the instability when $\boldsymbol{\xi}$ is substituted by the eigenfunction that is obtained in the simulation result. Negative change in the potential energy integral means a destabilizing effect of the displacement. The first three terms appearing in the right hand side of (3.3) corresponds to the change in the potential energy of the Alfvèn wave, the fast magnetoacoustic wave, and the acoustic wave. In other words, these terms refer to the required energy for bending the magnetic field, compressing the magnetic field, and compressing the plasma pressure, respectively. These terms are positive definite, so that they have a stabilizing effect. Only the last two terms can be negative. The fourth term, in which the equilibrium current is

Table 3.2: Estimation of the change in total potential energy by using the energy principle. All the terms are normalized by the absolute value of the kink term for each mode.

term	$n = 1$	$n = 2$
kink	-1	-1
interchange	-6.6	-15.3
Alfvén	5.0	11.3
fast magneto acoustic	0.7	0.8
acoustic	0.4	1.2
total	-1.4	-3.0

included, is related to the current-driven instability, which is so-called kink mode. The last term is based on the pressure gradient, and is related the pressure-driven instability, such as the interchange and the ballooning modes. By comparing the value of the current-driven and the pressure-driven terms in (3.3), we can classify the instability into the two categories. The estimation for the $n = 1$ and the $n = 2$ mode in the simulation result is listed in Table 3.2.

Here, we derive the displacement vector for each mode from the simulation result as $\boldsymbol{\xi_n} = \boldsymbol{v_n}/\gamma_n$, where γ_n is the growth rate defined by (3.2). Both the current-driven and the pressure-driven terms come out to be negative for both the $n = 1$ and the $n = 2$ modes. Therefore, the instability is driven by the combination of the effect of both the current and the pressure gradient. Furthermore, it can be seen that the pressure-driven term is much larger than the current-driven term for both the $n = 1$ and the $n = 2$ modes. Therefore, we can conclude that the instability has a nature of the pressure-driven modes both for $n = 1$ and the $n = 2$ modes. Incidentally, the fact that the sum of all terms is really negative for both the $n = 1$ and the $n = 2$ modes means that these modes are ideally unstable. It supports the conclusion that these modes are ideal mode.

Thus, we find these modes are categorized into an ideal pressure-driven mode. The last question about the linear instability is whether they are the interchange mode or the ballooning mode. The difference of the interchange mode and the ballooning mode is the existence of the parallel component to the magnetic field in the displacement vector. When $\boldsymbol{\xi}$ is perfectly perpendicular to the magnetic field, the instability is categorized into the interchange mode, and it may be called ballooning mode for any other cases. However, it is rare to see an interchange mode in such a strict sense in magnetically confined plasma. If the displacement is almost perpendicular to the magnetic field, we should recognize it as an interchange mode. Therefore, it is meaningful to discuss about the supporting evidence for these modes rather than to estimate the exact value of $\boldsymbol{\xi} \cdot \boldsymbol{B}$. The most noticeable supporting evidence of the ballooning mode is that the mode structure of the ballooning modes tend to be localized in poloidal cross section, because the growth of the mode is affected by the magnetic field curvature. Namely, it is localized in so-called 'bad curvature region', which correspond to the outer region of the torus. Another nature of the ballooning mode is the accompaniment of multiple poloidal modes. In contrast, the structure of the interchange mode extends equally along the magnetic field. The

interchange mode grows as forming a flute along magnetic field. We can see from Fig.3.4 that these modes have the nature of the interchange mode in that the poloidal mode patterns is uniformly distributed in the poloidal cross section. It will be confirmed well when we see the nonlinear development in the next section, where the displacement forms a flute along magnetic field.

Furthermore, if the eigenmode is an interchange mode, the Mercier criterion[59] must be broken at the unstable region. The Mercier criterion for interchange stability in the torus configuration with arbitrary aspect ratios is given by[60]

$$D_M < 1/4, \tag{3.4}$$

where

$$D_M = \frac{p'}{q'^2}\left[2\left\langle\frac{rB_p\kappa_n}{B^2}\right\rangle + \left\langle\frac{\Lambda}{B^4}\right\rangle - \left\langle\frac{1}{B^4}\right\rangle\left\langle\frac{\Lambda}{B^2}\right\rangle\right] \tag{3.5}$$

$$\Lambda = F\left(p'F - \frac{r^2B_p^2}{J}\frac{\partial\hat{q}}{\partial\psi}\right), \tag{3.6}$$

$$\langle\mathcal{Q}\rangle = \frac{\int_0^{2\pi}\frac{\mathcal{Q}B^2}{r^2B_p^2}Jd\chi}{\int_0^{2\pi}\frac{B^2}{r^2B_p^2}Jd\chi}. \tag{3.7}$$

Here, we use a flux coordinate (ψ, χ) represented by the Jacobian J, where ψ and χ correspond to the flux and the poloidal angle components, respectively. The prime denotes $d/d\psi$ and $F = rB_\theta$. The safety factor is calculated by using $\hat{q} = JB_\theta/r$ as $q = \int_0^{2\pi}\hat{q}d\chi/2\pi$. B_p and κ_n indicates the poloidal magnetic field density and the normal curvature, respectively. Shown in Fig.3.7 is the plot of D_M for the initial equilibrium of this simulation. It can be seen that the Mercier criterion is broken at the inner region including the $q = 1$ rational surface($\psi \sim 0.1$). It should be also noted that at the $q = 2$ rational surface ($\psi \sim 0.6$) the criterion is satisfied, so that the absence of $q = 2$ mode excitation in the simulation result can be explained.

Thus, we have found that the eigenmode of the linear instability on which we are focusing is categorized into an ideal pressure-driven interchange mode.

3.3 Nonlinear dynamics on relaxation phenomena

In this section, we investigate the dynamical behavior of ST plasma in the nonlinear stage[61, 62, 63, 64].

3.3.1 Weakly nonlinear development of low-n interchange mode

As we can see from Fig.3.2, the instability keeps growing linearly with the growth rates and the mode structures fixed as described in the previous section. The first sign of the nonlinearity appears as an abrupt change in the growth rate for the intermediate n

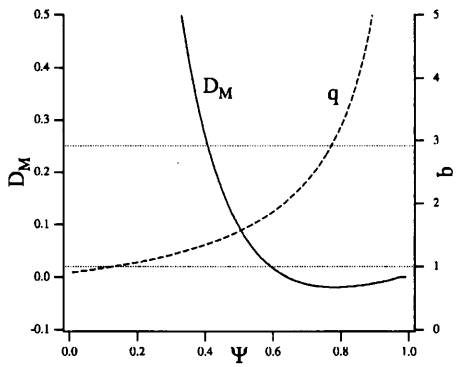

Figure 3.7: Estimation of interchange stability by Mercier criterion. $D_M < 1/4$ is needed for interchange stability.

modes. As shown in Fig. 3.2, the growth rate of the $n = 4$ mode suddenly increases at $t = 130\tau_A$. It implies the appearance of the higher harmonics for the $n = 2$ mode and the nonlinear couplings between the $n = 1$ and the $n = 3$ modes. Since amplitude of the $n = 1$ and the $n = 2$ modes are almost the same at that time, both of them can be the cause of the increase of the growth rate in the beginning of the nonlinear stage. As for other intermediate or higher n modes, similar excitement of higher nonlinear modes can be seen in Fig.3.2. After $t = 160\tau_A$, many higher nonlinear modes appear successively at large growth rate.

Figure 3.8 shows the magnetic energy spectrum at t =(a)120, (b)165, and (c)185τ_A. It can be seen that a disordered spectrum in the linear stage reflecting the independency among linear modes gradually changes into an ordered spectrum. At $t = 165\tau_A$[see Fig.3.8(b)], the higher harmonics of the $n = 2$ mode, such as $n = 4, 6, \cdots$ components, have larger amplitude than the neighboring odd n components. At $t = 185\tau_A$[see Fig.3.8(b)], the higher n components are well developed and the spectrum tends to be in line for higher n region. Such a cascade phenomena in the wavenumber space is generally observed in nonlinear system, These phenomena are usually related to a highly complicated mixing among modes. In this simulation, however, the resultant change in real space in the succeeding highly nonlinear stage is surprisingly simple, namely, a single large bulge of the plasma pressure appears in the subsequent stage, which is described in the next subsection. This is caused by the existence of a specific relation among the phases of these modes. Such analysis for the phases is discussed in Sec.4.3.

We can also pick another suggestive feature up from Fig.3.2 in the early nonlinear stage, that is, a slowing down of the growth of $n = 3$ mode at around $t = 150\tau_A$ before the successive excitation of higher nonlinear modes. Such a slowing down of the second or the third dominant modes is often observed in our simulation for other parameters, and similar behavior is also seen in another paper[65], which is concerned with a weakly nonlinear theory on the growth of Rayleigh-Taylor instability. Though the detailed analysis for this phenomenon has not been completed in this thesis, there are two possible explanation for this phenomenon. First one is the energy transportation in wavenumber space from

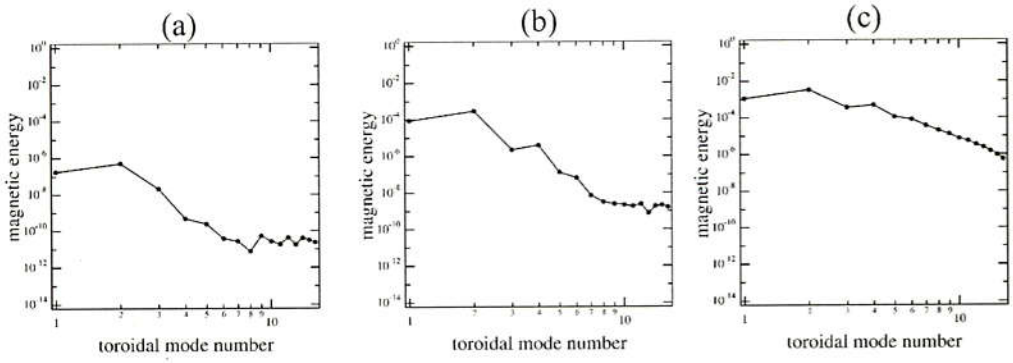

Figure 3.8: Temporal change in the energy spectrum. Time equals to (a)120, (b) 165, (c)185 τ_A, respectively.

lower modes to higher modes due to the cascade. Another one is a premature saturation of weaker modes. As described in Sec.4.3, a test simulation run with an artificial suppression of the $n = 1$ mode shows that the growth of the $n = 1$ mode and its higher harmonics reach the saturation at much lower level, and an early slowing down of the growth is observed. It implies that the growth of weaker modes are inhibited when the most dominant mode becomes at large amplitude so that it affects the growth of other modes. It may be likened to a natural selection. However, more detailed analysis for this phenomenon is beyond our scope in this thesis.

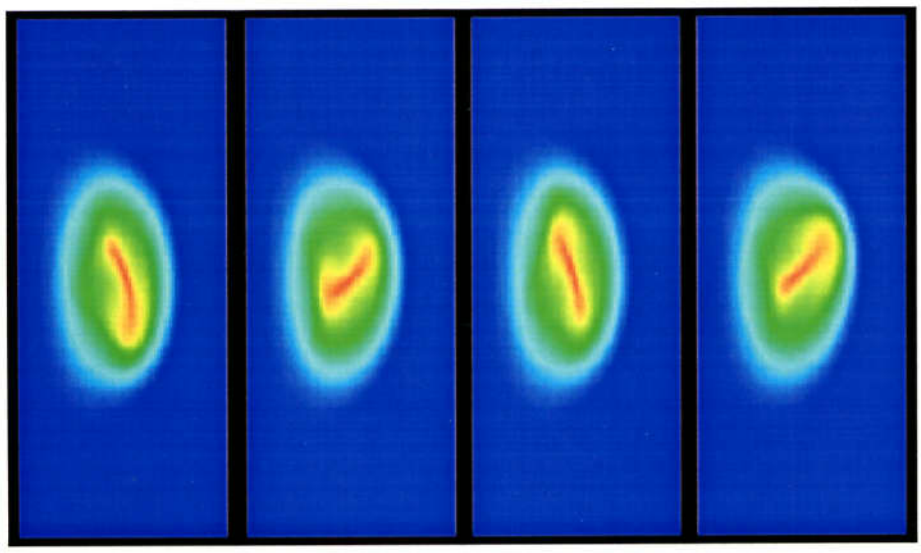

Figure 3.9: Change in the poloidal pressure profile at the weakly nonlinear stage. The net pressure is represented by color for four different toroidal angles perpendicular each other at $t = 180\tau_A$.

Finally, at the end of the weakly nonlinear stage at around $t = 190\tau_A$, the growth of

the dominant $n = 2$ and the $n = 1$ modes is saturated. The pressure profile on poloidal cross section for four toroidal angle perpendicular to each other at $t = 180\tau_A$ is shown in Fig.3.9. An elliptical deformation due to the $m = 2/n = 2$ mode and a shift of the center of profile due to the $m = 1/n = 1$ mode are clearly seen.

Though the magnetic energy for each mode is saturated at some level, the system goes into more dynamical regime, which may be called the 'highly nonlinear stage'.

3.3.2 Collapse and localized deformation

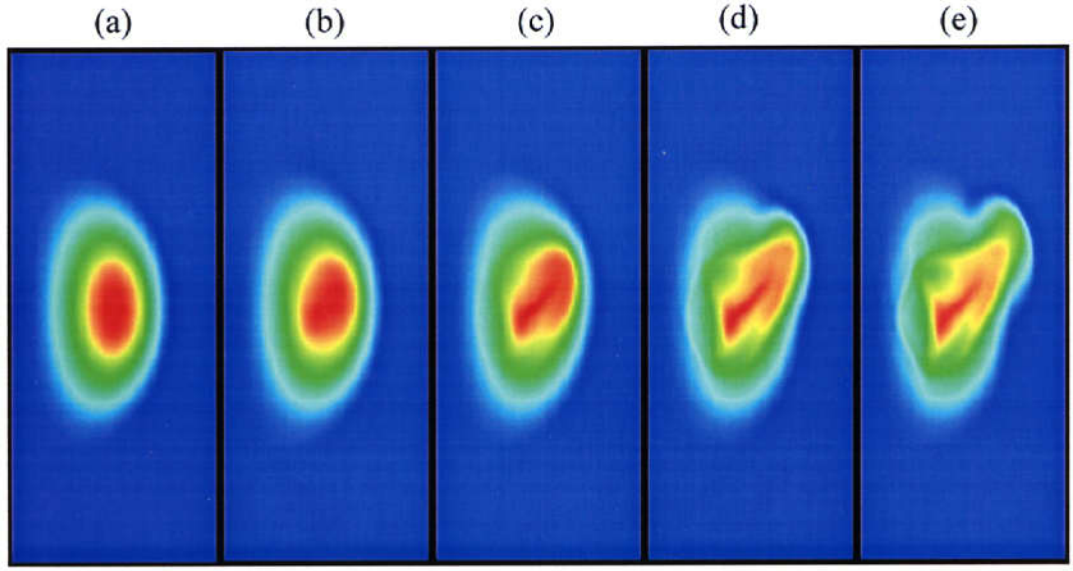

Figure 3.10: Time development of the pressure profile in the early nonlinear stage (a)t=0, (b)165, (c)180, (d))190, and (e)195 τ_A.

As the perturbation grows, the amplitude of the displacement becomes so large that a noticeable deformation appears in the global shape. Figure 3.10 shows the temporal change in the net pressure profile on a poloidal cross section. The displacement becomes a visible scale at $t = 165\tau_A$ [see Fig. 3.10(b)]. The pressure profile is elliptically elongated in the poloidal cross section reflecting the convection motion of the $m = 2/n = 2$ mode, as is described in the previous subsection. As time passes, the peak of the pressure profile is gradually shifted away because of the convection motion of the $m = 1/n = 1$ mode [see Fig. 3.10(c)]. At around $t = 190\tau_A$ [Fig. 3.10(d)], the displacement reaches near the separatrix. It is worthy of notice that although in the linear stage the instabilities have the nature of the internal modes as an interchange mode, they grow so much that even the outermost surface of the torus is deformed like an external mode in the nonlinear stage . Simultaneously, the plasma pressure at the core region is transported from the core to the edge by such development of the convection motions.

Figure 3.11 shows the time development of radial profile of (a) the plasma pressure and (b) the toroidal current on the midplane. It can be seen that the central pressure

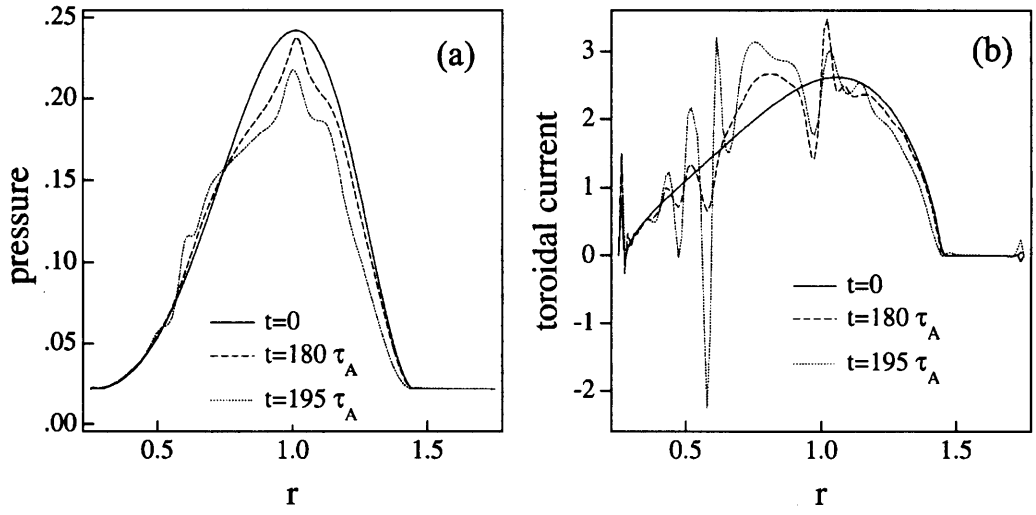

Figure 3.11: Temporal change in the radial (a)pressure and (b) toroidal current profiles on the midplane.

falls in several tens of τ_A, and the radial pressure profile changes from a bell-shaped one to a trapezoidal one. It should be noted that the current profile, on the other hand, is largely waving at around $t = 195\tau_A$.

As time goes further, the deformation due to the development of the instability forms a large bulge near the outermost surface at $t = 195\tau_A$[see Fig. 3.10(e)]. Shown in Fig.3.12 is the three-dimensional view of the deformation of plasma at $t = 195\tau_A$. The surface is an iso-contour of plasma pressure at a level near the outermost surface($p = 0.05$). The structure of the surrounding magnetic field is plotted together in Fig.3.12 by picking typical external field lines up. It can be clearly seen that a pressure bulge is formed in a narrow region of the torus which exists helically from the top down to the bottom of the torus. This bulge is formed along the external magnetic field as it pushes aside the neighboring external field lines. This deformation reminds us that the instability mode is an interchange mode. The displacement of an interchange mode grows perpendicular to magnetic field. It has a physical meanings that the interchange of plasma pressure is done without bending of the magnetic field. Therefore, the displacement of interchange mode extends uniformly along magnetic field.

Furthermore, it is worthy of notice that the deformation appears only one side of the torus. There is no visible deformation in the opposite side. It is mysterious, considering that the most dominant mode in the linear stage is not the $n = 1$ mode but the $n = 2$ mode, and that a lot of modes exist at this time as described in previous subsection. The reason why the number of the ridge of the deformation is reduced in the nonlinear stage is found to be the specific relation in the phase of modes each other.

Figure 3.13 shows a top view of a three-dimensional iso-contour surface of pressure for each mode at $t = 195\tau_A$. The net pressure is shown together with a semi-transparent iso-contour surface. The localized deformation exists at the upper right of each picture.

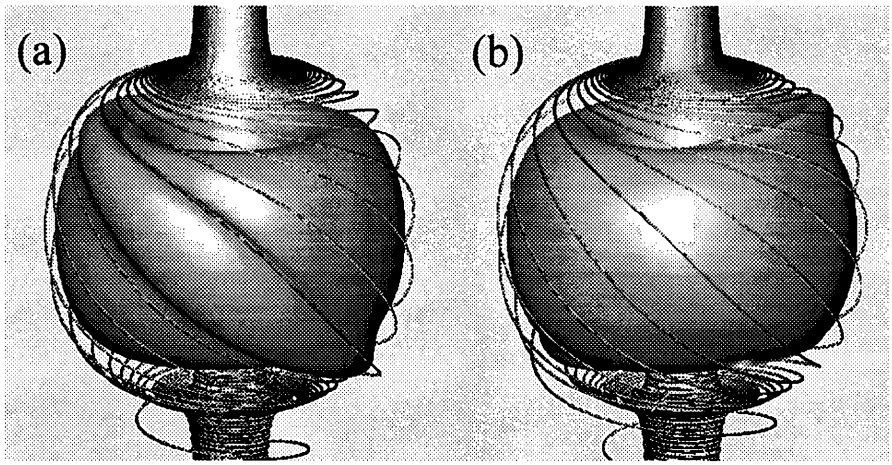

Figure 3.12: A localized deformation which appears at $t = 195\tau_A$. (a) and (b) are viewed from the different angles of 180 degs. apart each other in toroidal direction. The iso-pressure surface ($p = 0.05$) and the surrounding external magnetic field lines are plotted.

The positive and the negative perturbation component is indicated with dark and light gray surface, respectively. There are n pairs of the positive and the negative perturbation in each picture. It is clearly seen that one of the positive perturbation is aligned to the direction of the localized deformation for each mode. This is the direct cause for the formation of localized bulge. On the other hand, the opposite side of the localized deformation, the positive perturbation of even n modes and the negative one of odd n modes are aligned, so that the displacement is canceled out. The detailed discussion for the alignment in phases among modes is given in Sec.4.3.

3.3.3 Magnetic reconnection between internal and external fields

Due to the deformation of the surface, a large topological change in the configuration, namely, the magnetic reconnection, is induced on the surface of the torus. Both the inside and the outside of the separatrix are filled with plasma embedded in the magnetic field. As the localized deformation grows, the internal plasma is carried and pushed against the external magnetic field. If the magnetic field is sheared near the separatrix, a situation for causing a magnetic reconnection will be formed.

Shown in Fig. 3.14 are the magnetic field lines traced from a fixed point on the top conducting wall boundary at different time . The field line is traced numerically with high accuracy based on a fourth order interpolation of the magnetic field and a sixth order Runge-Kutta integration scheme. A field line outside the separatrix never passes through the separatrix at $t = 0$ [see Fig. 3.14(a)] because the initial equilibrium assumes the nested surfaces inside the torus. On the other hand, the field line traced at $t = 200\tau_A$ [see Fig. 3.14(b)] penetrates into the inner region of the torus passing through around the localized deformation. It proves that a magnetic reconnection actually occurs between the internal and the external magnetic field.

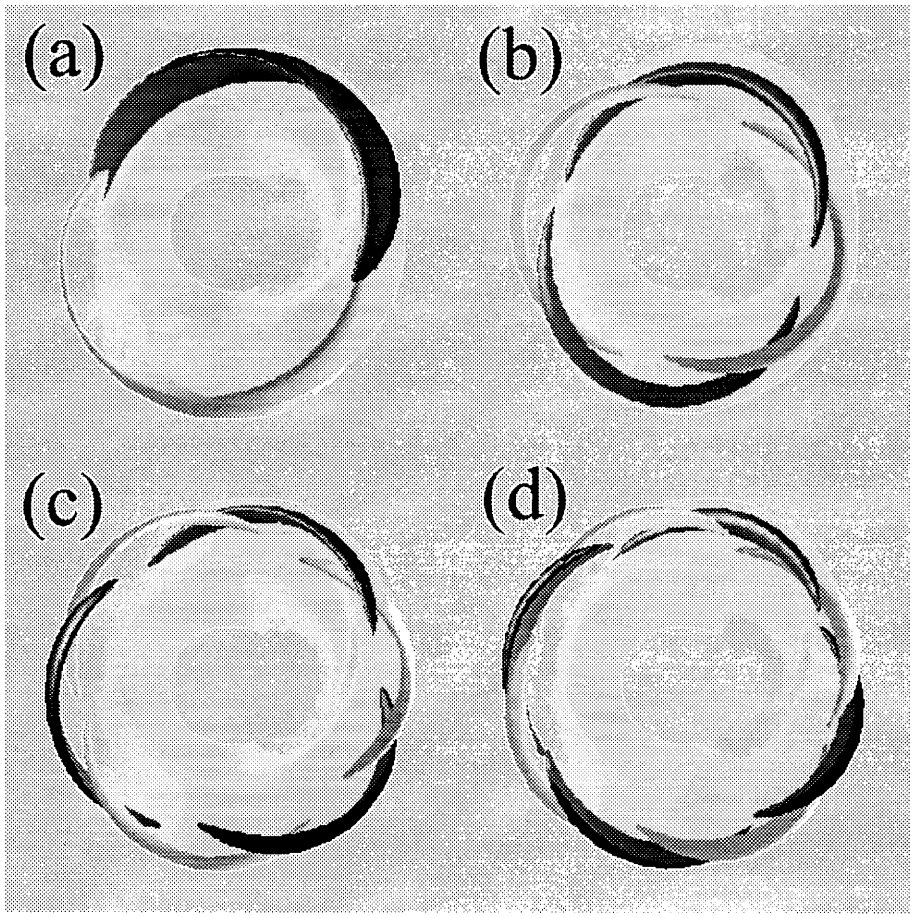

Figure 3.13: Three-dimensional structure related to the localized deformation at $t = 195\tau_A$. The perturbation component in pressure for (a)$n = 1$, (b)$n = 2$, (c)$n = 3$, and (d)$n = 4$ Fourier components are plotted together with a semi-transparent iso-surface of the net pressure.

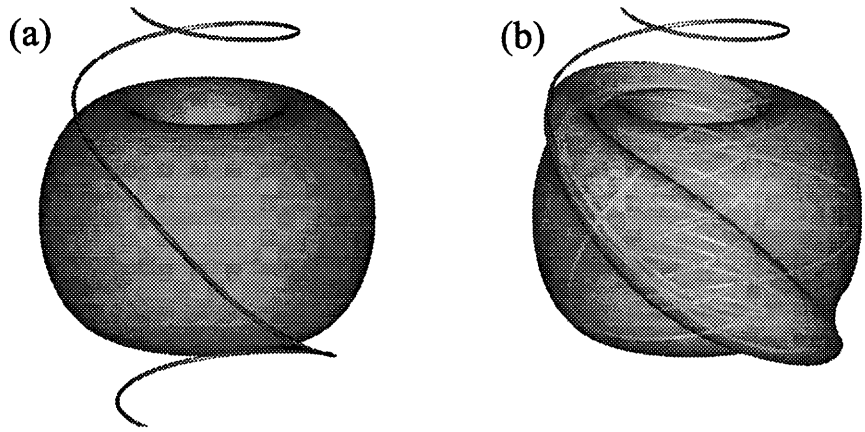

Figure 3.14: Magnetic reconnection between the internal and the external field. An identical magnetic field line and an iso-pressure surface near the separatrix is drawn for (a)$t = 0$ and (b)$t = 200\tau_A$. The magnetic field line is traced from a fixed point on the top boundary, and connects directly into the torus at $t = 200\tau_A$.

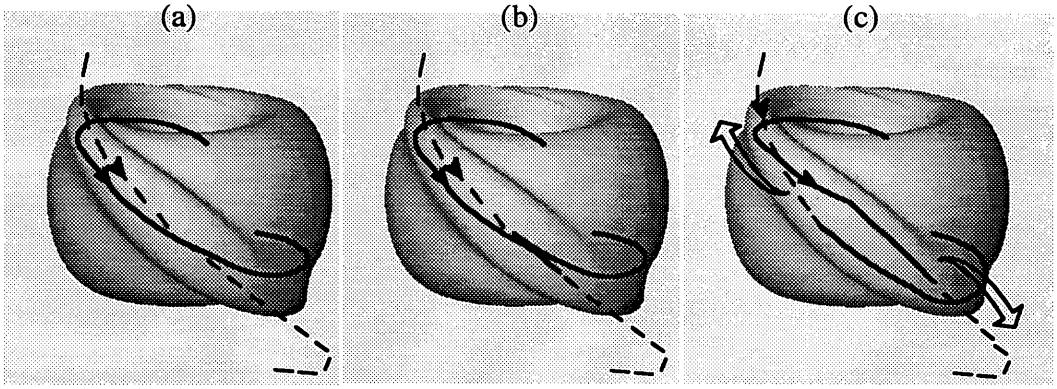

Figure 3.15: Schematic figure to explain the possible mechanism of the magnetic reconnection.

Let us consider the mechanism of this magnetic reconnection process. Figure 3.15 is a schematic diagram explaining this process. A pair of field lines relevant to the magnetic reconnection is drawn with solid and dashed lines together with an iso-contour surface of pressure. They are almost parallel but not perfectly to each other, and they lie on the opposite sides of the outermost surface [see Fig. 3.15(a)]. One is the line inside the torus (solid line) and the other is the open field line in the external region (dashed line). The internal field lines are moved by the convective flow and pushed against the external field just outside the pressure bulge. It enhances the formation of current sheet in a local region where the anti-parallel magnetic field is forced to be close to each other. Thus, the anti-parallel fractions of the magnetic fields are driven to be reconnected [see Fig. 3.15(b)] by enhancing a local current sheet[66]. Once the reconnection occurs, a part of field lines in the torus is directly connected with the external field lines so that a large pressure imbalance appears along the reconnected field lines. As we can see from the parallel component to the magnetic field of (2.2), the pressure gradient along magnetic field causes a generation of plasma flow along magnetic field. In this case, a pair of strong plasma flow from the inside toward the outside will be formed as indicated with fat arrows in Fig. 3.15(c). One bunch of flow goes upward, and the other goes downward, so that they cross each other in the localized bulge. The plasma pressure will be rapidly expelled out of the torus by such outward flow. This process is to be likened to put a hole on the surface of a rubber ball which contains air with high pressure. The reconnected field lines, on the other hand, are somewhat bent just after the reconnection occurs, and are to be stretched by releasing the magnetic tension. It enhances the relevant field lines to be distant further each other.

On the basis of this preliminary consideration, we examine the simulation result in detail. Figure 3.16 shows the three-dimensional structure of the vector field of the plasma flow and the magnetic field lines. The magnetic field lines are drawn with thick lines, and are colored in green to red in proportion to the local value of the plasma pressure (red refers to the higher pressure). The field lines passing the localized deformation emerges out of the torus and directly links to the external region. The pressure on them is definitely higher than that on the other field lines which exist entirely on the external region. It implies that the plasma pressure actually flows out of the torus along the reconnected field lines. The flow field is colored in red and blue depending on the sign of the toroidal component of the velocity, and the length of each line is in proportion to the absolute value of the flow. It is clearly seen that a pair of strong plasma flow is formed toward the top and the bottom of the torus originated from the inside of the torus. Interestingly, it is possible to go against the flow up to deep inside the torus. They are formed to cross each other at the localized deformation. These structures agree with the schematic picture shown in Fig. 3.15(c).

The magnetic reconnection process described above is a unique one in that (1) the relevant magnetic field lines are almost parallel, (2) the pressure on the magnetic field line to be reconnected is largely different from that on the field line, and (3) therefore, the dynamics of the system posterior to the reconnection is governed by the generated pressure gradient along the magnetic field.

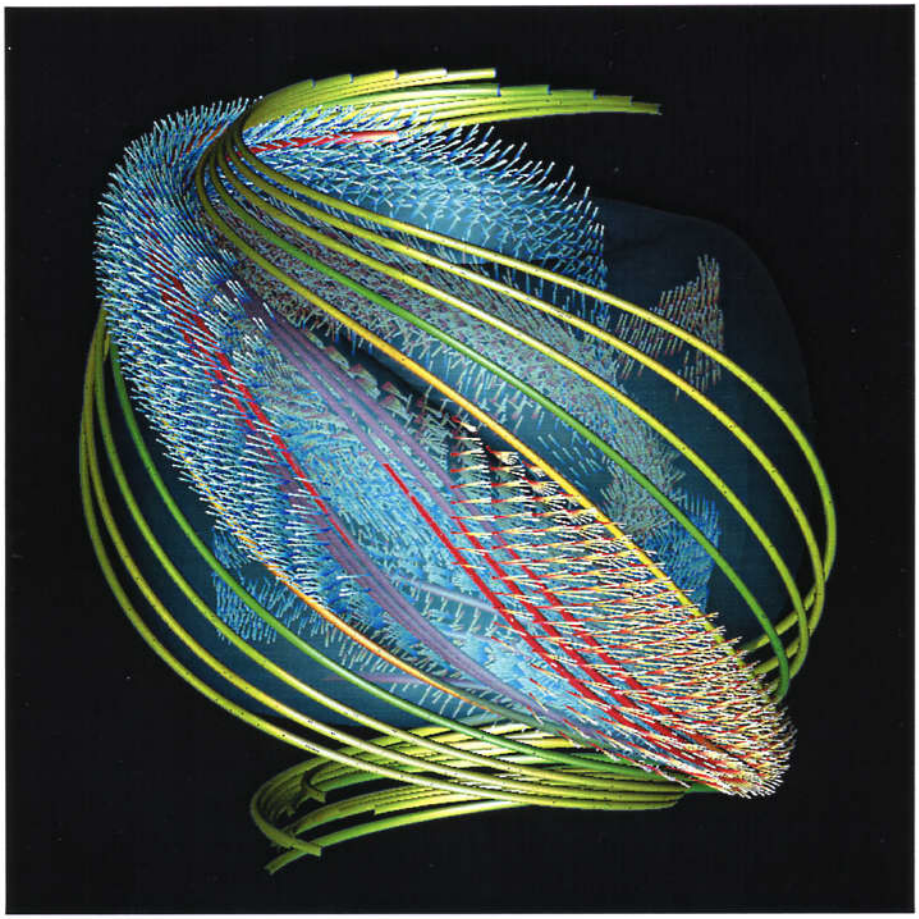

Figure 3.16: Three-dimensional structure of plasma pressure, flow and the magnetic field at $t = 200\tau_A$ in the simulation result. The semitransparent surface indicates the iso-contour of plasma pressure($p = 0.05$), the thick lines are the arbitrary traces of magnetic field lines, and the thin lines represents the plasma flows. The direction of the flow are represented by the variation of the color on the lines [from the blue (red) to the white]. The difference between the blue and the red is the sign of toroidal component of the fluid velocity. The magnetic field lines are colored in green to red corresponding to the local value of the pressure. (Red denotes higher region)

3.3.4 Convective loss of heat energy

The magnetic reconnection process described above has important meaning in the whole relaxation process in two points. One is that the topological structure of the torus is changed by the reconnection. The reconnection between the internal and the external magnetic field makes the definition of the inside and the outside of the torus obscure, and succeeding time development of the system becomes complicated. The other point is that the reconnected field line works as a channel for a convective loss of heat energy from the core region to the periphery[67]. Of course, both points are closely related, and become important simultaneously. In this subsection, we investigate the subsequent time development and the resultant loss of energy.

The outward plasma flow induced by the magnetic reconnection described in the previous subsection extends into a characteristic shape in the peripheral region of the torus. Shown in Fig.3.17 is the temporal change in the overall shape represented by an iso-contour of plasma pressure together with the surrounding magnetic field lines. The plasma pressure forms a pair of conical thin layers at the top and the bottom of the torus at $t = 250\tau_A$ as shown in Fig.3.17(c). The conical structure is originated from the localized deformation that is described in Sec.3.3.2. The resultant overall shape is a helically twisted one, and the plasma extends near the top boundary of the simulation region down to the vicinity of the bottom boundary. It can be seen as the overall shape of the torus is elongated vertically. The temporal change in the poloidal profile of plasma pressure at this stage is shown in Fig.3.18 as the continuation of Fig.3.10. It can be seen that the expelled plasma forms several thin layers surrounding the center rod at $t = 250\tau_A$ [Fig.3.18(b)]. The layers looks somewhat spread radially forming a vertically opened conical shape at the top and the bottom of the torus. We can see from Figs.3.17 and 3.18 at a glance that a considerable amount of plasma is lost from the core region. It should be noted that the core plasma at high pressure still remains at the center of the distorted torus, in spite of the massive expulsion of the plasma.

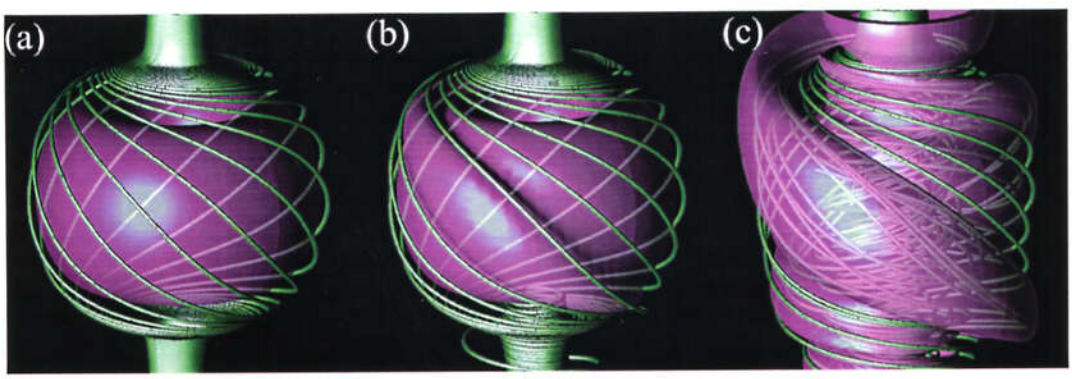

Figure 3.17: Nonlinear time development of the three-dimensional structures of the plasma pressure represented by iso-pressure surfaces and the surrounding magnetic field lines. The time equals to (a)0, (b)195, and (c)250 τ_A.

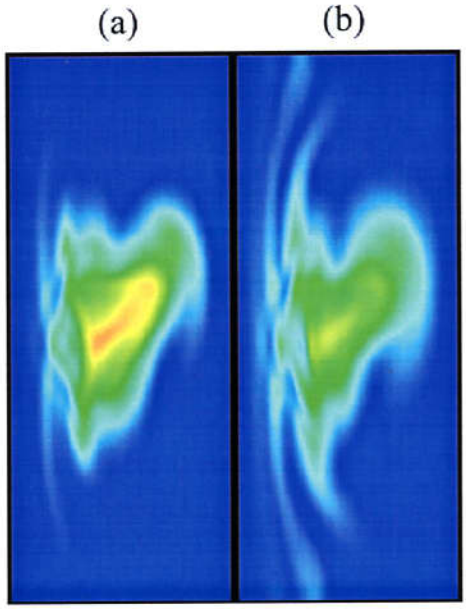

Figure 3.18: Sequel of Fig.3.10 at (a)t=215 and (b)250 τ_A.

To examine the plasma loss process in more detail, we trace the motion of fluid particle of plasma. The trace is done by following scheme. First of all the start point to be traced is specified at $t = 0$. The motion of fluid particle is calculated by integrating the fluid velocity in time. Therefore, the velocity must be given at any time and position. The best way to do this is to solve the motion of fluid particle simultaneously with the main simulation. However, for simplicity, we aim to obtain a rough estimation for the motion of fluid particle by using the data saved at every $5\tau_A$. The field data of velocity are interpolated in space and time by using a fourth order interpolation scheme. Thus, the time integration is calculated with the interpolated data by a fourth order Runge-Kutta method. Figure 3.19 shows the snapshots for the result of such traces of fluid particles. At $t = 0$ [Fig.3.19(a)] the test particles are placed inside the separatrix at regular interval in r, θ, and z direction. As the instability grows, the test particles begin to rotate mainly in toroidal direction[Fig.3.19(b)]. The particles are colored in red and blue depending on the sign of v_θ. The snapshots are represented with a finite 'exposure' time, that is, more active particles are drawn with longer streak lines. (However, each line is approximated by a straight line.) At $t = 175\tau_A$, a strong plasma flow rounding near the center of the torus appears in visible bunch of lines[Fig.3.19(c)] . This flow makes the localized bulge at $t = 190\tau_A$[Fig.3.19(d)]. After around this time, part of particles are expelled out of the torus, rounding fast around the torus[Fig.3.19(e)]. Thus, we find that the plasma placed inside the torus is actually lost in part.

Furthermore, let us focus on the motion of each particle. Typical streak lines traced from $t = 0$ up to $t = 250\tau_A$ are shown in Fig.3.20. Two traces are drawn in each figure. It is found that the streak lines are classified roughly into three types, though the border for each type is not so clear, and there are some particles that cannot be included in these

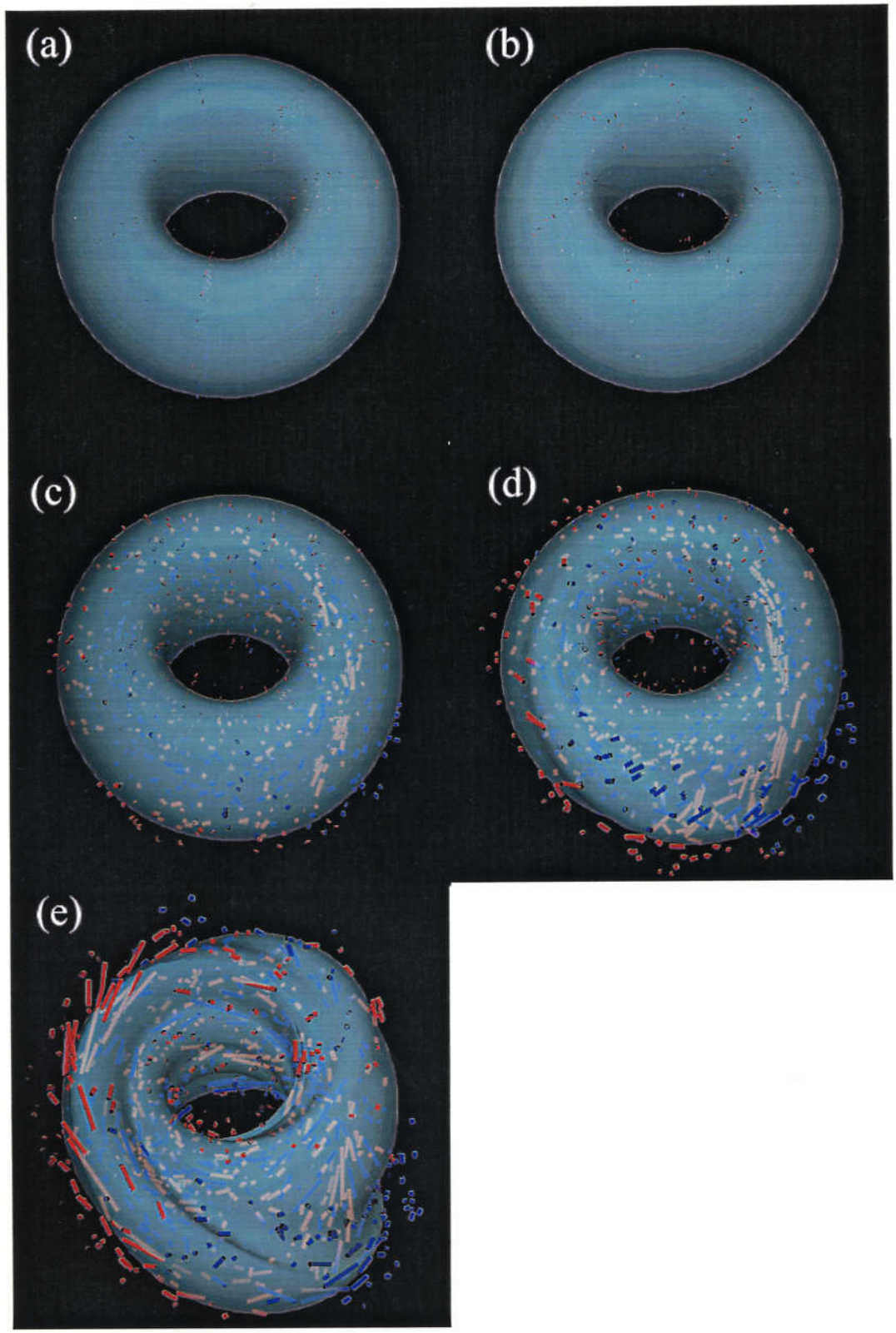

Figure 3.19: Snapshots of the tracing of the test fluid particles. Time equals to (a)0, (b)70, (c)175, (d)190, and (e)205 τ_A. Red and blue indicate the toroidal direction of the flow.

types. The first one is fully confined particle, as is shown in Fig.3.20(a). The particles of this type rotate toroidally with smaller radius, which corresponds to the vicinity of the center of convection motion of linear instability modes, that is, near the $q = 1$ surface. The toroidal velocity is so large that the particles rotate toroidally several turns until $t = 250\tau_A$. For the second type, on the other hand, the particles rotate poloidally with large radius, as shown in Fig.3.20(b). The toroidal velocity is rather small for this type. The large poloidal rotation motion is related with the formation of the localized bulge. After the reconnection between the internal and the external magnetic field occurs, the particles are expelled continuously out of the torus. The third type is the most interesting one. This type is a compromise between the first and the second ones. The particles are confined in the beginning, rotating with smaller radius as those of the first type [see Fig.3.20(c)]. However, they are suddenly brought out of the torus through the localized deformation. The particles are carried in large velocity and almost straight, once they are switched into the path to be lost. This kind of motion implies that a channel for a convective loss of plasma actually opens.

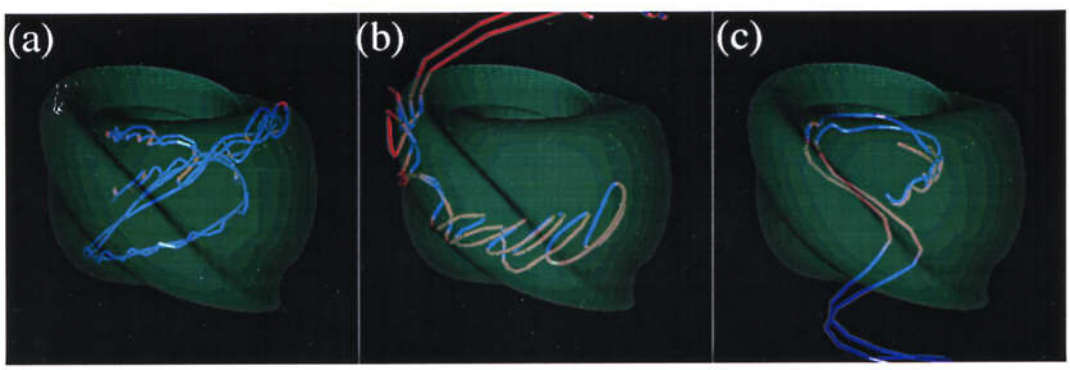

Figure 3.20: Typical streak lines of fluid particles. Three types are found. (a) Confined, (b) To be lost, forming a bulge, and (c) Forced to be lost by an opening of a loss channel induced by the magnetic reconnection between the internal and the external magnetic field. Red and blue indicate the toroidal direction of the flow.

The convective loss channel is definitely shown in Fig.3.21 by using the simulation result at $t = 195$. This is a similar picture to Fig.3.16 but is modified in several points to visualize the convective loss channel more clearly. In order to see the internal structure of plasma flow, a part of the iso-contour surface of pressure is cut away and one of the bunches of the flow, which goes upward in Fig.3.16, is removed. The poloidal pressure profile is drown on the right poloidal cross section with colored contour. Each of the flow vectors are also colored to indicate the local pressure in correspondent color with that used in the contour. The magnetic field near the bunch of the flow is almost parallel to the bunch. A typical field line is drawn on the figure with a thick dark-blue line. Figure 3.21 includes much fruitful information illuminating the convective loss process. Firstly, the bunch of the flow is formed continuously from the depth of the torus to the bottom wall. This can be a direct evidence of the existence of convective loss channel. It can be seen that there is a marvelous agreement between the bunch of the flow and the magnetic field

line, and that the pressure is definitely increasing as it rises up to the source region. These facts support our prediction that a strong flow is to be formed by the pressure imbalance along the reconnected magnetic field line. The velocity on the bunches of plasma flow reaches up to about $0.1v_A$ (v_A is the Alfvèn velocity normalized at the magnetic axis at $t = 0$).

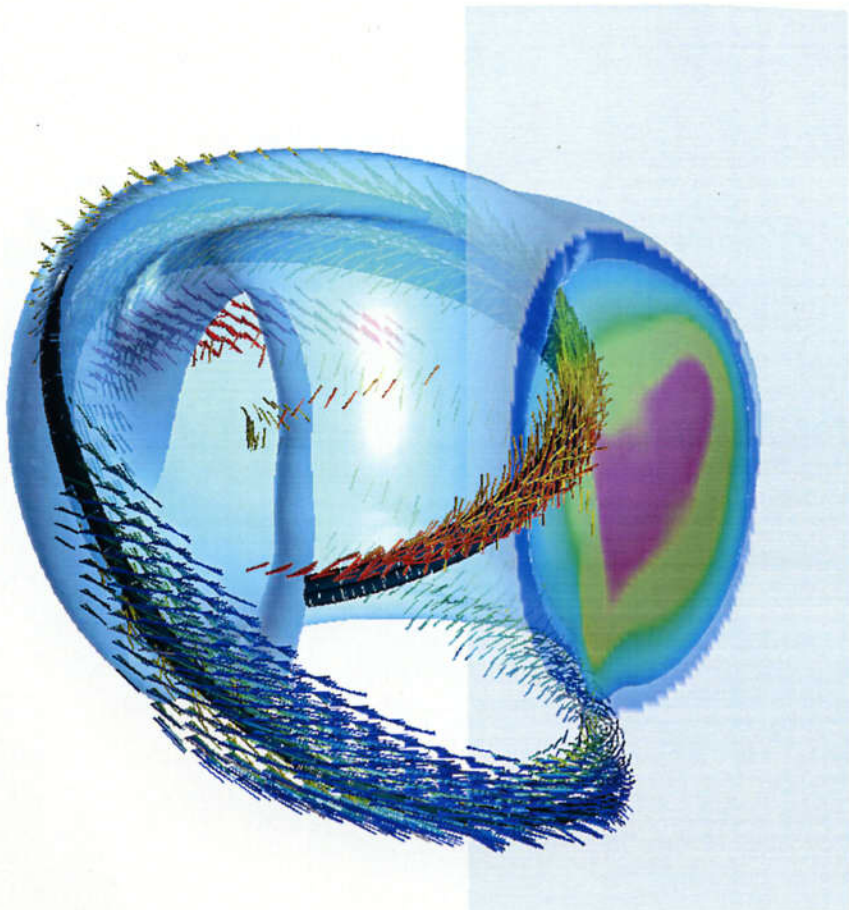

Figure 3.21: The internal structure of outward flow which is induced by the magnetic reconnection. Strong plasma flow (indicated by fine lines) arises from the deep inside of the torus along the reconnected field lines (indicated by thick lines). A pressure gradient is shown clearly by the color that corresponds to the local value of pressure.

The loss of heat energy caused by such mechanism based on a strong parallel flow is much rapid compared to any other cross-field transport process, and enhances the collapse of structure in the core region. However, it should be noted that the plasma flow never passes the right center of the torus, and the flow keeping its laminar structure for a long while. In other words, this type of energy loss is characterized by an effective expulsion of heat energy from the edge region of the torus. Consequently, as we can see from Fig.3.18(b), the configuration at the center region is not completely destroyed by this process.

3.4 Multi-step relaxation

3.4.1 Cessation and re-heating

The numerical calculation is sound enough to solve highly complicated nonlinear dynamics of plasma which is described in the previous sections. The simulation can be executed in only a single run from the beginning up to $t = 210\tau_A$. Namely, all of the key processes such as the linear growth of low-n interchange instability, the formation of the localized pressure bulge, the magnetic reconnection between the internal and the external magnetic field, and the generation of strong outward plasma flow, can be reproduced consistently in a single simulation run. However, after the plasma is expelled out of the separatrix, the plasma pressure extends quickly in several thin layers near the central rod, where the toroidal magnetic field is strong due to the large toroidicity. Therefore, the torus is vertically elongated, and the mass density is relatively decreased. It causes a local increase of Alfvèn velocity, and makes the execution of simulation run difficult. A slight difficulty can be overcome for instance by shortening the time interval of the integration. For all the effort, the execution get into fatal problem at around $t = 210\tau_A$. As a result, a fatal density and pressure hole is formed in the inner region, and the simulation is terminated. However, the overall structure actually remains at that time. Especially, the large scale behavior in the core region is still full of interest, partly because the convective loss channel does not penetrates the real core region of the torus, as described in the previous section. Therefore, it is meaningful to continue the simulation somehow. Such a pressure hole must be an artificial error, because a kind of restoring force and probably a kind of dissipation, which decelerate the expansion of the plasma, will work on the local hole of the pressure in the real system. The most straightforward way to overcome this difficulty is to increase the spatial resolution of numerical grid to solve the real forces more precisely. However, it seems to be a wasteful approach for our interest of the large scale behavior of plasma. Accordingly, we give up solving the fine structure in a simulation run. We try to continue the simulation by diminishing the short wave-length components artificially. Here, we apply a low pass filter on each variable to remove such insignificant fine structure. This treatment is not only for convenience of numerical calculation, but also for modeling of anomalous enhancement of dissipation for small-scale component due to the increase in the fluctuation of field quantities in a reasonable spatial resolution of numerical grid. The low pass filter used in the simulation is based on compensated binomial average in space[68]. This filtering is done by replacing each variable X_j with

$$\widetilde{X_j} = \frac{WX_{j-1} + X_j + WX_{j+1}}{1 + 2W}, \tag{3.8}$$

where W is the weighting factor for filtering. If $W \gg 1$, the scheme becomes a simple two-point average, which can strongly suppress the fine structure. However, it is not suitable for our present objective, because it smooths the large scale structure out beyond the permissible range. A binomial ($W = \frac{1}{2}$) filter compensated by $W = -\frac{1}{6}$ filtering gives one of the best solution for the present problem. The response of the filtering for the Fourier transformation of X with wavenumber k can be expressed by

$$\mathcal{F}\left[\widetilde{X_k}\right] = S(\theta)\mathcal{F}[X_k], \tag{3.9}$$

$$S(\theta) = \frac{1+2W\cos\theta}{1+2W}, \theta = k\Delta x. \tag{3.10}$$

Shown in Fig.3.22 is the trace of $S(\theta)$ for three kinds of low pass filter. It can be seen that the compensated binomial scheme can effectively diminish the large wavenumber component without spoiling the large scale behavior. We apply this filtering to all the variables when the gradient of at least one of the variables exceeds a certain level in somewhere in the simulation region. The filtering is applied at $t = 200 - 345\tau_A$ in advance of the appearance of irregular structure, though the problem does not become severe till $t = 210\tau_A$ without filtering. The results after $t = 200\tau_A$ which was described in the previous sections in this thesis is that with such artificial filtering.

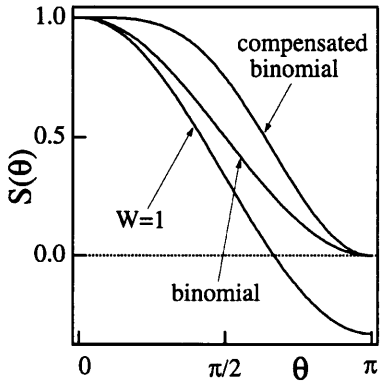

Figure 3.22: Response function for the low-pass filtering scheme.

Under such treatment, the simulation can be continued after the expulsion of plasma. Shown in Figs.3.23 and 3.24 are the sequels up to $t = 345\tau_A$ to Figs.3.18 and 3.17, respectively. It can be seen that the active deformation ceases after $t = 250\tau_A$, and an almost axisymmetric torus-shaped configuration appears again at $t = 345\tau_A$. Figure 3.25 shows the time development of the total kinetic energy of plasma. The total kinetic energy falls into about 5% of that at the most active stage of around $t \sim 200\tau_A$. The sequel to Fig.3.11 is shown in Fig.3.26. The central pressure falls more due to the expulsion of plasma till $t = 290\tau_A$. As the expulsion ceases and the torus appears again, the central pressure is increased again up to $t = 450\tau_A$ because of both the viscous and the Ohmic heating and the adiabatic compression.

With the appearance of the torus, the magnetic flux surface, which was once destroyed at the active stage, is reconstructed again, as shown in Fig.3.27 with a series of punctual plots of magnetic field lines. It can be seen that the magnetic flux surface disappears when the magnetic reconnection between the internal and the external magnetic field occurs at around $t = 200\tau_A$, and the punctual plot becomes chaotic from the edge to the core

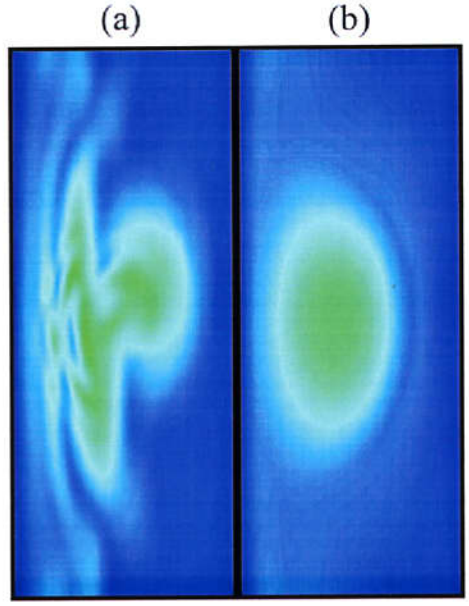

Figure 3.23: Sequel of Fig.3.18. Time equals to (a)290, and (b)345 τ_A.

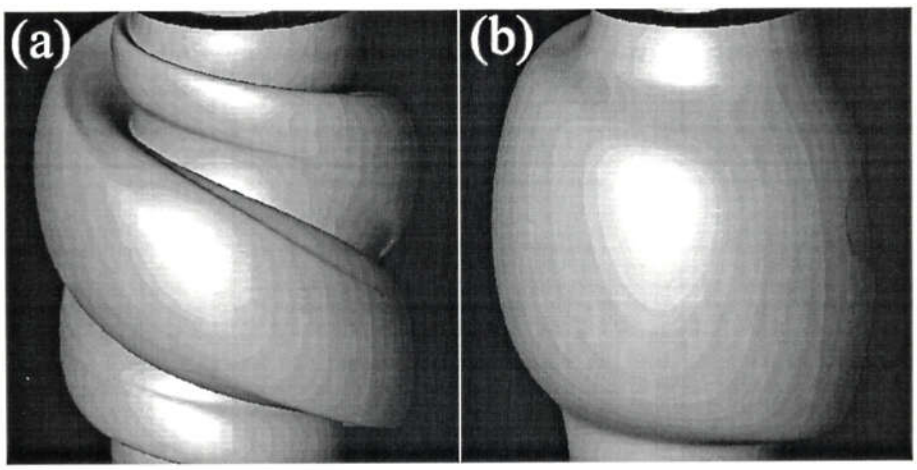

Figure 3.24: Sequel of Fig.3.17. Time equals to (a)290, and (b)345 τ_A. Only pressure is plotted.

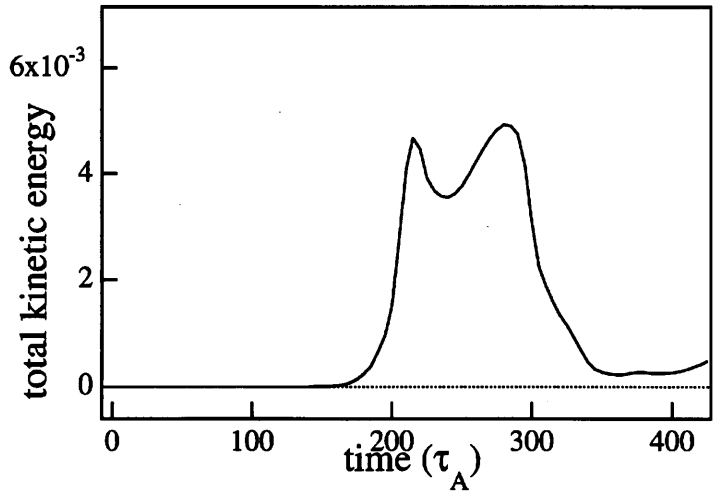

Figure 3.25: Time development of total kinetic energy.

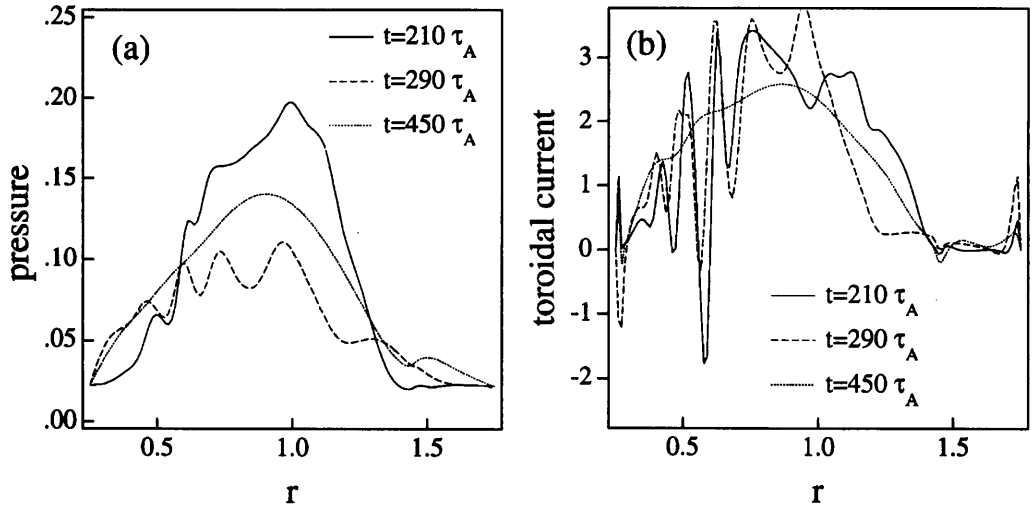

Figure 3.26: Sequel of Fig.3.11. Time equals to (a)210, (b)290, and (c)450 τ_A.

[see Figs.3.27(d)-(f)]. The mapping of field lines extends to the peripheral region near the center rod, corresponding to the appearance of characteristic conical shape, which is described in Sec.3.3.4. At $t = 290\tau_A$, the magnetic flux surface is completely destroyed [see Fig.3.27(f)]. At $t = 345\tau_A$ [see Fig.3.27(g)], however, magnetic flux surface appears again in the core region [see Fig.3.27(g)].

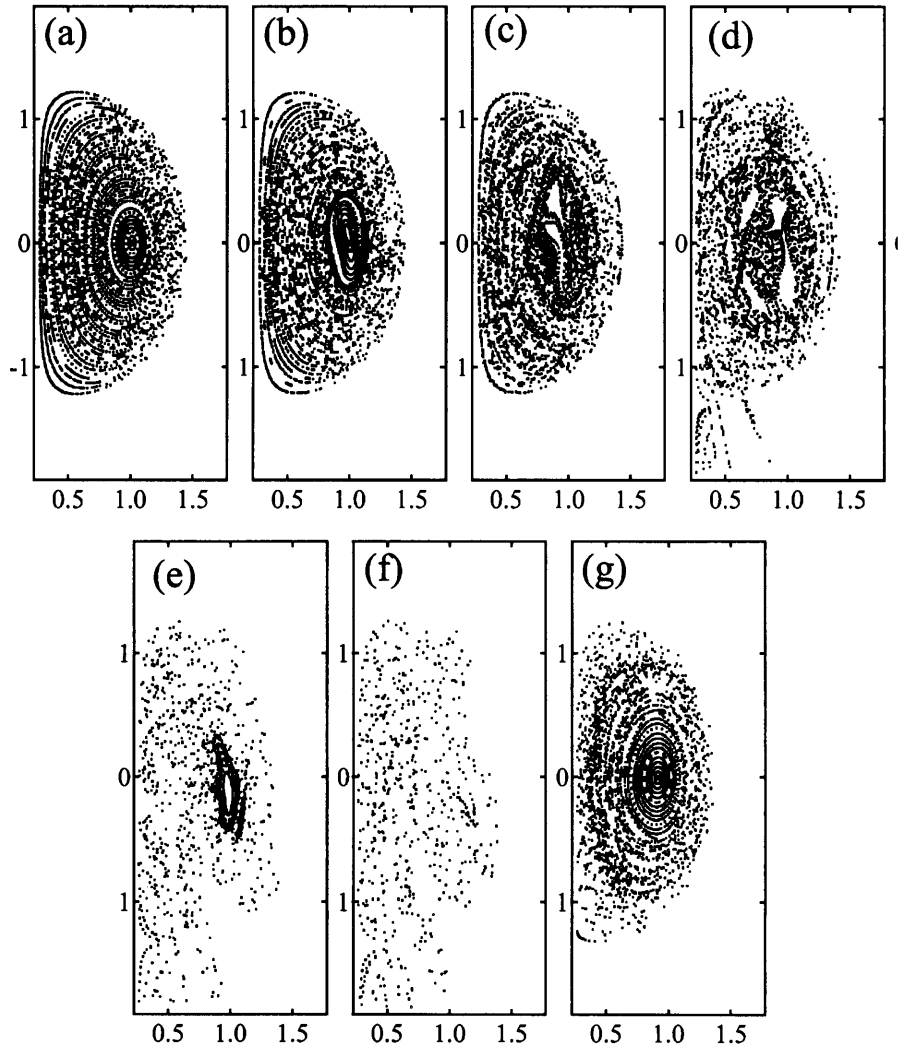

Figure 3.27: Punctual plots of field lines at time equal to (a)0, (b)165, (c)185, (d)200, (e)250, (f)290, and (g) 345 τ_A.

The comparison of the radial profiles between ones before and after the relaxation is shown in Fig.3.28. It can be seen that both the pressure [see Fig.3.28(a)] and the current [see Fig.3.28(b)] profiles are somewhat broaden after the relaxation. It should be also noted that the maximum pressure falls into about 50% compared to the initial value after the relaxation. On the other hand, the peak value of the toroidal current is not changed almost at all. It means that the intensity of poloidal magnetic field does not change so

much. Shown in Fig.3.28(c) is the change in the radial safety factor (q) profile. In general, it is difficult to measure the q-value of asymmetric configuration, even the definition of q-value is obscure. However, in this case at $t = 345\tau_A$, there is a clear magnetic flux surface structure, so that at least a rough estimation for q-value is available by tracing the magnetic field lines. The safety factor is estimated as the separation in toroidal angle while the field line trace goes round once in the poloidal direction. The broken line on Fig.3.28(c) is obtained in such way. (Therefore, it cannot be calculated with sufficient accuracy near the magnetic axis.) It should be noted that the central safety factor rises up to about 1.2 after the relaxation. Even if we take account of the lack of accuracy near the magnetic axis, it is undoubted that the central q-value exceeds unity after the relaxation. Namely, the $q = 1$ surface diminishes at that time. This change is explained by the reduction of the Shafranov shift due to the decrease in the β value. Namely, the toroidal magnetic field at inner region is larger because of the effect of toroidicity, on the other hand, the poloidal field is not so changed by the relaxation as described above. This will cause an increase of the safety factor.

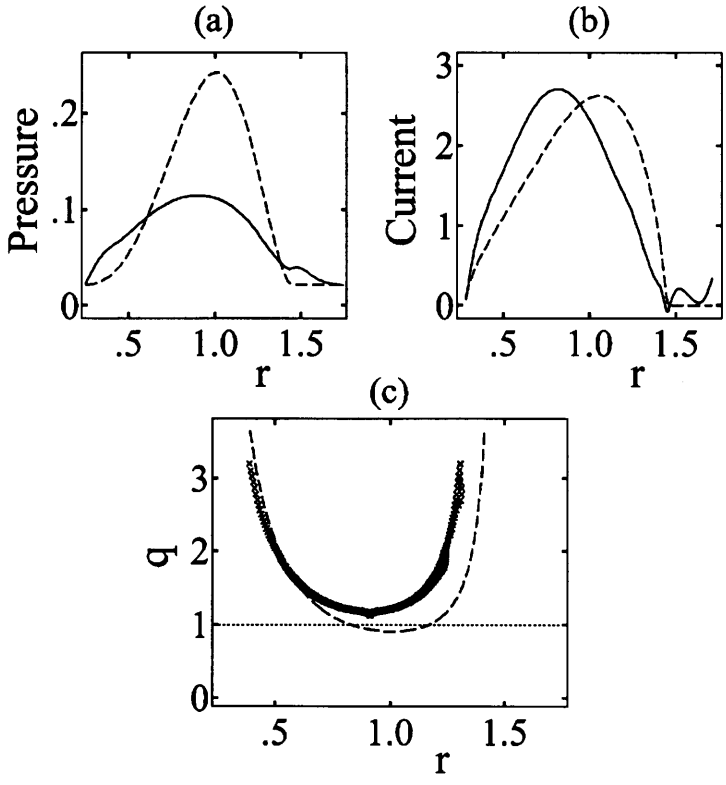

Figure 3.28: Change in radial profiles of (a)pressure, (b)current, and (c)safety factor on the midplane. The broken line and the solid line [the cross markers in (c)] correspond to $t = 0$ and $t = 340\tau_A$, respectively.

The system is ideally stabilized in this state for the modes which are linearly unstable in the initial equilibrium, partly because of the change in the profile of the torus, especially

the change in the safety factor profile as is stated above, and partly because of the decrease in the β value due to the expulsion of the heat energy.

3.4.2 Behavior of resistive instability

The model of the anomalous enhancement of dissipation due to the activation of short-wavelength fluctuations, which is introduced in the previous subsection, is an inconsistent assumption in a sense until the increase of other dissipation terms such as resistivity and viscosity is included. In particular, the increase in the resistivity can destabilize the system with some resistive modes. We should take account of the effect of resistivity due to the existence of the fluctuation and the decrease of the temperature.

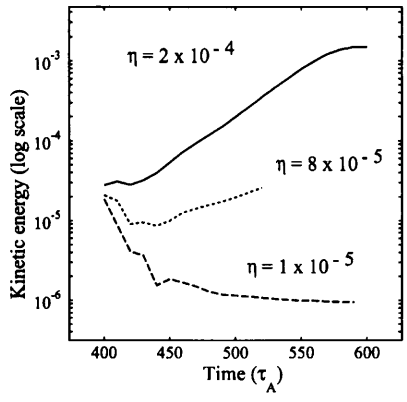

Figure 3.29: Time development of total kinetic energy for the second stage. The result of calculations with three different values for the resistivity term, are plotted.

Shown in Fig.3.29 is the time development of the total kinetic energy for three cases, where the viscosity $\mu = 4 \times 10^{-3}$ and the resistivity η equals to 1×10^{-5}, 8×10^{-5}, and 2×10^{-4}. It can be seen that the kinetic energy grows for larger resistivity, and is damped for smaller resistivity. It means that the system is unstable for resistive modes, though it is stable for ideal modes.

The same plot as Fig.3.2, that is, the time development of the total magnetic energy for each toroidal Fourier mode at this stage is shown in Fig.3.30 for the $\eta = 2 \times 10^{-4}$ case. A dominant growth in $n = 1$ mode can be seen. To make sure the mode structure for the resistive mode, the three-dimensional and poloidal mode structure at $t = 410\tau_A$ are visualized in Fig.3.31 and Fig.3.32, corresponding to Fig.3.5 and Fig.3.4, respectively. The $n \neq 0$ component is shown in each figure. It can be seen that the $n \neq 0$ perturbation is composed by almost only $n = 1$ mode. And it should be noted that the $n = 1$ mode has another helicity than that of the linear $m = 1/n = 1$ mode. This can be easily recognized by comparing Fig.3.31 with Fig.3.5(a), where the toroidal pitch of the resistive mode is larger than that of the $m = 1/n = 1$ mode. Fig.3.32 shows that the $m = 2$ component is included as the most dominant poloidal component in the $n = 1$ mode, and the $m = 3$

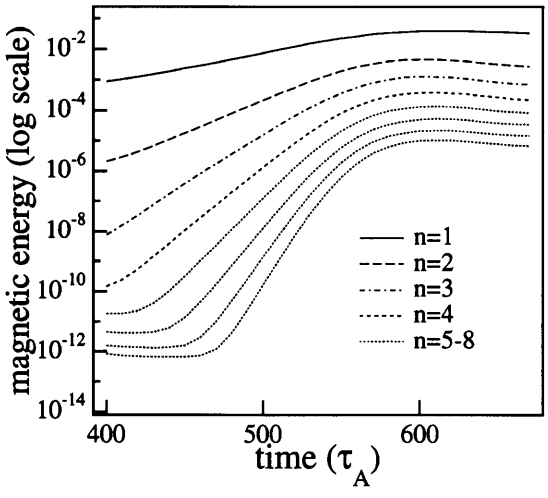

Figure 3.30: Same as Fig.3.2 but for the second growth with $\eta = 2 \times 10^{-4}$.

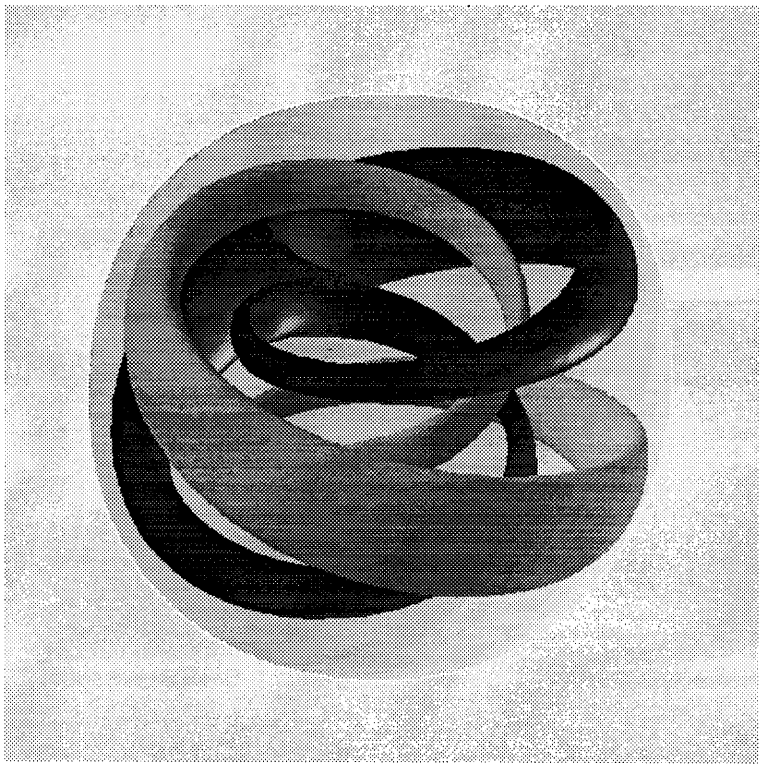

Figure 3.31: Three-dimensional structure of the eigenmode of the second stage. The $n \neq 0$ component at $t = 410\tau_A$ is plotted.

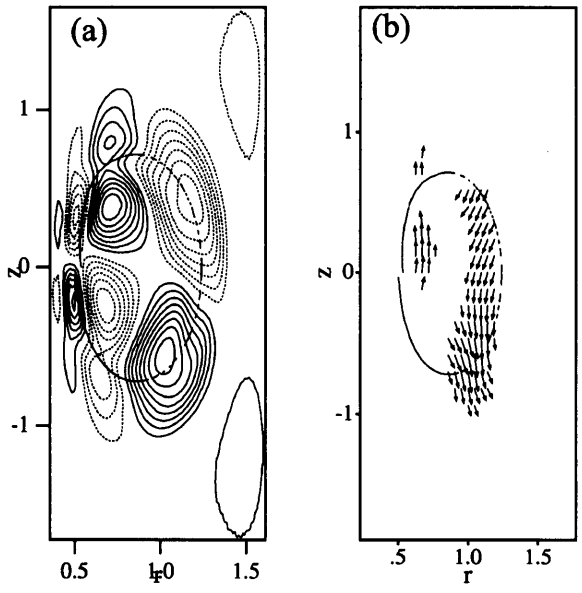

Figure 3.32: Same as Fig.3.4 but for the second stage. The $n \neq 0$ component at $t = 410\tau_A$ is plotted.

component exists in the outer region with smaller amplitude. In Fig.3.32, the location of the $q = 2$ rational surface is specified with a dashed line. This is a rough trace of magnetic field line which has a helicity of $q = 2$, namely, which comes back to the initial point of the trace after passing around the torus twice in toroidal direction and once in poloidal direction. The field line tracing is done at the most silent stage at $t = 345\tau_A$. It can be seen that the $m = 2/n = 1$ component is resonant to the $q = 2$ rational surface. Such a resonance to the rational flux surface is a general nature of a resistive mode. The tiny discrepancy in the inner region may be due to the error on the field line trace and the difference of the relevant time between that when the field line is traced and that when mode structures are estimated.

Further time development of this $m = 2/n = 1$ resistive mode gives a large deformation of the overall shape again. Figure 3.33 shows the overall shape of the torus at $t = 500\tau_A$ with an iso-contour surface of pressure cut in half at two poloidal cross sections. The only difference between Figs.3.33(a) and (b) is the toroidal angle of the view, which is perpendicular to each other. The $m = 2$ displacement corresponds to an elliptical elongation in a poloidal cross section, and the direction of the elongation varies in toroidal direction with the toroidal mode number. In this case, the direction of poloidal elongation becomes just perpendicular in the toroidally opposite side. Therefore, if the elliptical elongation appears vertically in a poloidal cross section, the opposite side is elongated horizontally as is shown in Fig.3.33(a). Namely, the deformation becomes fully asymmetric. On the other hand, if a poloidal cross section is elongated obliquely in about $\frac{\pi}{4}$, the opposite side is elongated just parallel to it, but in the opposite direction. That is, the overall shape looks tilted, as is shown in Fig.3.33(b). Such large axis-asymmetric deformation is the characteristic feature of this instability.

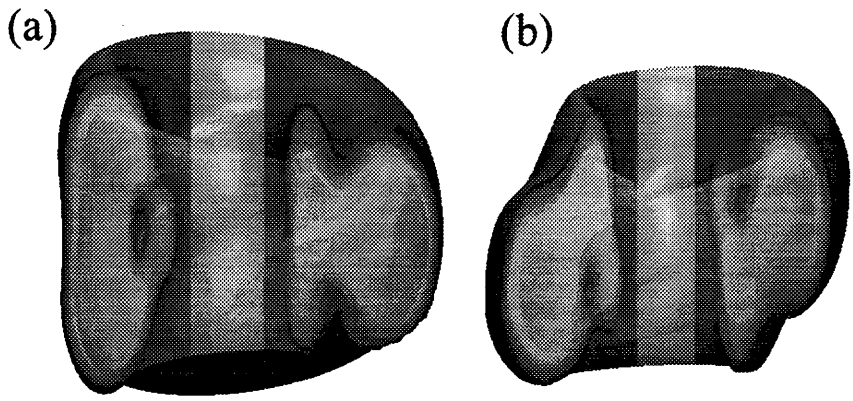

Figure 3.33: Time development in pressure profile in the second stage.

Furthermore, the ultimate of the growth of this instability is a vague spread of the plasma into whole the simulation region, namely, a full destruction of the configuration. Thus, it can be said that the resistive stage is destructive or dangerous compared to the ideal stage described in Sec.3.3.

Chapter 4

Discussion

4.1 Comparison with experiments

In this section, we compare the simulation results with the experimental observations of IREs. As described in Sec.1.2.2, the characteristic features of IRE is summarized as follows:

- a rapid collapse of the density and the temperature profile
- low-n activities precursory of the thermal quench
- a large deformation of the overall shape
- a rapid increase in the net toroidal current just posterior to the thermal quench
- a strong resilience in both the plasma pressure and the toroidal current

We have executed a simulation for the case where the low-n modes grow dominantly on their linear growth as described in Chap.3. In the weakly nonlinear stage, the perturbation of the instability becomes a visible scale. The structure of the perturbation retains the low-n natures, especially, a large pressure bulge is formed as a superposition of several modes. The amplitude of such activities is so large that they would be observed also in real experiments as some low-n activities.

4.1.1 Time development of observable quantities

Let us consider in more detail about the comparison with experimental observations. Figure 4.1 shows a comparison in the temporal change in the radial pressure profile. Shown in Fig.4.1(a) is the simulation result of the time development of the radial pressure profile on the midplane in a fixed poloidal cross section. The result of the resistive stage for $\eta = 2 \times 10^{-4}$ is plotted continuously together in Fig.4.1. It can be seen from Fig.4.1(a) that the pressure profile suddenly collapses at around $t = 200\tau_A$, while there is no visible change in the prior time development. Furthermore, the pressure profile is broadened while it falls rapidly ($t = 200 - 300\tau_A$), since the pressure falls mainly in the central region and the pressure is transported to the edge region by the convection motion. The

increase of the pressure at the outside of the separatrix can be seen in Fig.4.1(a) because of the expulsion through the magnetic reconnection, as described in Sec.3.3. The central pressure can be seen to recover to some level after the rapid fall ($t = 300 - 480\tau_A$).

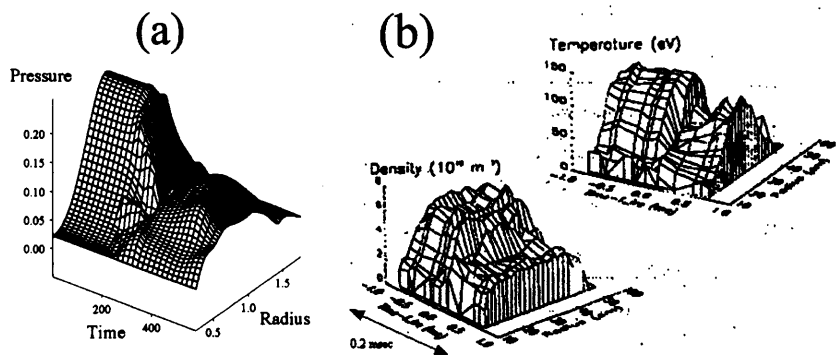

Figure 4.1: Comparison between (a)simulation and (b)experiment in the temporal change in the radial (a) pressure and (b) density and temperature profiles. [(b): reprint from Fig.10 of Ref.[16].]

Such features in Fig.4.1(a) are in good agreement with experimental observation that is reported in Ref.[16]. Shown in Fig.4.1(b) is the reprint from Fig.10 of Ref.[16], in which the temporal change in the radial profiles of the electron density and the electron temperature measured in START by using Thomson Scattering is plotted. The plasma pressure in the MHD simulation is expressed by the sum of the ion and the electron pressure that is modeled as a product of the density and the temperature. Therefore, the behavior of the pressure in the MHD simulation can be compared roughly with these experimental observations. The rapid fall in the central pressure, the broadening of the radial profiles, and the immediate reheating after the collapsing phase in the central region are in good agreement between the simulation and the experiment.

As for the time scale of the process, the temporal resolution is not sufficient with above observations, in which the electron temperature falls in one or two steps of the plots. Thus, we compare it using another experimental observation. Figure 4.2 shows the comparison in the time development of the observable quantities. Shown in Fig.4.2(a) is the simulation result of the maximum value in the pressure of all over the simulation region. It can be seen that the maximum pressure decreases in a short time scale of around $100\tau_A$. According to the normalization for START operating parameter that is described in Sec.2.2.2, the time scale of $100\tau_A$ corresponds to about 50μsec with START operation parameter. This is comparable to the experimental observation in START as shown in Fig.4.2(b). Shown in Fig.4.2(c) is the experimental result of a soft X-ray (SXR) measurements at $R = 34.6$ cm[9]. The SXR signal includes the information of electron temperature in the core region. Therefore, it can be compared with the simulation results in Fig.4.2(a). It can be seen from Fig.4.2(c) that the SXR signal falls in about 150μsec. This time scale is in accordance with the simulation result by factor 3. It is a fairly good agreement.

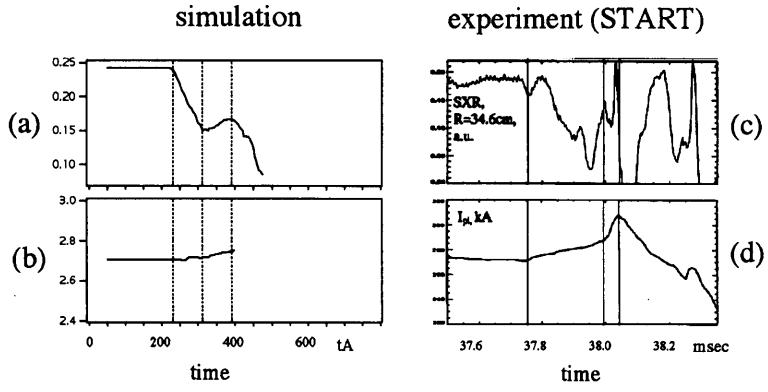

Figure 4.2: Comparison with experiments in the time scale of the process. (a) Maximum pressure in the simulation result. (b) Net toroidal current in the simulation result. (c) Experimental data of SXR measurement. (d) Experimental observation of plasma current.

As described in Sec.1.2.2, the thermal quench in an IRE usually proceeds in two step: the first slow phase and the second fast phase. It really agrees with our simulation results. The central pressure falls for the first step by the convection motion of the instability. Namely, both the shifting motion of the bulk plasma and the rapid loss of plasma due to the magnetic reconnection cause a decrease of the pressure in the core region. And when we consider the second step of the simulation that is described in Sec.3.4, the decrease of the pressure occurs in two steps. It is in good agreement with experiments, in which the thermal quench usually occur in two-step, as described in Chap.2.

Thus, now it can be concluded that the rapid fall in the density and the temperature profiles observed in the experiment is explained by the nonlinear development of low-n interchange instability

As for the rapid increase in the net toroidal current which is observed in the experiments, a direct comparison between the simulation and the experiment is not available, because the simulation cannot be continued to the stage in which the current increases. As is shown in Fig.4.2(d), the net toroidal current increases just after the thermal quench phase in the experiment. The change in the current is not so large during the SXR drop. Since the simulation result mainly corresponds to the SXR drop, the remarkable change in the net toroidal current is not observed in the simulation as shown in Fig.4.2(c). However, it should be noted that the net toroidal current does not change so much in good agreement with the experiments, in spite of the violent perturbation in its profile during the thermal quench as shown in Fig.3.11(b). .

4.1.2 Deformation of the overall shape

In this subsection, we focus on the change in the overall shape of the torus. The simulation result shows some characteristic global deformation of the torus, such as an appearance of the toroidally localized bulge of the plasma pressure on the outermost surface, an appearance of the characteristic conical shape at the top and the bottom of the torus

after the magnetic reconnection between the internal and the external field occurs, and some axis-asymmetric deformation due to the development of the resistive $m = 2/n = 1$ mode instability. These observation can be compared with the numbers of experimental result of the measurement in START using a charge coupled device (CCD) camera[9]. Shown in Fig.4.3 are the typical snapshots taken by the CCD cameras in the START experiment[9]. Figure 4.3(a) is the images of START plasma taken at a stable state[9]. The picture is taken by a wide-angle lens, so that the whole of the center rod and the peripheral constructions are taken on the image. The plasma looks almost axisymmetric spherical shape. It should be noted that the brighter region corresponds to the lower temperature region on the images. Therefore, the plasma appears on the images as a thin red shell at low temperature region.

Figures 4.3(b)-(g) are the snapshots of START plasma which are taken at the moment when an IRE occurs. Only Fig. 4.3(b) is taken by a monochromatic CCD camera which has a higher time resolution of about 30μsec, and the other pictures are taken by a color CCD camera which has a relatively poor time resolution of about 100μsec. It can be seen in Fig.4.3(b) that there is a bright helical structure which extends on the surface of the torus from the top to the bottom, surrounding behind the center rod. It should be noted that the bright region is localized in only a narrow region. According to Ref.[9], similar structure is often observed in START when IRE occurs. Shown in Fig.4.4 is a series of snapshots taken by the same CCD camera at every 222μsec while an IRE occurs. It can be seen that the helical structure appears only in the beginning of the IRE at $t = 44.000$msec [see Fig.4.4(b)]. This structure agrees with the localized pressure bulge that appears at around $t = 200\tau_A$ in the simulation result. In the simulation, such a localized pressure bulge appears only in a narrow region on the surface of the plasma, and it keeps the structure for only several tens of τ_A in the beginning of the nonlinear stage. Therefore, it can be said that the bright helical structure in Fig.4.3(b) and the localized deformation in the simulation result are in good agreement both in the temporal and the spatial scale.

In the color images shown in Figs.4.3(c) and (d), the overall shape of the torus is largely deformed. The bright region can be seen to extend to the top and the bottom boundaries of the chamber along the center rod. It can be seen that the bright region expands wider at the top and the bottom than at the center, so that the bright region looks like a pair of cones. Especially, it can be clearly seen in Fig.4.3(c) that the cones consist of several thin layers. These structures seem to correspond to the characteristic conical structure which appears in our simulation result after the magnetic reconnection between the internal and the external magnetic field occurs. Since the time resolution of the color CCD camera is relatively poor ($\sim 100\mu$sec), instantaneous structures may be smoothed out or accumulated in time on the images. As for this structure in the simulation result, the expelled plasma extends along the stiff external magnetic field, so that it holds the characteristic conical structure for a pretty long duration of around $150\tau_A$ since $t = 200\tau_A$ under an assumption that there is not any cooling mechanism on the boundary walls. Thus, it is reasonable that the conical structure can be captured on the color CCD camera images in spite of its poorer time resolution. Furthermore, some spiral bright part can be seen in the middle of Figs.4.3 (c) and (d). In Fig.4.3(d), it clusters slightly below the center of the torus. Such structures are also observed in the

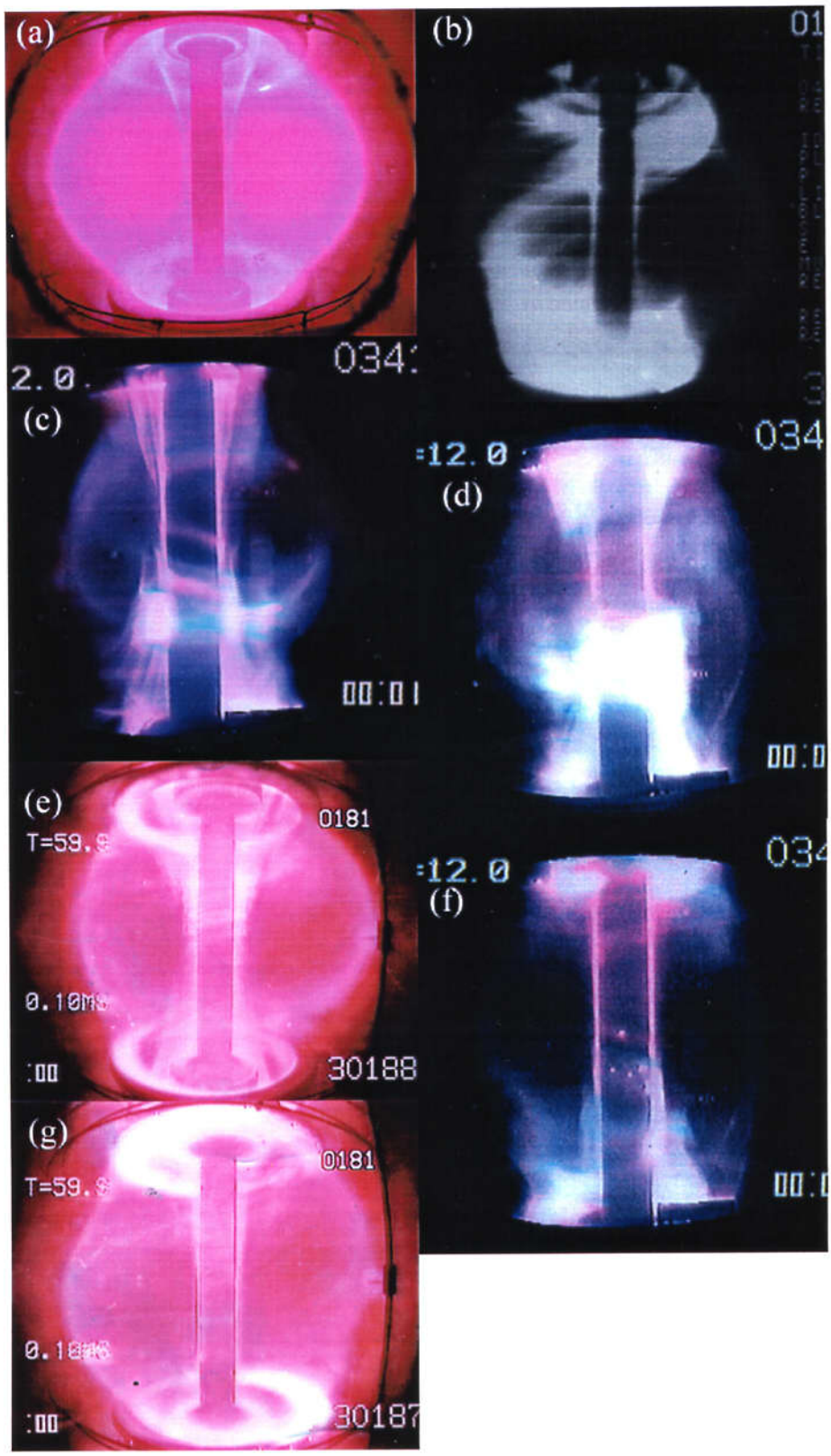

Figure 4.3: Images taken by CCD camera in START experiment by courtesy of Dr. A. Sykes and Dr. M. Gryaznevich.

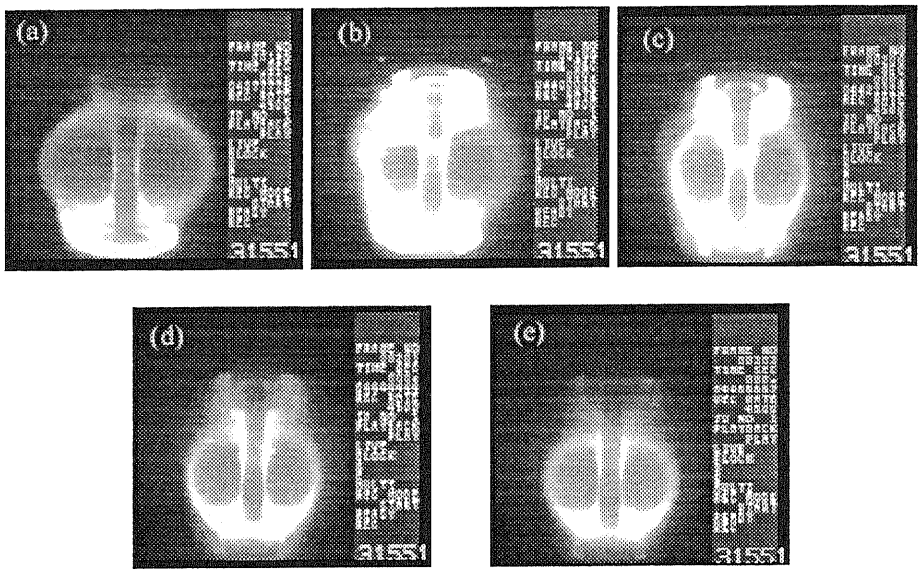

Figure 4.4: Sequencial images taken by a high time-resolution CCD camera.

simulation result. Namely, as a part of the plasma is expelled out of the torus through the magnetic reconnection, the core plasma gradually shrinks to some extent. Although the most noticeable deformation is the single localized bulge, the activity of the most dominant $n = 2$ modes still remains in the core plasma at that time, and it appears out when the plasma shrinks. Namely, similar helical structure is formed in the opposite side of the torus, so that the overall shape of the core plasma is deformed into a complicated helical structure like Fig.3.24. However, an iso-surface plot is inconvenient to be compared with the experimental observations of CCD camera images, because the surface screens out the opposite side of the torus by itself, and because it has only the information of the plasma exactly at the threshold level. A possible solution for this problem is to make use of the so-called volume rendering technique, which is represented by a line integral of the stimulation from the plasma to the view point. Shown in Fig.4.5 are those representations. The stimulation from the plasma is assumed to be much for colder plasma than for hotter plasma, so that the brighter region on the image roughly corresponds to the region where it is denser with low temperature plasma. The view point is set to be at the far infinite. Though the physical meaning of this representation is not so clear, it is useful to derive the global structure of the plasma, which can be compared with the CCD camera images.

Figure 4.5(a) is thus created with the simulation data at $t = 250\tau_A$. The characteristic conical shape at the top and the bottom is clearly shown in the figure. Besides, some bright parts can be seen in spiral shape at the middle of the image. Thus, there are fairly good agreement between Figs.4.3(c)-(d) and Fig.4.5(a).

Figures 4.3(e)-(g) are taken by the color CCD camera at slightly later stage of IREs for different shots. These images can be considered to capture the same phenomenon viewed from different angles perpendicular to each other. It can be seen in Figs.4.3(e) and (f) that the shape of the poloidal cross section on both side is different each other, namely, the

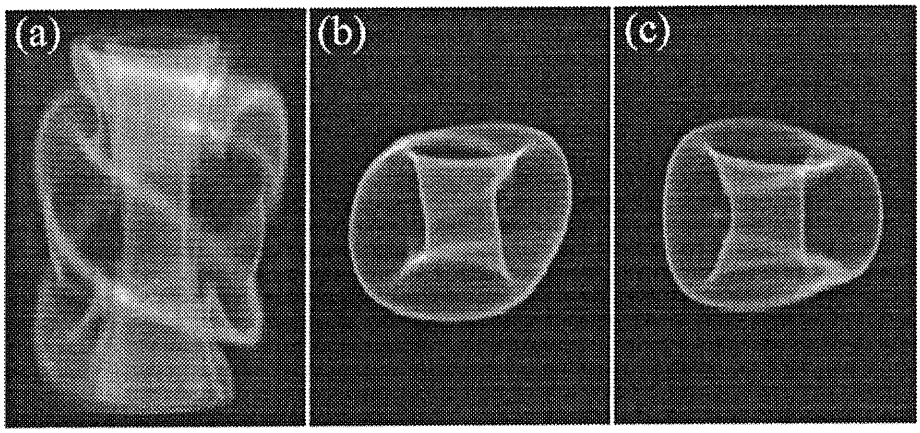

Figure 4.5: Simulation result corresponding to CCD camera images drawn by volume rendering scheme. (a) $t = 250\tau_A$, (b),(c) $t = 470\tau_A$. The difference between (b) and (c) is the view angle.

torus suffers an axis-asymmetrical deformation. In Fig.4.3(e), the poloidal cross section on the right hand side of the image is fatter (more horizontally elongated) than that on the left hand side. On the other hand, in Fig.4.3(f), the right poloidal cross section is thinner (vertically elongated) than the left one. These horizontal and vertical elongations are considered to show the existence of the $m = 2/n = 1$ mode activity. Namely, the asymmetric deformation captured in Fig.4.3(e) corresponds to those shown in Fig.3.33(a). They are in good agreement in the structure. And Fig.4.3(f) can be considered to capture the same deformation just from the opposite direction. On the other hand, Fig.4.3(g) shows a largely tilting deformation, which agrees well with the deformation shown in Fig.3.33(b). Therefore, this image is considered to capture the same phenomenon viewed from the direction perpendicular to that of Figs.4.3(e) and (f). Figures 4.5(b) and (c) are the same plot as (a) but for the data at $t = 470\tau_A$. They are in good agreement with Figs.4.3(e)-(g).

Thus, there are several pieces of excellent agreement in the observations of overall shape of the plasma between the simulation and the experiment.

4.2 Dependency on parameters

The linear instability described in Sec.3.2 is quite sensitive to the profiles of the initial equilibria. Especially the existence of the $q = 1$ surface causes the growth of the low n modes resonant to it such as $m = 1/n = 1$ and $m = 2/n = 2$. Here we examine the effect of the $q = 1$ rational surface on the nonlinear development. We have executed another simulation run, which we call hereafter case B, starting from an equilibrium where $q_0 = 1.06$, and other parameters are almost the same as those described in Sec.3, which is called case A.

The linear instability for case B is dominated by higher n modes than case A, such

as $m = 12/n = 8$. These modes are identified as the ballooning modes by following the same procedure as described in Sec.3.2. The figures corresponding to Fig. 3.3 and Fig. 3.4 for case B are shown in Fig. 4.6 and Fig.4.7, respectively. It can be seen in Fig. 4.6 that the peak of the growth rate for each mode appears at $n = 8$. It is noted that the higher n modes than $n = 8$ mode are well damped, so that the numerical validity is ensured also for this case. As seen in Fig. 4.7, the poloidal mode structure for $n = 8$ mode shows a poloidally localized activities in the bad curvature region. The growth rate of those unstable modes for case B, on the other hand, is much smaller than that of the dominant modes for case A.

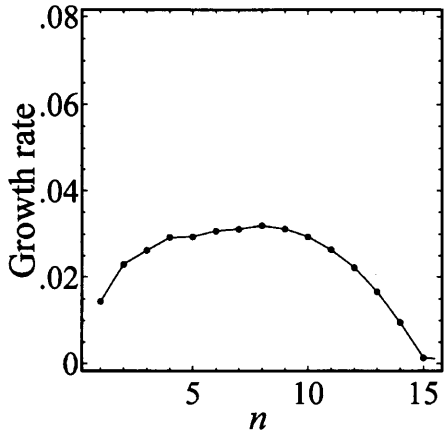

Figure 4.6: Same as Fig.3.3 but for case B.

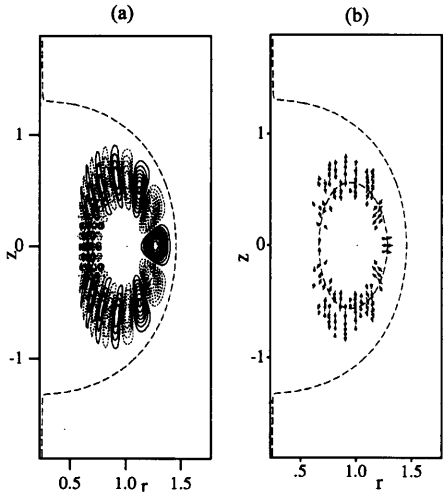

Figure 4.7: Same as Fig.3.4 but for $n = 8$ mode in case B.

It is worthy of notice that the nonlinear development for case B shows a quite similar

behavior to that for case A. Namely, the localized deformation also appears in case B in the early nonlinear stage. In case B, however, the localized deformation consists of several small bulges, not a single one, as shown in Fig. 4.8. The occurrence of the alignment of the phases among the toroidal modes which is described in Sec.3.3 is difficult to be recognized clearly in case B because of the small discrepancy in phases among the modes due to the high-n nature.

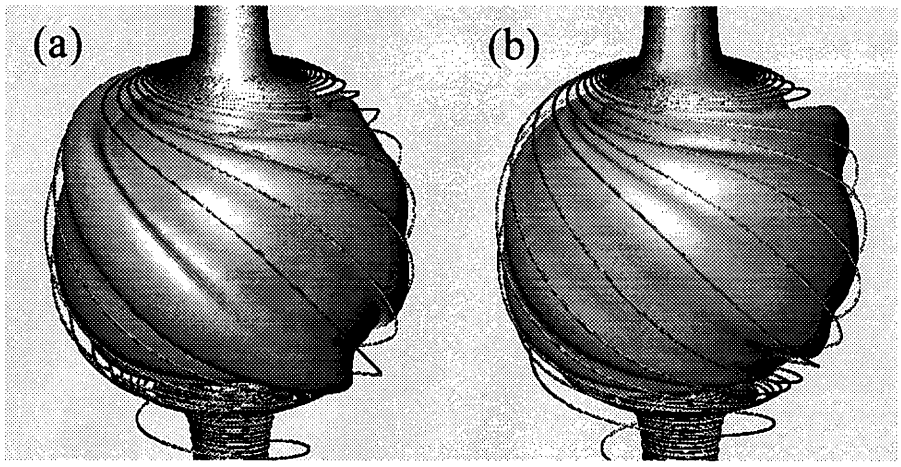

Figure 4.8: Same as Fig.3.12 but for case B.

The development after that resembles to that for case A. Namely, the magnetic reconnection between the internal and the external field occurs at a couple of large bulges, and the characteristic conical shape also appears at the top and the bottom of the torus as shown in Fig. 4.9. After expelling part of plasma pressure out of the separatrix, the system becomes ideally stable. The instability for the resistive modes is similar to case A, that is, the $m = 2/n = 1$ distortion grows when we put a larger resistivity.

Hence, it is concluded that there is no significant difference in the nonlinear development between the cases A and B, except for the number of localized deformation. That is to say, an IRE can occur under such condition where q_0 is greater than unity.

4.3 Spontaneous phase alignment among modes

The appearance of the localized pressure bulge described in Sec.3.3 is one of key mechanisms of this phenomenon in that it causes the collapse in pressure profile and the expulsion of the heat energy through the magnetic reconnection which is induced on it. It is the alignment of the phase among toroidal modes that directly causes the occurrence of the localized deformation[69]. Though the toroidal phases of $n = 2$ and the $n = 1$ modes are almost aligned each other in the simulation results described in Sec.3.3, there really be an arbitrariness in toroidal phases in there linear growth, because the system is fully axisymmetric. The toroidal phase must be determined only by the initial tiny perturbation. Therefore, it is necessary for us to check the dependency for initial perturbation

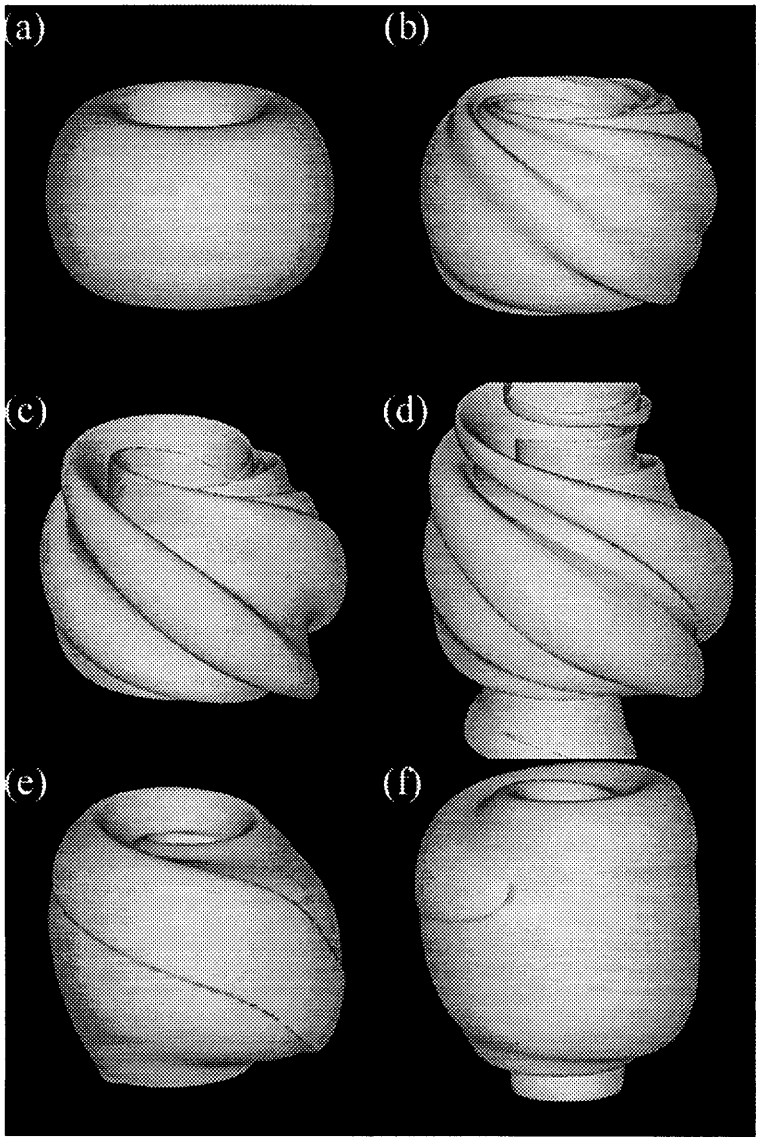

Figure 4.9: Same as Figs.3.17 and 3.24 but for case B.

patterns in order to make sure the scenario described above. Especially, we consider in this section whether the localized deformation appears or not when the toroidal phases are not aligned among the dominant modes in the linear stage.

To begin with, we execute another simulation run to check the role of the $n = 1$ mode in the nonlinear stage. This run is realized by artificially suppressing the growth of the $n = 1$ mode. The suppression is realized by setting the amplitude of the initial perturbation of the $n = 1$ mode much smaller than the $n = 2$ mode. Figure 4.10(a) shows the result for this case with an iso-contour plot of the pressure at the moment the bulge-like deformation appears. It can be seen that two bulges originated from the $n = 2$ mode are formed. It proves the necessity of the accompanying $n = 1$ mode for the production of the single localized deformation. Besides, in this case, the $n = 1$ mode also grows with the same growth rate as case A in the beginning of the linear stage, as shown in Fig.4.10(b). However, the growth reaches much lower saturation level than case A, because of the change in the global configuration caused by the growth of the $n = 2$ mode.

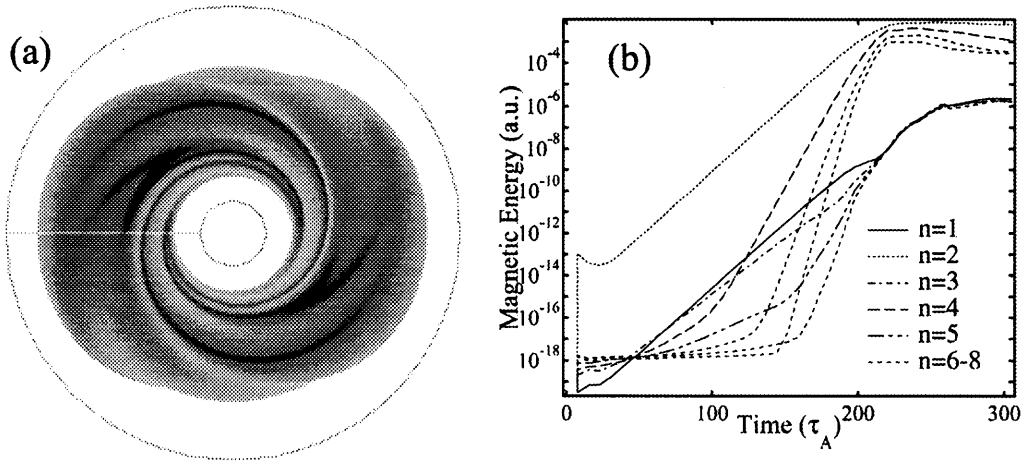

Figure 4.10: (a) Simultaneous appearance of two localized deformations in the simulation result where the $n = 1$ activities are artificially. suppressed. (b) Same as Fig.3.2 but for this case.

The phase-alignment mechanism among the excited modes, as is observed in Fig. 3.13, is an universal nature in the development of this phenomenon. Namely, the phases are spontaneously aligned to particular modes as a result of nonlinear interaction among them. In order to confirm the nature of the spontaneous phase alignment, we execute a simulation, in which the toroidal phase of the $n = 1$ mode is initially shifted from that of $n = 2$. Figure 4.11 is a top view of the torus and shows the time development of the fluctuations in the pressure on the midplane for $n = 1$ and $n = 2$. It is observed that the $n = 2$ mode never changes the direction, while the $n = 1$ mode is eventually split in two[Fig.4.11(d)], and the outer one spontaneously rotates till it is aligned to the $n = 2$ mode [Figs.4.11(g) and (j)].

Thus, it is proved that the localized deformation always appears in spite of the initial

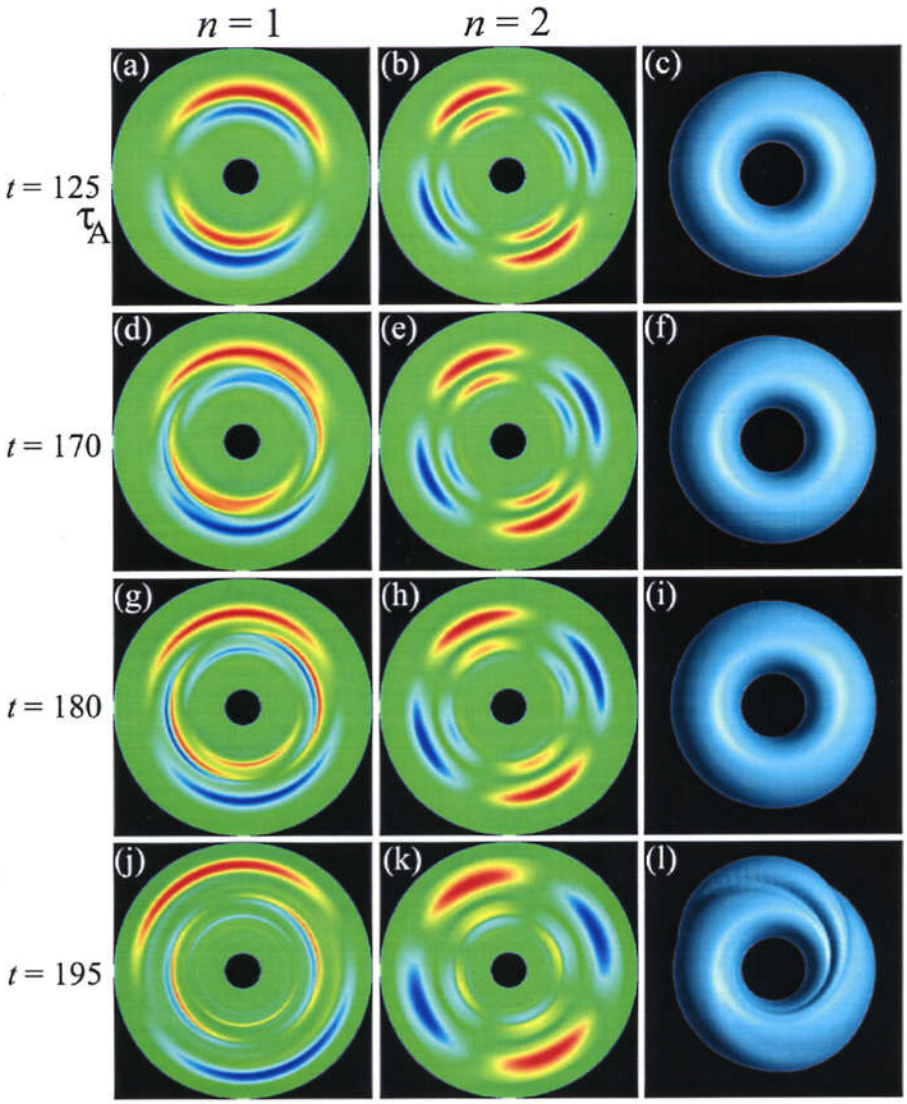

Figure 4.11: Spontaneous phase alignment between $n = 1$ and $n = 2$ modes. The temporal change in the fluctuation in pressure on the midplane for the $n = 1$ (left panels) and the $n = 2$ (center panels) are drawn by colored shades. Corresponding change in overall shape is drawn in right panels by the top view of an iso-contour surface of the net pressure. The $n = 1$ component gradually rotates until it is aligned with $n = 2$ mode. The localized deformation appears at the top in the panel.

discrepancy among the phases.

4.4 On the parallel heat transport

As described in previous parts of this thesis, a key mechanism of this phenomenon is the strong plasma pressure flow streaming from the core region to the outside of the separatrix. The plasma flow is induced by a pressure imbalance along the reconnected magnetic field line that links the core and the peripheral region. Therefore, the plasma flow is governed mainly by the physics parallel to the magnetic field. In this simulation, it is the pressure gradient that causes the appearance of the plasma flow. However, the physics parallel to the magnetic field will be more complicated in real plasma due to numbers of transport mechanisms such as the rapid electron heat conduction. The simple MHD model that we use in this simulation does not carefully take account of such effect of the transport. The pressure is defined by a simple product of density and temperature. The dynamics along the magnetic field is determined only by the force due to the pressure gradient. The individual behavior for each electron and ion fluid cannot be separated by this model. It is one of the limitations of the MHD closure at present situation that the detail of such effect cannot be taken account in a self-consistent manner. However, it is necessary for us to estimate the effect of such transport phenomenon on the simulation result when we compare it with experimental observations. To examine the effect of such transport phenomenon by simulation with some modified model is a difficult problem, because the electron heat transport is so rapid that the equations become highly stiff. Here, let us consider it inductively from the simulation result.

The electron-electron collision time(τ_{ee}) is about 1.6μsec ($3.3\tau_A$) for the typical experimental plasma in START ($n \sim 4 \times 10^{19}[\mathrm{m}^{-3}], a \sim 0.28[\mathrm{m}], T \sim 250[\mathrm{eV}], B \sim 0.4[\mathrm{T}], R \sim 0.34[\mathrm{m}]$). Thus, the effect of the electron-electron collision cannot be ignored. On the other hand, the electron-ion collision time(τ_{ei}) is approximately $6 \times 10^3 \tau_A$, so that the thermal relaxation between the electron and the ion fluids does not complete within the time scale of the whole process of this simulation. Therefore, we have to discuss here the electron and the ion transport separately. Furthermore, for highly magnetized plasma like that in this simulation, the temperature will not be isotropic. To estimate the effect of the transport under such condition , the Braginskii's theory[70] is the most reliable one for such collisional plasma.

There are some possible problems we should reconsider when we take account of the effect of heat conduction. Here we discuss them one by one as follows.

- Both the parallel and the perpendicular conduction can affect the linear mode structure of the growth of the instability.

  The main simulation result that is described in Chap.3 shows that the most dominant linear instability mode is the low n interchange mode. The displacement due to the interchange mode occurs only perpendicular to the magnetic field as a nature of the interchange mode. Therefore, the parallel heat conduction will make only a little contribution to the linear growth of the instability. On the other hand, the perpendicular heat conduction can affect the linear instability if the heat conduc-

tion occurs fast enough. The characteristic time scale of the perpendicular heat conduction can be estimated by

$$\tau_{\perp} = nL^2/\kappa_{\perp}, \tag{4.1}$$

where n, L, and $\kappa_{\perp}$ are the number density, the characteristic spatial scale, and the perpendicular thermal conductivity, respectively. The characteristic spatial scale for such perpendicular heat conduction may be the scale of the minor radius a. Using the Braginskii's formulation[70], we can estimate the time scale by

$$\tau_{\perp i} = 3 \times 10^5 \tau_A(\text{for ion}), \tag{4.2}$$
$$\tau_{\perp e} = 6 \times 10^6 \tau_A(\text{for electron}). \tag{4.3}$$

Thus, the time scale of the perpendicular heat conduction is much longer than that of the whole process of this simulation both for the ion and the electron. Therefore, it can be said that the effect of the perpendicular thermal conduction on the linear instability is negligible.

- The localized pressure bulge cannot appear because the displacement can become dull due to the perpendicular heat conduction so that the localized pressure bulge cannot appear.

  The parallel heat conduction can be ignored in this problem for the same reason as the previous problem. In the nonlinear stage, the temperature gradient exists mainly in the localized pressure bulge. Using the same formulation as the previous problem but with the spatial scale of the localized bulge, which may be at least several percent of the minor radius, one can estimate the effect of the heat conduction on the formation of the bulge. The absolute value of the time scale will be still small for this estimation. Thus, the effect of the heat conduction on the weakly nonlinear stage can be neglected.

- The energy transport after the magnetic reconnection occurs can be dominated not by the plasma flow but by the parallel heat conduction.

  In this simulation, a unique mechanism was found. Namely, a large pressure gradient is formed along a reconnected magnetic field line. In general, the parallel heat conductivity is much larger than the perpendicular one in magnetized plasma. The characteristic time scale of the parallel heat conduction for this case is estimated by

$$\tau_{\parallel} = nR^2/\kappa_{\parallel}. \tag{4.4}$$

  Here, we assume the spacial scale of the temperature gradient is characterized by the major radius. Then, we can estimate as,

$$\tau_{\parallel i} = 5 \times 10^{-2} \tau_A (\text{for ion}), \tag{4.5}$$
$$\tau_{\parallel e} = 1 \times 10^{-3} \tau_A (\text{for electron}). \tag{4.6}$$

Thus, it can be said that the parallel heat transport occurs much faster than the characteristic MHD time scale. Therefore, the energy loss by the thermal conduction can actually take place in this process. However, the difference between the convective and the conductive loss of the energy is not an essential matter on the whole relaxation process. The heat energy is rapidly expelled out of the torus from the core region in both loss mechanisms. The succeeding process, such as the formation of the conical structure at the top and the bottom, will not vary from the result described in Chap.3 if the heat transport is taken into account.

- Since the pressure gradient is immediately removed by the parallel heat conduction, the plasma flow cannot be induced.

  The thermal conduction is a process that the imbalance in the temperature is relaxed by collisions of plasma particles. Therefore, the spacial distribution of the temperature will surely flatten by the thermal conduction in a short time scale. However, the imbalance in the pressure can still remain because of the existence of the density gradient. The spatial distribution of the density is determined mainly by the motion of the massive ion, which is characterized by the MHD time scale. Therefore, the plasma flow along the magnetic field will be induced in spite of the rapid parallel heat transport.

It is difficult to examine the above discussion by executing the simulation in practice including such transport effect, partly because the stiffness of the equations with rapid heat transport. A self-consistent analysis with transport effect is the future work.

Chapter 5

Concluding remarks

5.1 Summary

As a first attempt at the generalization of relaxation theory to the finite pressure regime, the physical mechanism of the relaxation phenomenon in ST plasma is investigated by means of numerical simulation. This is the first large scale nonlinear simulation that is applied to ST plasma. The major discoveries of this study are summarized as follows.

- In an instable ST equilibrium with the parameters of $< \beta > \sim 8\%$, $q_0 \sim 1$, pressure driven instability grows dominantly. In particular, for the case $q_0 < 1$, low-n modes which are resonant to the $q = 1$ rational surface such as $m/n = 2/2$ and $1/1$ modes grow with large growth rate.
- In the result of the nonlinear time development of low-n interchange modes, the pressure profile collapses in a short time scale, and the heat energy is rapidly transported from the central region to the edge region of the torus.
- At the weakly nonlinear stage of the growth, the toroidal phases among multiple modes are aligned each other, so that they act additionally to create a toroidally localized pressure bulge on the surface of the torus.
- A magnetic reconnection is induced at the localized bulge between the internal and the external magnetic field. This magnetic reconnection is characterized by following points.
  - The reconnection occurs between almost parallel magnetic fields.
  - There is large difference in the pressure on the field lines to be reconnected, so that a large pressure gradient is formed along a filed line by the reconnection.
  - A strong plasma flow is induced along the magnetic field through the reconnection.
- Part of plasma confined in the torus is lost out of the separatrix by the strong plasma flow, which is induced by the reconnection, so that a pair of characteristic structures which consists of thin conical layers, are formed at the top and the bottom of the torus by the expelled plasma flow. It is a newly discovered type of convective loss.

- The configuration is not perfectly destroyed by the event, and the following time development in the large scale behavior shows the stabilization and the recovery to an axisymmetric torus configuration.
- Another instable mode can be excited with an enhancement of the resistivity. The nonlinear development of this mode shows a $m = 2/n = 1$ deformation and a quite destructive behavior.
- These nonlinear behavior appears both for the $q_0 < 1$ and the $q_0 > 1$ cases.

The simulation results are intensively compared with experimental observations. It shows excellent agreement for several points in both temporal and spatial scale.

In conclusion, the physical mechanism of the IRE in ST plasma has been revealed from the onset of the growth of the instability to the collapse of the pressure profile.

5.2 Future work

As an extension of the present simulation study, the mechanism of the later stage of an IRE, that is, the resiliency accompanying the increase in the total current, still remains to be accounted for. This should be firstly elucidated. Besides, in our simulation, a considerable amount of heat energy is left at the core region even at the posterior state after the expulsion of the heat energy due to the magnetic reconnection. One of the key point of the resiliency is whether the left heat energy is to be restored to a free energy of the system or not. The highly twisted structure which appears just after the collapse implies that the magnetic energy is supersaturated around the torus. If the excessive magnetic energy can be transformed into the heat energy in a desirable way, that is, into a free energy, then the event will recur. It has been revealed by this simulation that there is a tendency to recover the torus when the fine structure disappears immediately by an anomalous enhancement of the dissipation. Therefore, it may be important to treat the exclusion mechanism for small scale structure appropriately. Furthermore, to reveal the mechanisms of resiliency will be related to the destabilization of the system at the beginning, which is assumed beforehand in the present simulation.

Another interest is to be directed to the next generation of ST experiments, such as MAST[24, 45] and NSTX[43, 44], which are starting their operation, and other larger devices in the planning stage[71]. Their equilibrium configurations are designed to have much larger elongation and the central safety factor ($\kappa \sim 10$, $q_0 \sim 4$). The dynamical behavior will be quite different with that in the present STs. It will provide interesting materials when we compare the results.

As for the generalization of relaxation theory, fragmentary knowledge has been derived by this study. For example, the magnetic reconnection is an important element for relaxation in this event. However, it has rather a secondary meaning as a kind of trigger of relaxation. The posterior stage to the reconnection is governed by the global configuration, in particular, the pressure gradient parallel to the magnetic field. The system

tends to quickly follow the global magnetic structure. Such is in contrast to the Taylor type relaxation, in which the magnetic reconnection plays a central role in the whole relaxation process by discriminating the progress of the dissipation between the energy and the helicity. Furthermore, as shown in other work[5], a large scale advection in the system determines the process. Therefore, the generalization of the relaxation theory must be done by introducing some global parameters. Though the completion of the generalization needs much information and is beyond our subject at the present situation, these result from our study will develop the argument further.

Acknowledgment

I would like to express my thanks to Prof. Takaya Hayashi for his guidance in the past three years of my graduate study.
I wish to thank Prof. Tetsuya Sato for providing me with an opportunity to study the physics of high beta plasma at Theory and Computer Simulation Center of National Institute for Fusion Science.
Special thanks are due to Dr. Noriyoshi Nakajima for numbers of valuable comments. The analysis of linear instability which is described in Chap.3.2 owes much to his advice. I am indebted to Dr. Yasushi Todo and Dr. Tomo-Hiko Watanabe for their fruitful discussion and helps on execution of this work. The experimental data was provided by Dr. Alan Sykes and Dr. Michael Gryaznevich of UKAEA, Culham. Thanks are due to them for permission to use the unpublished photographs in my research. I wish to express my gratitude to Dr. Martin Peng and Dr. Masayuki Ono of Princeton Plasma Physics Laboratory and Dr. Yuichi Takase of Univ. of Tokyo for their fruitful comments.
My special thanks are due to all the stuff and students of TCSC for their supports.

Bibliography

[1] J. B. Taylor
"Relaxation of Toroidal Plasma and Generation of Reverse Magnetic Fields"
Phys. Rev. Lett. **33** (19), 1139-1141 (1974)

[2] J. B. Taylor
"Relaxation and Magnetic Reconnection in Plasmas"
Rev. Modern Phys. **58** (3), 741-763 (1986)

[3] S.-P. Zhu, R. Horiuchi, T. Sato, and The Complexity Simulation Group
"Non-Taylor Magnetohydrodynamic Self-Organization"
Phys. Rev. E **51** (6), 6047-6054 (1995)

[4] Y. Ono, A. Morita, and M. Katsurai
"Experimental Investigation of Three-Dimentional Magnetic Reconnection by Use of Two Spheromaks"
Phys. Fluids B**5** (10), 3691-3701 (1993)

[5] T.-H. Watanabe, T. Sato, and T. Hayashi
"Magnetohydrodynamic Simulation on Co- and Counter-Helicity Merging of Spheromaks and Driven Magnetic Reconnection"
Phys. Plasmas **4** (5), 1297-1307 (1997)

[6] Y.-K.M.Peng and D. J. Strickler
"Features of spherical torus plasmas"
Nucl. Fusion **26** (6), 769-777 (1986)

[7] A. Sykes
"Behaviour of low-aspect-ratio tokamak plasmas"
Plasma phys. Contr. Fusion, **34**, 1925-1930 (1992).

[8] M. Yamada
"Charming characteristics of the Ultra Low Aspect Ratio Tokamak, ULART"
J. Plasma and Fusion Res. **72** (3), 205-217 (1996) (in Japanese)

[9] M. Gryaznevich and A. Sykes
private communications (1998-1999)

[10] Y.-K.M.Peng, J. D. Galambos, and P. C. Shipe
"Small tokamaks for fusion technology testing"
Fusion Technology **21** , 1729-1738 (1992)

[11] Y.-K.M.Peng
"Prospects and status of low-aspect-ratio tokamaks"
Trans. Fusion Technology **27** , 138-143 (1995)

[12] F. Troyon, R. Gruber, H. Saurenmann, S. Semenzato, and S. Succi
"MHD-Limits to plasma confinement"
Plasma Phys. Contr. Fusion **26** (1A), 209-215 (1984)

[13] H. Bruhns, R. Brendel, G. Raupp, J. Steiger
"Study of the low aspect ratio limit tokamak in the heidelberg spheromak experiment"
Nucl. FUSION **27** (12), 2178-2182 (1987)

[14] A. Sykes, E. Del Bosco, R. J. Colchin, G. Cunningham, R. Duck, T. Edlington, D. H. J. Goodall, M. P. Gryaznevich, J. Holt, J. Hugill, J. Li, S. J. Manhood, B. J. Parham, D. C. Robinson, T. N. Todd and M. F. Turner
"First results from the START experiment"
Nucl. Fusion, **32**, 694-699 (1992).

[15] M. Gryaznevich, DJH. Goodall, T.C.Hender, J. Hugill, I. Jenkins, R. Martin, M. Price, C. Ribeiro, A. Sykes, M.J. Walsh
"MHD activity and operational limits on START"
22nd EPS Conf., ΘBournemouth (1995 EPS Geneva), II-17.

[16] R. Akers, R. A. Bamford, M. K. Bevir, R. J. Buttery, A. Caloutsis, P. G. Carolan, N. J. Conway, M. Cox, G. F. Counsell, T. Edlington, C. G. Gimblett, M. Gryaznevich, T. C. Hender, I. Jenkins, O. J. Kwon, R. Martin, M. Mirinov, K. Morel, A. W. Morris, M. P. S. Nightingale, M. R. O'Brien, Y. -K. M. Peng, S. Petrov, P. D. Phillips, C. Ribeiro, D. C. Robinson, S. E. Sharapov, A. Sykes, C. C. Tsai, M. Tournianski, M. Valovic, M. J. Walsh, *Fusion Energy 1996*(International Atomic Energy Agency, Vienna, 1997), Vol. 2, 57.

[17] A. Sykes
"High β produced by neutral beam injection in the START (Small Tight Aspect Ratio Tokamak) spherical tokamak"
Phys. Plasmas **4** (5), 1665-1671 (1997).

[18] M. Gryaznevich, R. Akers, P. G. Carolan, N. J. Conway, D. Gates, A. R. Field, T. C. Hender, I. Jenkins, R. Martin, M. P. S. Nightingale, C. Ribeiro, D. C. Robinson, A. Sykes, M. Tournianski, M. Valovic and M. J. Walsh
"Achievement of Record β in the START Spherical Tokamak"
Phys. Rev. Lett., **80**, (18), 3972-3975 (1998).

[19] D. A. Gates, R. Akers, L. Appel, P. G. Carolan, N. Conway, J. Dowling, M. Gryaznevich, T. Hender, O. J. Kwon, R. Martin, M. Nightingale, M. Price, C. Roach,

A. Sykes, M. R. Tounianski, M. Walsh, C. D. Warrick, START and NBI teams
"High-Performance Discharges in the Small Tight Aspect Ratio Tokamak (START)"
Phys. Plasmas, **5**, (5), 1775-1783 (1998).

[20] P. G. Carolan, R. J. Akers, L. Appel, N. J. Conway, G. F. Counsell, A. R. Field, D. A. Gates, S. J. Gee, M. P. Gryaznevich, I. Jenkins, R. Martin, K. Morel, A. W. Morris, M. P. S. Nightingale, C. M. Roach, A. Sykes, A. Tukachinsky, M. R. Tournianski, M. J. Walsh, and the START operations team
"Enhanced performance in the START tokamak"
Plasma Phys. Contr. Fusion **40** , 615-620 (1998)

[21] T. C. Hender, S. J. Allfrey, R. Akers, L. C. Appel, M. K. Bevir, R. J. Buttery, M. Gryaznevich, I. Jemkins, O. J. Kwon, R. Martin, S. Medvedev, M. P. S. Nightingale, C. Ribeiro, C. M. Roach, D. C. Robinson, S. E. Sharapov, A. Sykes, L. Villard, and M. J. Walsh
"Magneto-hydrodynamic limits in spherical tokamaks"
Phys. Plasmas, **6** (5), 1958-1968 (1999)

[22] A. Sykes, R. J. Akers, L. C. Appel, P. G. Carolan, J. W. Connor, N. J. Conway, G. F. Counsell, A. Dnestrovskij, Yu. N. Dnestrovskij, M. Gryaznevich, P. Helander, M. P. S. Nightingale, C. Ribeiro, C. M. Roach, M. Tournianski, M. J. Walsh, H. R. Wilson, The START Team, and The NBI Team
"*H*-Mode Operation in the START Spherical Tokamak"
Phys. Rev. Lett. **84** (3), 495-498 (2000).

[23] K. G. McClements, M. P. Gryaznevich, S. E. Sharapov, R. J. Akers, L. C. Appel, G. F. Counsell, C. M. Roach, and R. Majeski
"Physics of energetic particle-driven instabilities in START spherical tokamak"
Plasma Phys. Contr. Fusion **41**, 661-678 (1999)

[24] A. Sykes
"The spherical tokamak programme at Culham"
Nucl. Fusion **39** (9Y), 1271-1282 (1999).

[25] D. C. Robinson
"The physics of spherical confinement system"
Plasma Phys. Contr. Fusion **41** , A143-A157 (1999)

[26] M. Ono, C. B. Forest, Y. -S. Hwang, R. J. Armstrong, W. Choe, D. S. Darrow, G. J. Greene, T. Jones T. R. Jarboe, A. Martin, B. A. Nelson, D. Orvis, C. Painter, L. Zhou, J. A. Rogers, M. J. Schaffer, A. W. Hyatt, R. I. pinker, G. M. Staebler, R. D. Stambaugh, E. J. Strait, K. L. Greene, J. Leuer, and J. M. Lohr
"Novel current drive experiments on the CDX-U, HIT, and DIII-D tokamaks"
(*Plasma Phys. Contr. Nucl. Fusion Res.* , 1993, IAEA, Vienna) **1**, 693-700.

[27] Y. S. Hwang, M. Yamada, T.G. Jones, M. Ono, W. Choe, S.C. Jardin, E. Lo, G. Ludwig, J. Menard, A. Fredricksen, R. Nazikian, N. Pomphrey, S. Yoshikawa, A. Morita, Y. Ono, T. Itagaki, M. Katsurai, and K. Tokimatsu

"Exploration of low-aspect-ratio tokamak regimes in the CDX-U and TS-3 devices"
(*Plasma Phys. Contr. Nucl. Fusion Res.* , 1994, IAEA, Vienna) **1**, 737-746.

[28] M. Ono, D. Stutman, Y.S. Hwang, W. Choe, J. Menard, T. Jones, E. Lo, R. Armstrong, M. Finkenthal, V. Gusev, S. Jardin, R. Kaita, J. Manickam, T. Munsat, R. Nazikian, and Y. Petrov
"Investigation of the Effect of resistive MHD modes on spherical torus performance in CDX-U"
Fusion Energy 1996 (IAEA,Viena,1997), **2**, 71-82.

[29] T. R. Jarboe, B.A.Nelson, A.K. Martine, D.J. Orvis, L.A. McCullough, J. Xie, C. Zhang, and L. Zhou
"Formation and sustainment of a low aspect ratio tokamak by coaxial helicity injection"
(*Plasma Phys. Contr. Nucl. Fusion Res.* , 1994, IAEA, Vienna) **1**, 725-735.

[30] B. A. Nelson, T. R. Jarboe, D. J. Orvis, L.A. McCullough, J. Xie, C. Zhang, and L. Zhou
"Formation and sustainment of a 150kA tokamak by coaxial helicity injection"
Phys. Rev. Lett. **72** (23), 3666-3669 (1994).

[31] B. A. Nelson, T. R. Jarboe, A.K. Martin, D. J. Orvis, J. Xie, C. Zhang, and L. Zhou
"Formation and sustainment of a low-aspect ratio tokamak by coaxial helicity injection"
Phys. Plasmas **2** (6), 2337-2341 (1995).

[32] B. A. Nelson, T. R. Jarboe, R. Ewig, C. Hoffman, A.K. Martin, K. McCollum, D. J. Orvis, U. Shumlak, and B. Udrea
"Results from the HIT-II coaxial helicity injection spherical tokamak"
IEEE confernce record, 1997 International Confernce on Plasma Science,318.

[33] T. R. Jarboe, M.A. Bohnet, A.T. Mattick, B.A. Nelson, and D.J. Orvis
"Results from current drive experiments on the Helicity Injected Torus"
Phys. Plasmas **5** (5), 1807-1814 (1998).

[34] H. Toyama, S. Ohdachi, K. Hanada, K. Shinohara, T. Oikawa, K. Nozawa, H. Totsuka, E. Ishiyama, N. Shinoda, and K. Yamagishi
"Observation of turbulence suppresison and transport reduction in the presence of sheared flow"
IAEA 1994 **1** , 575-581 (1995)

[35] K. Hanada, T. Oikawa, K. Nozawa, H. Totsuka, K. Shinohara, E. Ishiyama, N. Shinoda, K. Yamagishi, and H. Toyama
"Low aspect ratio tokamak experiment in University of Tokyo"
Trans. Fusion Tech. **27** , 440-443 (1986)

[36] H. Toyama, K. Hanada, K. Yamagishi, T. Oikawa, K. Shinohara, H. Totsuka, E. Ishiyama, H. Saito, S. Shiraiwa, M. Hasegawa, I. Nakajima, and M. Ushigome
"Helicity injection experiments and turbulence measurments on the Tokyo spherical

tokamak"
Fusion Energy 1996(International Atomic Energy Agency, Vienna, 1997), **2** , 223-228 (1997).

[37] H. Toyama, K. Hanada, K. Yamagishi, H. Totsuka, E. Ishiyama, S. Shiraiwa, S. Duroach, I. Nakajima, M. Ushigome, N. Uetake, K. Tanji, A. Ejiri, and Y. Takase
"Comparative Studies of Spherical Tokamak and Conventional Tokamak: Magnetic Turbulence-induced Transport"
17th IAEA Fusion Energy Conference, IAEA-CN-69/EXP2/15, Yokohama(1998).

[38] Y. Ono, M. Inomoto, T. Ozaki, and Y. Ueda
"Experimental Investigation of Three-Component Magnetic reconnection by use of merging spheromaks and tokamaks"
Phys. Plasmas **4** (5), 1953-1963 (1997).

[39] A. Morita, Y. Ono, M. Katsurai, M. Yamada, and S. Yoshikawa
"Experimental Investigation on Tilt Stabilizing Effect of External Toroidal Field i Low Aspect Ratio Tokamak"
Phys. Plasmas **4** (2), 315-322 (1997)

[40] M. Nagata, N. Yuasa, P. Gu, N. Yagi, S. Kano, N. Fukumoto and T. Uyama
"Helicity Injection and Current Drive of Spherical Tokamak and Spheromak Plasmas in HIST"
17th IAEA Fusion Energy Conference, IAEA-CN-69/EXP4/10, Yokohama(1998).

[41] Y. Narushima, T. Asai, S. Shimamura, T. Takahashi, Y. Nogi and Y. Ohkuma
"Low Aspect Ratio Tokamak produced by Negative-Biased Theta-Pinch"
ICPP98 + 25th EPS CCFPP, Prague(1998), ECA Vol. 22C, p. 906-909.

[42] I. R. Jones, C. Deng, I.M. El-Fayoumi, and P. Euripides
"Operation of the Rotamak as a Spherical Tokamak: The Flinders Rotamak-ST"
Phys. Rev. Lett **81** (10), 2072-2075 (1998).

[43] J. H. Chrzanowski, H.M. Fan, P.J. Heitzenroeder, M. Ono, and J. Robinson
"Engineering Overview of the National Spherical Tokamak Experiment"
16th IEEE/NPSS Symposium on Fusion Engineering(1995), **2**,1430-1433.

[44] M. Ono and NSTX team
"Exploration of Spherical Torus Physics in the NSTX Device"
17th IAEA Fusion Energy Conference, IAEA-CN-69/ICP/01-EX4/1, Yokohama(1998).

[45] A. C. Darke, M. Cox, J.R. Harbar, J.H. Hay, J.B. Hicks, J.W. Hill, D. Hurford, J.S. McKenzie, A.W. Morris, M.P.S. Nightingale, T.N. Todd, G.M. Voss, and J.R. Watkins
"The Mega Amp Spherical Tokamak"
16th IEEE/NPSS Symposium on Fusion Engineering(1995), **2**,1456-1459.

[46] R. Fonck, G. Garstka, T. Intrator, B. Lewicki, T. Thorson, R. Toonen, K. L. Tritz, B. White and G. Winz
"Overview of the Pegasus Extremely Low-Aspect Ratio Tokamak"
Bull. Am. Phys. Soc. **41**, 1400 (1996).

[47] V.E. Golant, E.Z. Gusakov, V.K. Gusev, V.B. Minaev, A.N. Novokhatsky, K.A. Podushnikova, N. V. Sakarov, K.G. Shakhovetz, V.S. Uzlov, V.A. Belyakov, A.A. Kavin, Y.A. Kostzov, E.G. Kuzmin, V.F. Soikin, E.A. Azizov, E.A.Kuznetzov, V.A. Yagnov, N.Y. Dvorkin, G.P. Gardymov, V.V. Mikov, A.Y. Dnestrovskii, and S.Y. Medvdev
"Globus-M Experiment at the Final Stage of Preparations"
17th IAEA Fusion Energy Conference, IAEA-CN-69/ICP/02-EX4/1, Yokohama(1998).

[48] B. A. Carreras, L.A. Charlton, J.T. Hogan, J.A. Holmes, and E.A. Lazarus
"MHD Stability in Low-Aspect-Ratio Tokamaks"
Plasma. Phys. Contr. Nucl Fusion Res.(1986) **253**-63

[49] R. Gruber, F. Troyon, D. Berger, L.C. Bernard, S. Rousset, R. Schreiber, W. Kerner, W. Schneider, and K.V. Roberts
"ERATO Stability Code"
Comp. Phys. Communications **21** 323-371 (1981).

[50] R. C. Grimm, R.L. Dewer, and J. Manickam
"Ideal MHD Stability Calculation in Axisymmetric Toroidal Coordinate Systems"
J. Comp. Phys **49** 94-118(1983).

[51] J. E. Menard, S.C. Jardin, S.M. Kaye, C.E. Kessel, and J. Manickam
"Ideal MHD Stability Limits of Low Aspect Ratio Tokamak Plasmas"
Nucl. Fusion **37** 595-610(1997)

[52] M. Yamada, N. Pomphrey, A. Morita, Y. Ono, and M. Katsurai
"Global Stability Study of the Ultralow Aspect Ratio Tokamak, ULART"
Nucl. Fusion**36** 1210-1216 (1996)

[53] R. J. Buttery, M.K. Bevir, A. caloutsis, D. Gates, C. G. Gimblett, M. Gryaznevich, T.C. Hender, I. Jenkins, R. Martin, C. Ribeiro, D.C. Robinson, A. Sykes, M. Valovic, M.J. Walsh, and H.R. Wilson
"Study of Internal Reconnection Events on the START Tokamak"
23rd EPS Conf. on Controlled Fusion and Plasma Phys., Kiev, 1996, EPS, Vol. 20c, Part I, 416-419 (1996)

[54] Ya. I. Kolesnichenko, V.V. Lutsenko, and V.S. Marchenko
"Fishbone Mode in Spherical Tokamaks"
Phys. Rev. Lett. **82** (16) 3260-3263 (1999)

[55] R. Horiuchi and T. Sato
"Full Magnetohydrodynamic Simulation of the Tilting Instability in a Field-Reversed Configuration"
Phys. Fluids B **1** (3) 581-590 (1989)

[56] J.P. Freidberg
"*Ideal Magnetohydrodynamics*"
Plenum Press, New York (1987), pp. 108.

[57] G. Bateman
"*MHD Instabilities*"
The MIT Press, Cambridge, (1978), pp. 89.

[58] J.M. Greene and J.L. Johnson
"Interchange Instabilities in Ideal Hydromagnetic Theory"
Plasma Physics, Pergamon Press, Northern Ireland (1968), Vol.10, pp. 729-745.

[59] J.P. Freidberg
"*Ideal Magnetohydrodynamics*"
Plenum Press, New York (1987), pp. 401.

[60] J.W. Connor, R.J. Hastie, and J.B. Taylor
"High Mode Number Stability of an Axisymmetric Toroidal Plasma"
Proc. R. Soc. Lond. A. **365** 1-17 (1979)

[61] N. Mizuguchi, T. Hayashi, and T. Sato
"Nonlinear simulation of Internal Reconnection Event (IRE) in Spherical Tokamak (in Japanese)"
J. Plasma and Fusion Res.**75**(5) CD-ROM (1999)

[62] N. Mizuguchi, T. Hayashi, and T. Sato
"Dynamics of Spherical Tokamak Plasma on Internal Reconnection Event"
Phys. Plasmas, **7** (3), 940-949 (2000).

[63] T. Hayashi, N. Mizuguchi, T.-H. Watanabe, Y. Todo, T. Sato, and The Complexity Simulation Group
"Nonlinear simulation of Internal Reconnection Event in Spherical Tokamak"
Nuclear Fusion , **40** (3), 721-726 (2000).

[64] T. Hayashi, N. Mizuguchi, T. Sato, and The Complexity Simulation Group
"Numerical simulation of Internal Reconnection Event in Spherical Tokamak"
J. Plasma and Fusion Res. SERIES **2** 43-47 (1999).

[65] K. Nishihara and T. Ikegawa
"Weakly Nonlinear Theory of Rayleigh-Taylor Instability"
J. Plasma Fusion Res. SERIES **2** 536-540 (1999)

[66] T. Sato and T. Hayashi
"Externally Driven Magnetic Reconnection and Powerful Magnetic Energy Converter"
Phys. Fluids **22** (6) 1189-1202 (1979)

[67] N. Mizuguchi, T. Hayashi, and T. Sato
"Convective Loss of Heat Energy Excited in the Edge Region of Spherical Tokamak"
Contrib. Plasma Phys., in printing.

[68] C.K. Birdsall and A.B. Langdon
"*Plasma Physics via Computer Simulation*"
Bristol , New York (1991), pp. 437.

[69] T. Hayashi, N. Mizuguchi, T. Sato, and The Complexity Simulation Group
"Nonlinear Simulations of Relaxation Phenomena in Spherical Tokamak"
Chinese Phys. Lett., in printing.

[70] S.I. Braginskii
"*Review of Plasma Physics*"
Consultant Bureau , New York (1965), Vol. 1, pp. 205.

[71] M. Peng and Contributers
"Science and Technology of the 10-MA Spherical Tori"
17th IAEA Fusion Energy Conference, IAEA-CN-69/FTP/04(R)-FT1/2(R), Yokohama(1998).

Appendix A

Numerical convergence test on the simulation

As we can see in the simulation results described in Chap.3, the whole process is governed by activities which have the large spacial scale. In particular, the $n = 1$ and the $n = 2$ modes play important roles. Therefore, it is necessary to check the convergence properties to the numerical mesh and the time step, or to the boundary condition at least for low-n modes.

Mesh and time step convergence can be examined by comparing results computed with various mesh numbers and time steps. We have executed such runs with the same parameter as stated in the body of the text for five different cases listed in Table.A.1, where the mesh number and the time step are halved compared to the original case.

The growth rates of the linear eigenmode that are obtained by executing the nonlinear simulation for these case are shown in Fig.A.1. We can see from Fig.A.1 that there is no significant change among these cases for low-n modes.

In addition, the nonlinear time development is checked for case A. The result of the temporal change in the three-dimensional pressure profile is shown in Fig.A.2. It is shown that quite similar behavior to that for the original case, such as the formation of the localized bulge, reconnection, and the conical shape, as well as the time scale of the development of the process.

Table A.1: Parameters for the convergence test runs.

case	number of mesh $N_r \times N_\theta \times N_z$	α^1
O	$128 \times 64 \times 128$	1 (main result)
A	$128 \times 32 \times 128$	1
B	$64 \times 64 \times 128$	1
C	$128 \times 64 \times 64$	1
D	$128 \times 64 \times 128$	0.5

[1] α : ratio of characteristic speed of mesh $(\delta x/\delta t)$ to the Alfvèn speed

In conclusion, the mesh size and the time step used in the simulation are appropriate for the present problem.

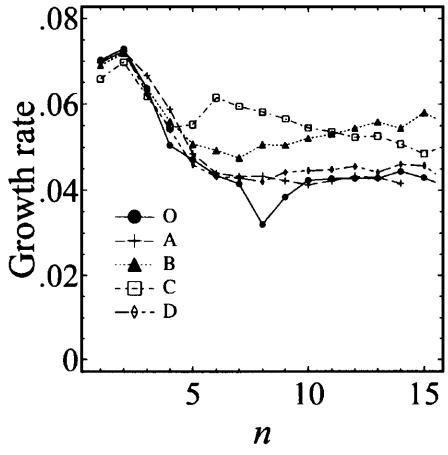

Figure A.1: Comparison in the linear growth rate among cases with different grid numbers and time steps.

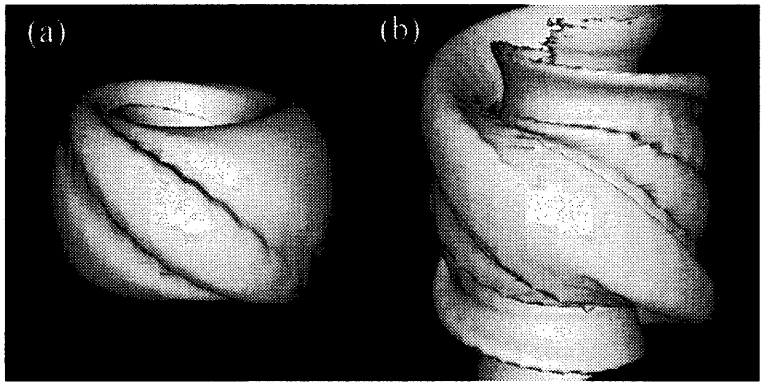

Figure A.2: Simulation results in the nonlinear stage for case A. Similar structures to Fig.3.17 appears in this calculation.

Since the magnetic field line penetrates the top and the bottom boundary, the plasma extends to there at large fluid velocity on the nonlinear stage as described in Chap.3. Therefore, the dependence on boundary conditions for the top and the bottom boundary should be carefully examined.

Figure A.3 shows the time development of the poloidal pressure profile in the simulation result which is executed in a geometry with a dimension doubled in z direction. As we can see from Fig.A.3, the plasma extends almost within $z \pm 1.8$, so that we can conclude the system dimension is sufficient in the original simulation run.

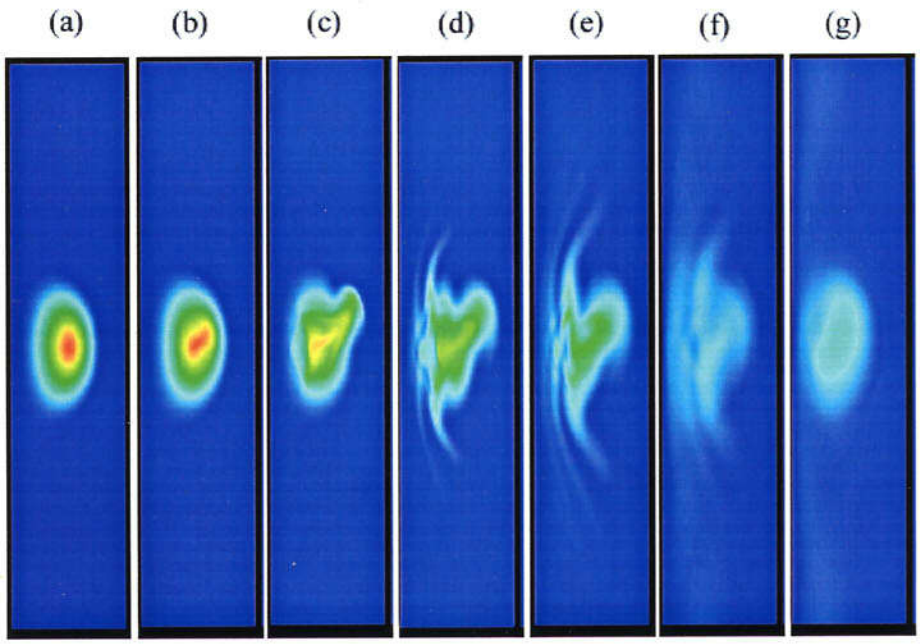

Figure A.3: Simulation results corresponding to Figs.3.10, 3.18, and 3.23 executed in a vertically longer geometry.